4D FLOW MRI POST-PROCESSING STRATEGIES for NEUROPATHOLOGIES

by

Eric Mathew Schrauben

A dissertation submitted in partial fulfillment

of the requirements for the degree of

Doctor of Philosophy

(Medical Physics)

at the

UNIVERSITY OF WISCONSIN – MADISON

2015

Date of final oral examination: 04/16/2015

The dissertation is approved by the following members of the Final Oral Committee:
      Oliver Wieben, Associate Professor, Medical Physics and Radiology
      Andrew Alexander, Professor, Medical Physics and Psychiatry
      Sean Fain, Professor, Medical Physics
      Aaron Field, Professor, Radiology
      Patrick Turski, Professor, Radiology

4D FLOW MRI POST-PROCESSING STRATEGIES for NEUROPATHOLOGIES

Eric M. Schrauben

Under the supervision of Associate Professor Oliver Wieben

At the University of Wisconsin – Madison

Abstract

4D flow MRI allows for the measurement of a dynamic 3D velocity vector field. Blood flow velocities in large vascular territories can be qualitatively visualized with the added benefit of quantitative probing. Within cranial pathologies theorized to have vascular-based contributions or effects, 4D flow MRI provides a unique platform for comprehensive assessment of hemodynamic parameters. Targeted blood flow derived measurements, such as flow rate, pulsatility, retrograde flow, or wall shear stress may provide insight into the onset or characterization of more complex neuropathologies. Therefore, the thorough assessment of each parameter within the context of a given disease has important medical implications.

Not surprisingly, the last decade has seen rapid growth in the use of 4D flow MRI. Data acquisition sequences are available to researchers on all major scanner platforms. However, the use has been limited mostly to small research trials. One major reason that has hindered the more widespread use and application in larger clinical trials is the complexity of the post-processing tasks and the lack of adequate tools for these tasks. Post-processing of 4D flow MRI must be semi-automated, fast, user-independent, robust, and reliably consistent for use in a clinical setting, within large patient studies, or across a multicenter trial. Development of proper post-processing methods coupled with systematic investigation in normal and patient populations pushes 4D flow MRI closer to clinical realization while elucidating potential underlying neuropathological origins.

Within this framework, the work in this thesis assesses venous flow reproducibility and internal consistency in a healthy population. A preliminary analysis of venous flow parameters in healthy controls and multiple sclerosis patients is performed in a large study employing 4D flow MRI. These studies are performed in the context of the chronic cerebrospinal venous insufficiency hypothesis. Additionally, a double-gated flow acquisition and reconstruction scheme demonstrates respiratory-induced changes in internal jugular vein flow. Finally, a semi-automated intracranial vessel segmentation and flow parameter measurement software tool for fast and consistent 4D flow post-processing analysis is developed, validated, and exhibited an in-vivo.

Acknowledgements

When I first met my advisor, Dr. Oliver Wieben, a mere six weeks before I was set to move to Madison and begin my graduate work in the Medical Physics program, it's safe to say I had no idea what I was getting myself into. Those who know Oliver would describe him as enthusiastic: about his research, his job, his family, and all things German. Though I came away knowing very few specifics about what my research would entail, Oliver's vitality (and ability to communicate his energy) in that meeting made my decision very easy. I will always consider myself lucky to have landed in the lab of such an exuberant and passionate advisor.

Through my nearly five years in the program I've worked closely with a number of talented and brilliant researchers within the MRI flow group, without whom most of this research would not have been performed. Dr. Kevin Johnson, not many would argue, possesses a wealth of knowledge concerning MRIs and programming that is unmatched in our group, and his aid in providing quick and helpful answers drove much of my work. Dr. Alejandro Roldan-Alzate was always a source of clever research ideas, and of generally thinking I know more than I actually do (imbuing me with some much needed confidence). Dr. Liz Nett taught me the values of persistence and meticulousness in performing research. Dr. Andrew Wentland educated me on the design and execution of a perfectly run experiment, about which I still have some things to learn. Dr. Ashley Anderson and I spent many hours poring over the intricacies of properly acquiring and measuring phase-contrast images, and we also sent many volunteers into the scanner for a free sauna. Michael Loecher provided some extraordinary acumen in the form of computer programming skills and the ability to perform some spectacular image post-processing in neurovasculature. Others in the flow group, such as Phil Kilgas, Leonardo Rivera, Jacob

surrounded myself with, all of which have made my life in Madison truly enjoyable and memorable.

Table of Contents

List of Figures

List of Tables

Chapter 1:   Introduction

Neurovascular diseases represent a wide range of neurological, functional, and anatomical disorders potentially related to morphologic or hemodynamic vascular changes. Proper monitoring using vascular imaging is vital to assess both acute and chronic alterations within the vasculature. Most clinical imaging of neurovascular disease is done in terms of vessel anatomy, though added information on macroscopic and microscopic blood flow can be important. Flow imaging can be performed with imaging modalities such as Doppler ultrasound (US), positron emission tomography (PET), and digital subtraction angiography (DSA). However, these modalities have some pitfalls: Doppler US is difficult to perform in the brain and is operator-dependent, PET imaging is only useful for microscopic perfusion measurements, and DSA is not truly quantitative.

Magnetic resonance imaging (MRI), which exploits the unique property of spin inherent to protons, can also be used to examine neurovascular disease. Many imaging contrast methods from MRI are tailored to specific pathologies or anatomies of interest, and the robustness and safety of MRI proves very useful in clinical and research settings, especially when performing longitudinal studies.

The measurements of blood velocities are particularly interesting with respect to the neurovasculature. Phase contrast MR (PC MR) is the most commonly used MRI technique for the assessment of velocities and also allows for the generation of angiographic information. With 4D flow MRI, time and three-directional velocity data is acquired over a volume, providing flow information over an entire region; in the cranial context whole brain vasculature is measured. In recent years, there has been extensive work in the field of 4D flow MRI to improve both data

acquisition and reconstruction. With the movement to larger patient populations and multicenter studies, a major limiting step becomes accuracy and duration of post-processing techniques used to analysis 4D flow MRI data.

The aim of this thesis work was to develop novel 4D flow acquisition, reconstruction, and data processing schemes to ameliorate issues related to 4D flow MRI. Specifically, the reliability of 4D flow in cerebrospinal veins was examined, venous drainage in patients with multiple sclerosis was investigated and compared to healthy controls, a double-gated cardiac and respiratory acquisition and reconstruction scheme was developed and tested in healthy subjects, and a novel semi-automated intracranial 4D flow processing scheme was developed and validated.

The organization of this thesis is as follows:

Chapter 2: Background provides brief overviews of a number of topics relevant to this thesis. The assessment of neurovascular diseases with MRI is presented, focusing on research concerning potential PC MR biomarkers of disease. MR physical principles are introduced, including signal formation, acquisition, and reconstruction. PC MR physics, considerations, errors, and correction methods are presented. Finally 4D flow MRI, including acceleration techniques and practical considerations, is described.

Chapter 3: Reproducibility of Cerebrospinal Venous Blood Flow and Luminography using PC VIPR and CE MRA presents a test-retest investigation into the reproducibility and reliability of measuring and visualizing venous blood flow. 4D flow MRI of major head, neck, and chest veins is performed and flow is quantified in ten healthy subjects. MRA of the internal jugular veins is scored by two experienced radiologists and compared from day-to-day. The

material in this chapter was presented at ISMRM 2012 (1), ISMRM 2013 (2) and is published in the American Journal of Neuroradiology (3).

Chapter 4: Preliminary Results – Multiparameter CCSVI Study presents data from a larger CCSVI study that is currently underway at our institution. Patients with multiple sclerosis and age- and sex-matched healthy controls underwent a battery of MRI scans to look at quantitative biomarkers in normal appearing white matter and venous blood flow. After processing of data, subject statuses were unblinded and compared across all parameters of interest. This work has been accepted for presentation at ISMRM 2015 (4,5).

Chapter 5: Respiratory-Induced Venous Blood Flow Effects Using Flexible Retrospective Double-gating introduces a novel simultaneously cardiac and respiratory double-gated PC MR acquisition and reconstruction technique, allowing for assessment of changes in flow caused by respiration. The theory of this technique and results from measurements in the internal jugular vein of a healthy volunteer group are presented. The material in this chapter was presented at the ISMRM/SCMR workshop 2012 (6), ISMRM 2012 (7), and is published in the Journal of Magnetic Resonance Imaging (8).

Chapter 6: Fast 4D flow MRI intracranial segmentation and quantification in tortuous arteries focuses on a 4D flow MRI processing scheme that removes user-variability and decreases processing time for large datasets. This chapter presents the development, phantom and in-vivo validation, and in-vivo testing of this processing technique. The material in this chapter was presented at ISMRM 2014 (9) and has been accepted for publication in the Journal of Magnetic Resonance Imaging (10).

Chapter 7: Summary and Recommendations recaps the material covered in this dissertation with respect to medical imaging. Future studies and developments are proposed to enhance the research herein presented.

Chapter 2:   Background

2.1 Neurovascular Diseases and Neuropathologies

2.1.1   Introduction

The brain is provided oxygen and nutrients via the cerebrovascular system, such that any abnormalities in the macro- or microvasculature may affect the brain's functionality and lead to neurovascular disease. Its pathologies are comprised of a group of disorders with a wide range of phenotypes and high heterogeneity. Therefore research performed in this area is equally as variable, including investigations into genetic links and pathophysiological mechanisms. A number of investigative techniques are applied, including cell cultures, stem cells, animal models, medical therapies, and surgical or endovascular therapies. At the crux of much of this research is the role of vascular imaging, which provides in-vivo assessment and monitoring with subjects who have or are at risk of having a neurovascular disease.

Structurally, abnormal neurovasculature may exhibit increased vessel wall thickness, permeability, increased tortuosity, changes in size and shape (formations of stenoses or aneurysms), and perforations leading to hemorrhage. Functionally, abnormal blood flow has been commonly observed in brain disorders, manifesting as alterations in oxygen consumption, blood pressure, cerebral blood flow and cerebral blood volume related to changes in microvascular perfusion (11).

2.1.2   Assessment with MRI

Magnetic resonance imaging (MRI) provides a powerful, comprehensive, and noninvasive approach to monitor changes in both structure and function of the neurovascular system. Additionally, MRI has excellent soft tissue contrast capabilities, allowing structural alterations such as vessel size, tortuosity, density, vessel stenoses, and permeability to be

identified by directly visualizing the neurovasculature. Angiographic techniques, such as time-of-flight imaging and contrast-enhanced MR angiography, depict morphologic features of large vessels (12,13). High-resolution MRI T_1 and T_2 weighting allows for assessment of the vessel wall and corresponding plaques or lesions (14). The introduction of a blood pool contrast agent can also provide information on dynamic filling of vessels, as well as permeability, through dynamic contrast-enhanced MRI (15).

Functional neurovascular information in the form of cerebral blood flow and volume, oxygenation, and the oxygen consumption is also garnered through the use of specialized MRI scans. In large vessels, blood flow can be calculated through the use of phase-contrast (PC) MR (16). In the downstream microvasculature, arterial spin labeling and dynamic susceptibility contrast provide information on cerebral blood flow and volume, while blood oxygen level dependent MRI provides information on oxygenation and consumption (17). Thus, MRI allows for a versatile and broad classification of both the structural and functional properties of the neurovascular system. Table 2-1 summarizes a number of example structural and functional parameters and their corresponding MRI acquisitions for use in neurovasculature.

Structural parameter	MRI technique(s)	Functional parameter	MRI technique(s)
Morphology	Time-of-flight Contrast-enhanced MR Angiography	Blood Flow	Phase-contrast MRI
Vessel wall	High-resolution T1/T2 MRI	Cerebral Blood Flow	Arterial Spin Labelling Dynamic Susceptibility Contrast MRI
Vessel Filling	Dynamic contrast-enhanced MRI	Cerebral blood volume	Dynamic Susceptibility Contrast MRI Dynamic contrast-enhanced MRI
		Oxygen consumption	Blood oxygen level dependent MRI

Table 2-1. Summary of example MRI techniques related to structural and functional monitoring of the neurovasculature.

2.1.3 PC MR blood flow biomarkers

As will be detailed below, the use of PC MR allows for the assessment of blood flow in larger vessels. In the brain, these usually include the arteries in the head and neck that feed and are part of the Circle of Willis. These are composed of the bilateral internal carotid, vertebral, middle cerebral, anterior cerebral, posterior cerebral, and the basilar arteries. The draining veins include the superior sagittal, straight sagittal, and bilateral transverse sinuses that connect downstream to the bilateral internal jugular veins (Figure 2-1). PC MR is particularly useful intracranially as other flow imaging modalities, such as Doppler ultrasound, have difficulty identifying intracranial vessels through the skull and have been shown to be user-dependent and highly variable (18).
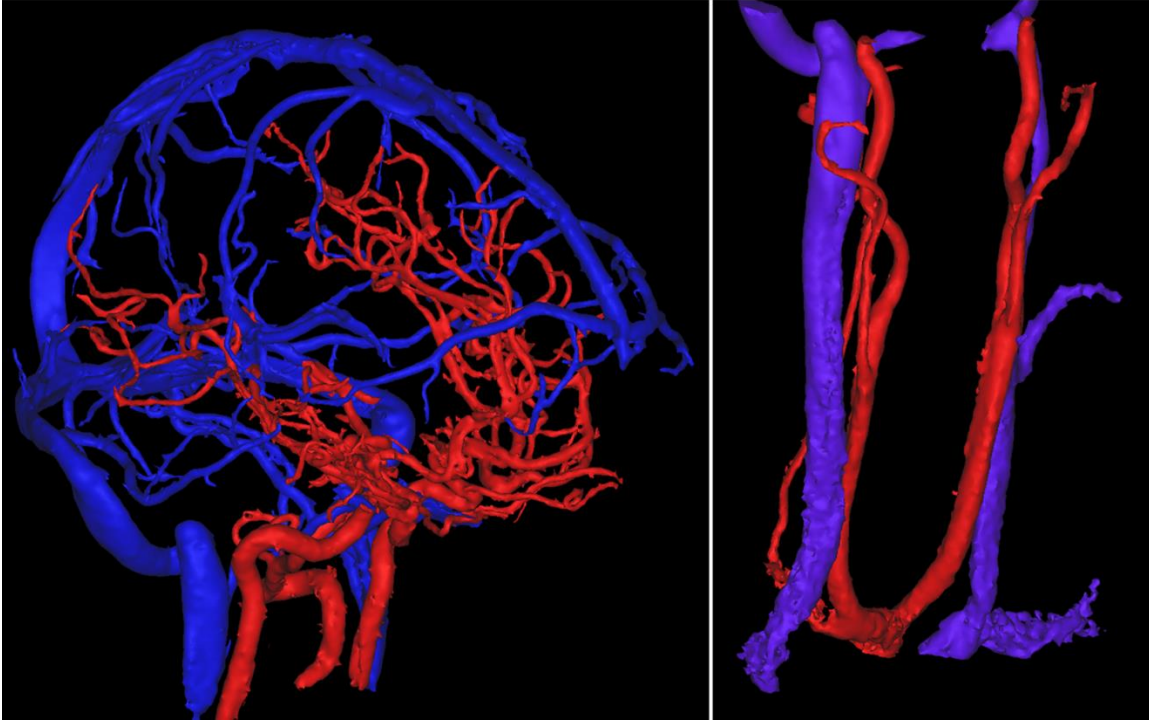
Figure 2-1. Segmented angiographic images display vessels of interest in the head and neck related to many neurovascular diseases. Left: intracranial arteries (red) and veins (blue) form a complex and tortuous network. Right: main feeders and drainers of the brain are the carotid arteries (red) and jugular veins (blue). These images were acquired using PC VIPR, see Section 2.4.2.

PC MR has garnered interest in relation to various neuropathologies as a technique to measure and monitor potential blood flow biomarkers in macrovasculature related to downstream changes in the microvasculature. A few examples of PC MR research into some of these neuropathologies are listed below (Figure 2-2).

Arteriovenous malformations (AVM) of the brain are characterized by tangled arteries and veins which are directly connected, thus bypassing and disrupting the vital capillary cyclic processes. Flow measurements from PC MR in and around AVMs allow for understanding of feeding and draining of the nidus, which may provide predictive information concerning pathologic changes such as flow-induced aneurysms, fistulas, and varices (19). Additionally, PC

MR can be used to gain information on serial filling and draining of AVMs, adding qualitative diagnostic information similar to the digital subtraction angiography without the use of ionizing radiation (20,21). Such information may allow for better risk stratification, more precise monitoring during staged embolization, and improved treatment planning in patients with AVMs.

In intracranial aneurysms, proper and frequent monitoring of aneurysm size and morphology allows for clinical determination of whether intervention is appropriate and the proper timing of the intervention. Additional information can be gained from PC MR to determine the amount of blood flow that is entering and exiting the aneurysm through time (over the cardiac cycle), the stress at aneurysm wall caused by vortical flow formation, and flow visualization to determine impingement zones and potential locations of aneurysmal rupture (22).

PC MR has been used as a tool to investigate a number of other clinical neurovascular conditions that have been reported in literature, including: the characterization of reversed vertebral flow in patients with subclavian steal syndrome (23), the risk stratification of recurrent strokes in patients with vertebrobasilar disease (24), and the efficacy of vascular bypass grafts for cerebral revascularization (25).

Wall shear stress (WSS) describes the drag force on the endothelial surface of vessels induced by the movement of blood. Historically, high WSS correlates with outward vascular remodeling, particularly in aneurysm impingement zones, while low WSS has been used as a biomarker for atherosclerotic development (26). Additionally, computational fluid dynamic simulations have shown WSS to be more perturbed in internal carotid artery siphons, with higher outer-wall WSS and lower inner-wall WSS (27). Neurologically, altered WSS has also been previously associated with lacunar infarction and elevated rupture risk (28,29).

Flow changes may also provide biomarkers for dementia. In the context of Alzheimer's Disease (AD), PC MR has been used to demonstrate a statistically significant increase in pulsatility index (PI) and decrease in mean flow in a number of intracranial arteries when comparing patients with AD and normal controls (30,31). PI has also been shown to increase with age in normal adults, suggesting more rigid and less compliant arteries with age. Decreases in PI in more distal intracranial arterial segments suggest that as one ages and vessels stiffen, larger PI may create more tissue damaging effects in smaller arterial branches (32). These studies highlight a growing area of research connecting diffuse congestive microvascular pathology in AD with global hemodynamic changes.

Clearly cranial flow biomarkers have much promise in the assessment, diagnosis, risk stratification and potential treatment in a number of neurovascular disorders. PC MR, with the ability to provide repeatable, accurate, and noninvasive assessment of intracranial flow, is well-suited for such studies.
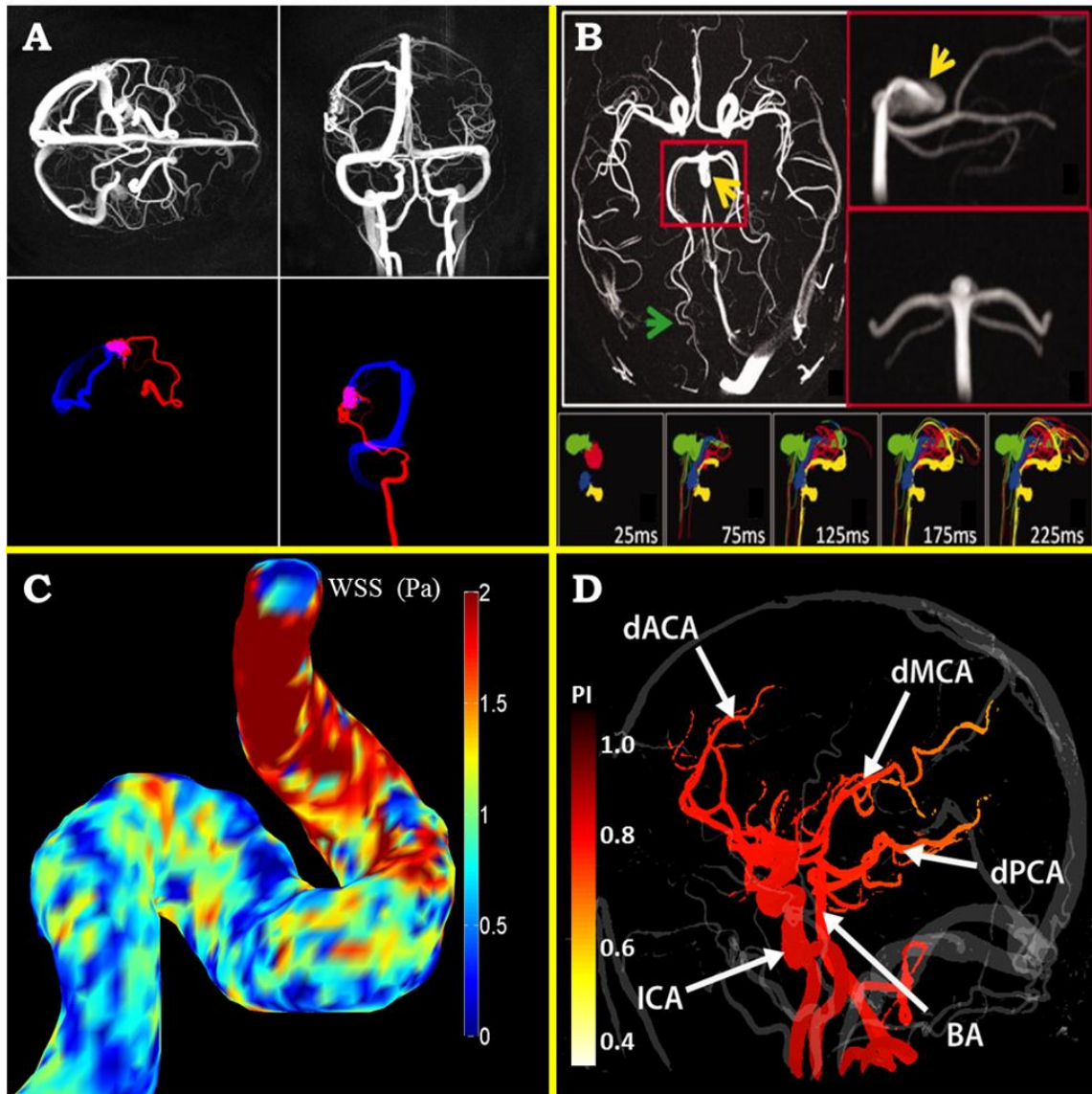
Figure 2-2. Examples of advanced research using PC MR in neurovascular conditions. A: Axial and coronal maximum intensity projections in an AVM. Flow tracking allows for the visualization of the feeding artery (red) and the draining vein (blue) of the AVM nidus (purple) (21). B: Maximum intensity projections depict a basilar tip aneurysm (yellow arrow) as well as branching distal vessels (green arrow). Pathlines at different time points help visualization of the blood distribution in the aneurysm (22). C: Wall shear stress calculations show increases near the superior portion of the siphon of the internal carotid artery (ICA). D: Pulsatility index map in a healthy young adult shows decreases in more distal portions of the anterior, middle, and posterior cerebral arteries (dACA, dMCA, dPCA) compared with the ICA and basilar artery (BA) (32).

2.2 Magnetic Resonance Principles

This section introduces the basic concept of signal formation and detection in nuclear magnetic resonance as it relates to MRI. It is meant solely as a relevant basis for the research that follows and is by no means exhaustive. Extensive and in-depth descriptions exist in published literature (33-36).

2.2.1 Nuclear Magnetic Resonance

All atoms have an intrinsic quantum number, spin, which is dependent on the number of electrons surrounding the protons and neutrons in a nucleus. An odd number of protons, neutrons, or both produces a nuclear charge, and the coupling of charge and spin in these nuclei creates a magnetic dipole moment. Hydrogen molecules (protons) are a key component in biological tissue, such as water, fat, and muscle, and are thus the target of acquisition in most clinical MRI scans. For convenience, here we will use the classical model and not the quantum mechanical model to explain the source of the MR signal.

When tissue containing hydrogen-rich molecules is placed in an external magnetic field B_0, individual magnetic dipole moments act as bar magnets, aligning either with or against the field. Over a large ensemble of these protons, a fraction more will align rather than anti-align, and a net equilibrium magnetization will form. The strength of the net magnetization is governed by the Boltzmann distribution, depending on B_0, the number of spins in the sample, and temperature. Each proton in the sample intrinsically spins around B_0 with resonance frequency ω_0 according to the Larmor equation:

$$\omega_0 = \gamma B_0 \qquad\qquad 2\text{-}1$$

where γ is known as the gyromagnetic ratio, independent for each atomic nucleus. For instance, for protons $\gamma = 42.6\ MHz/T$. As Equation 2-1 shows, precession frequency linearly increases

with the strength of B_0. The net magnetization will possess the same resonance frequency as an individual spin.

2.2.2 Excitation and Relaxation/Decay

The addition of a second magnetic field B_1, in the form of electromagnetic waves at precisely the right frequency and orthogonal to B_0, will disturb the precession of the net magnetization, tipping it into the x-y (or transverse) plane. The strength and duration of this additional field, produced from a radiofrequency (RF) pulse, will determine the amount of excitation of the net magnetization away from its equilibrium state.

Here it is illustrative to introduce the concept of the rotating frame of reference (Figure 2-3). Consider net magnetization vector M_0, rotating around B_0 at resonance frequency ω_0. In the standard laboratory reference frame, RF excitation will decrease the amount of available M_0 along the direction of B_0. This can be viewed as a spiral descending from M_0 into the transverse plane at ω_0. The spiral continues downward as long as the RF pulse is being applied. As the ensemble M_0 all possess the same resonance frequency, switching to a frame of reference spinning at precisely ω_0 simplifies excitation into a vector tipping into the transverse plane. This rotating frame excited state of M_0 can be broken down into orthogonal and independent components, M_Z and M_{XY}. M_Z describes the longitudinal component of the magnetization along the direction of B_0, while M_{XY} is the component in the x-y plane, or the transverse magnetization.
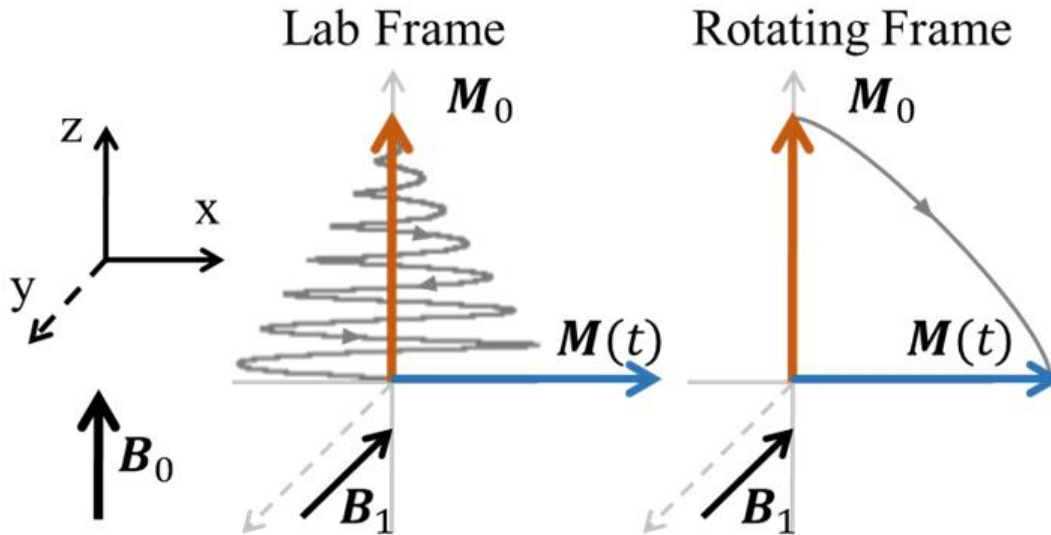
Figure 2-3. Pictorial representation a 90° radiofrequency pulse (from $\boldsymbol{B_1}$) to tip the magnetization $\boldsymbol{M_0}$ (orange arrow) into the x-y plane (blue arrow). In the lab frame, an observer see a spiral motion (gray), rotating at $\boldsymbol{\omega_0}$, down into the transverse plane. In the rotating frame, the observer sees a simple arc motion.

Once tipped into the x-y plane, the net magnetization immediately begins to transition back to its equilibrium state along the z-axis. This is known as T_1, spin-lattice, or longitudinal relaxation. This $\boldsymbol{M_Z}$ regrowth follows an exponential recovery curve and is described by the following equation (assuming $\boldsymbol{M_Z}(0) = 0$; i.e. $\boldsymbol{M_0}$ started in the x-y plane):

$$\boldsymbol{M_Z}(t) = \boldsymbol{M_0}(1 - e^{-t/T_1}) \qquad\qquad 2\text{-}2$$

Differences in tissue water content and physical state cause different T_1 times. It is these differences that provide image contrast and are utilized in many MRI acquisitions. Tissues with short T_1, such as fat, recover more quickly to the equilibrium state than those with long T_1, such as blood. Example recovery curves are shown in Figure 2-4 for experimental values at a magnetic field strength of 3T (37).

While T_1 relaxation describes the regrowth of $\boldsymbol{M_Z}$, T_2 relaxation, also known as spin-spin or transverse relaxation, describes the return of $\boldsymbol{M_{XY}}$ to its equilibrium state (i.e. $\boldsymbol{M_{XY}} = 0$). For

this reason, T_2 relaxation is also often called T_2 decay. Recall that the net magnetization $\boldsymbol{M_0}$ is actually a sum of the magnetization due to many protons. $\boldsymbol{M_0}$ will maintain its magnitude if and only all protons precess at exactly the same frequency. This happens in the instant after excitation via the application of an RF pulse orthogonal to $\boldsymbol{B_0}$. Following the tip of $\boldsymbol{M_0}$ into the x-y plane, some spins will precess at higher frequencies (faster) and some at lower frequencies (slower), so that over time the net magnetization will fan out. This process is known as dephasing and is caused by interactions of local magnetic fields of neighboring spins. T_2 decay is described by the following equation:

$$\boldsymbol{M}_{XY}(t) = \boldsymbol{M}_0 e^{-t/T_2} \qquad\qquad 2\text{-}3$$

Shorter T_2 times describe faster decay (a more quickly dephasing of $\boldsymbol{M_0}$). Similar to T_1 relaxation, different tissues exhibit different T_2 values depending upon tissue makeup. T_2 can be thought of as a basic representation about how fluidic a tissue is; pure liquid water has a very long T_2, while solid or fibrous tissues have very short T_2 times.
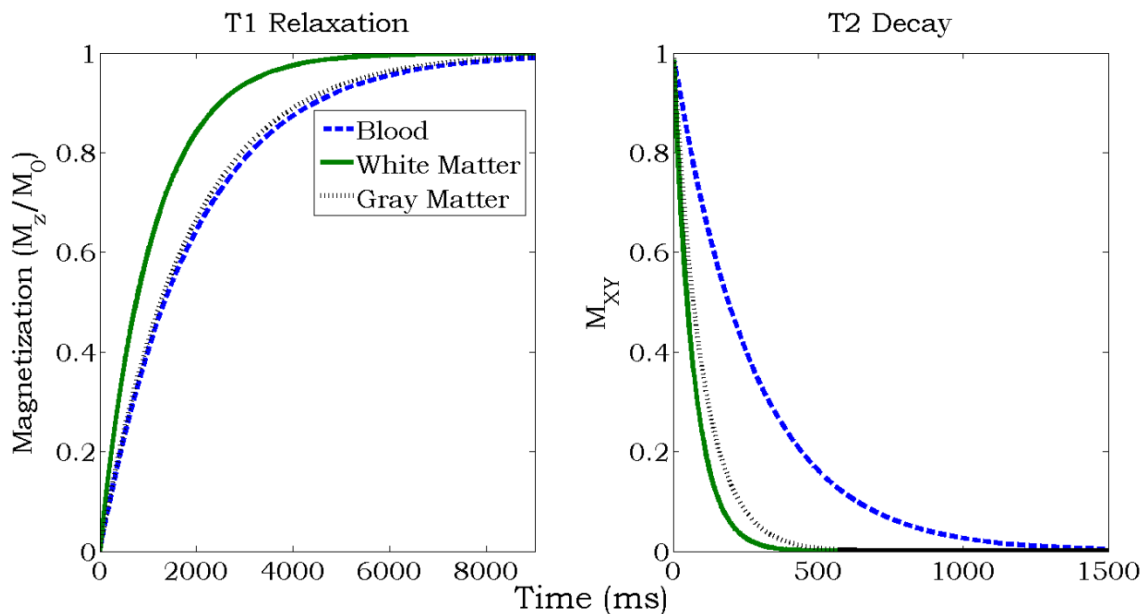
Figure 2-4. Example T_1 and T_2 time curves at a field strength of 3T in different tissues. Note that in all biological tissues, $T_1 > T_2$.

Equations 2-2 and 2-3 show that T_1 and T_2 are not mathematically related, and contrast in MRI often aims to weight images based on T_1, T_2, or both, depending on the desired structure to be highlighted.

The time quantity T_2 does not fully capture dephasing in the transverse plane. Within an imaging voxel, small differences or inhomogeneities in the main magnetic field lead to a more rapid dephasing of $\boldsymbol{M}_{XY}$. This parameter is termed T_2^*, and depends on changes in the local (within a voxel) magnetic field induced by magnetic susceptibility (such as tissue-air interfaces) or the presence of iron. For a given voxel, T_2^* is shorter than T_2, and often produces unwanted image artifacts. Specialized imaging techniques may be employed to eliminate T_2^* artifacts for purely T_2 relaxation.

2.2.3 Signal detection

RF receive coils placed orthogonal to the main magnetic field detect the time-varying signal, in the form of induced current in the coils. The manner in which signal is acquired employs quadrature detection of a circularly polarized magnetic field, resulting in two data streams separated by a phase difference of $\pi/2$. In the spatial frequency domain, known as k-space, the digitized values of these streams are represented via complex notation (i.e. real and imaginary parts modulated by a sine and cosine, respectively). Magnitude and phase of this complex signal are then extracted via demodulation of the signal from the Larmor frequency.

In the MRI context, once all data for an image or volume has been collected, it is reconstructed based on a mathematical operation known as the Fourier transform, effectively transforming data from k-space to image (pixel or voxel) space via a 2D or 3D Fourier transform. This process reconstructs two types of images, also called magnitude and phase.

Magnitude images are the magnitude of real and imaginary parts, are used to maximize the signal-to-noise ratio in an image, and are the typical clinical representation used in MRI. Phase images represent the phase that is accumulated in a given pixel over the course of the acquisition. For many anatomical acquisitions, this signal is compensated for or ignored, but, as shown below, the accrued phase can be used to encode blood flow velocity for hemodynamic information.

2.3 Phase-contrast MRI

2.3.1 Theory

Phase-contrast MRI (PC MR) is an MRI angiographic acquisition scheme that targets moving tissues, most notably blood. The technique was originally described and studied by *Moran et al.* (16). A spin in a magnetic field, with initial position $\boldsymbol{x}_0$, velocity $\boldsymbol{v}$, and acceleration $\boldsymbol{a}$, will accrue phase $\boldsymbol{\varphi}$ as a function of time t according to the following formula:

$$\boldsymbol{\varphi}(t) = \int_0^t i\gamma G(t)(\boldsymbol{x}_0 + \boldsymbol{v}\,t + \frac{1}{2}\boldsymbol{a}t^2)dt \qquad \text{2-4}$$

Where γ is again the gyromagnetic ratio and $G(t)$ is the time-varying magnetic gradient applied in the direction of motion. The expanded form of Equation 2-4 is separable as three distinct forms:

$$\boldsymbol{\varphi}(t) = \boldsymbol{x}_0 \int_0^t i\gamma G(t)dt + \boldsymbol{v} \int_0^t i\gamma G(t)t\,dt + \frac{1}{2}\boldsymbol{a} \int_0^t i\gamma G(t)t^2 dt \qquad \text{2-5}$$

Each integral in Equation 2-5 can be expressed as a moment $\boldsymbol{M}$ of the gradient pulse, finally producing the expression:

$$\boldsymbol{\varphi}(t) = \gamma(\boldsymbol{M}_0 + \boldsymbol{v}\,\boldsymbol{M}_1 + \frac{1}{2}\boldsymbol{a}\boldsymbol{M}_2) \qquad \text{2-6}$$

It is important to note that these moments $M_{0,1,2}$ are distinct from the net magnetization presented in the previous section. The first term in Equation 2-6 represents spatial encoding, the second velocity encoding, and the third acceleration encoding.

The mechanism by which tissues are delineated in PC MR is known as a bipolar linear magnetic gradient, applied in the direction of moving tissues, and displayed in Figure 2-5. Over the time course of the bipolar gradient, stationary and moving spins will accumulate different amounts of phase. Application of the first half of the gradient causes a shift in spin phase. In tissues with zero-velocity over the length of the bipolar gradient, the second half of the gradient cancels out the accrued spin phase. This produces zero net phase in static tissues, while spins that move in the imaging volume will accumulate a phase proportional to the velocity of these spins.
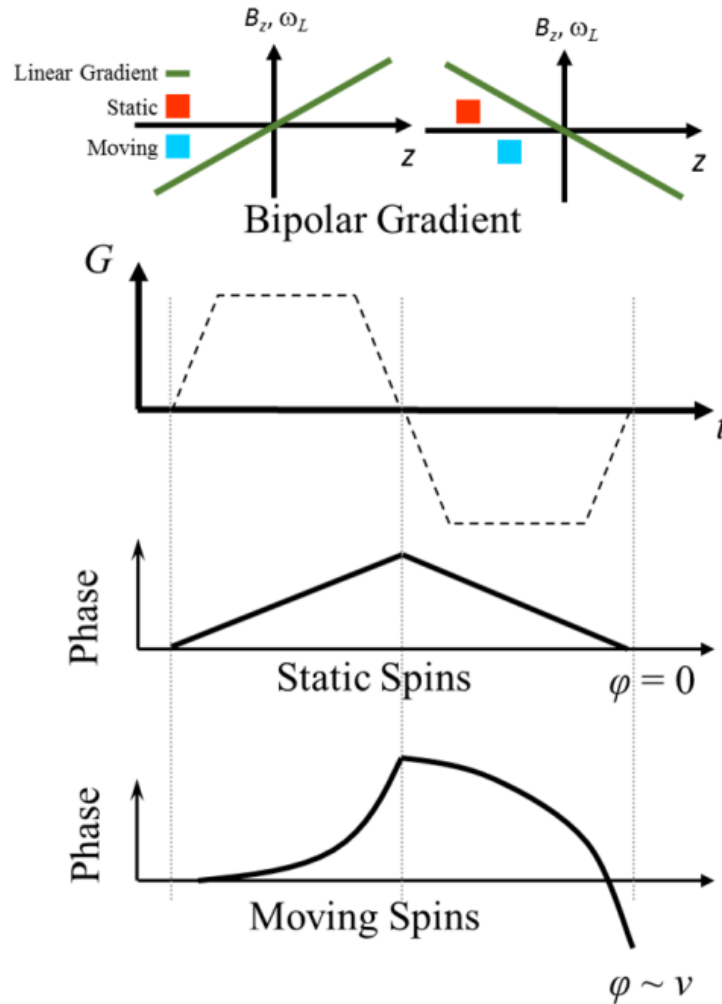
Figure 2-5. A schematic showing the effect of a bipolar gradient on the phase of stationary and moving spins. During the positive first half of the gradient, both static and moving spins accrue some amount of phase. The negative lobe rewinds the phase of static spins, producing a net of zero. Moving spins, which have traversed some distance based on their velocity and the time between positive and negative lobes, do not return to their initial state, accruing phase proportional to their velocity.

The magnitude of the change in phase can be calculated based on the magnitude change in the first moment ΔM_1 of the bipolar gradient and the magnitude of the velocity of the spins:

$$\Delta\varphi = \gamma v \Delta M_1$$

2-7

ΔM_1 is calculated through integration of a single lobe multiplied by the time difference between the lobes, making $\Delta\varphi$ malleable via these parameters.

In 2D PC MR, flow encoding is performed in a single direction, requiring one bipolar gradient. Each encoding of flow through the bipolar gradient requires a corresponding flow-compensated scan to establish and remove background phase (detailed below). As such in 2D there are only two possible states of the velocity encoding bipolar gradient (on/off or positive/negative). An example of 2D PC MR in the aorta is shown in Figure 2-6.
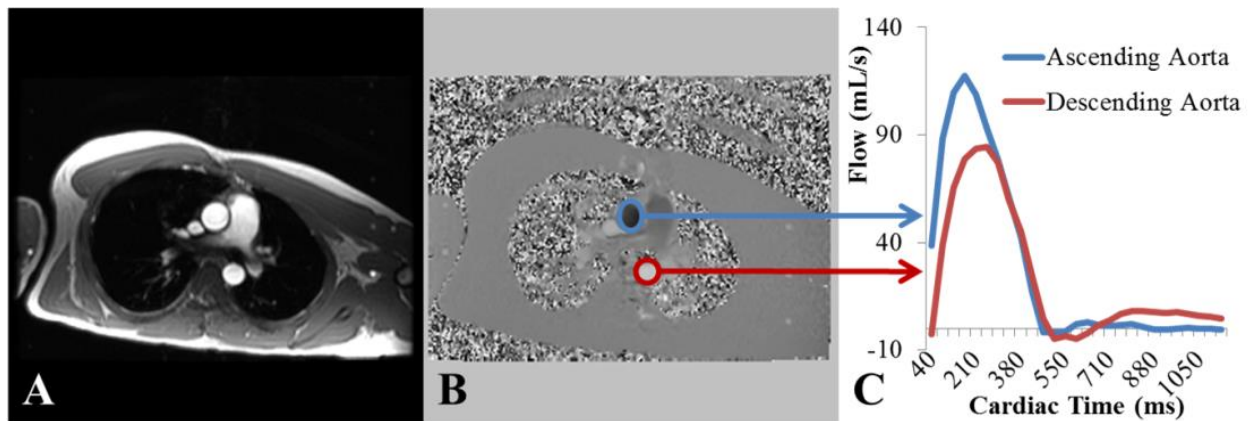
Figure 2-6. 2D PC MR prospectively gated to end-expiration and retrospectively gated to the cardiac cycle in the chest for assessment of aortic flow. Images shown are at end-systole. A: Magnitude images show good vessel enhancement and can be used for vessel segmentation. B: Phase images show flow in opposing directions for the ascending (blue) and descending (red) aorta. Note zero phase (velocity) in static tissues and white noise in air. C: Flow curves over cardiac time garnered from segmentation and integration of velocity of individual vessels.

2.3.2 Velocity encoding

The accumulated phase over the bipolar gradient takes on a unique value only if $-\pi < \Delta\varphi < +\pi$. Outside of these limits, phase wrapping or phase aliasing occurs, in which values will 'wrap' around to $\Delta\varphi \pm 2\pi n$, where n represents the number of 'wraps.' The velocity encoding for the scan, termed the V_{enc}, is described by:

$$V_{enc} = \frac{\pi}{\gamma \Delta M_1}$$

<div align="right">2-8</div>

Velocity v can be found by combining Equations 2-7 and 2-8 to give:

$$v = V_{enc}\left(\frac{\Delta \varphi}{\pi}\right)$$

<div align="right">2-9</div>

Thus, the V_{enc} can be set via M_1 manipulation for an expected maximum velocity within a PC MR acquisition. It is apparent that when velocity exceeds the V_{enc}, phase aliasing can occur. The simple solution to avoiding aliasing is to set the V_{enc} just above the highest expected velocity in the imaging volume. This value cannot be chosen arbitrarily, however, because slowly moving spins accumulate a small amount of phase, leading to smaller PC MR signals and a decrease in the velocity-to-noise ratio (VNR). VNR is inversely proportional to the V_{enc} via:

$$VNR = \frac{\pi v}{\sqrt{2} V_{enc} \sigma_\varphi}$$

<div align="right">2-10</div>

where σ_φ is the noise of the phase measurement. If V_{enc} is too high, velocities may reside below the noise floor of the VNR of a given pixel and velocity measurements would be inaccurate. In clinical settings where vessels with an extreme difference in expected velocities are measured, two separate scans at a high and low V_{enc} are often used, though research has been performed to combine a high and low V_{enc} (dual-Venc) or many V_{enc} settings (multi-Venc) into a single scan (38,39). These scans result in high VNR in all vessels within the imaging volume, yet are hampered by extended scan time.

2.3.3 Phase contrast errors

As shown above, the measurement of phase accumulation and minimization of noise is vital to good image quality and accurate assessment of flow. Magnetic susceptibility, field inhomogeneities, eddy currents, gradient delays, and other effects may all add significant and unwanted phase during PC MR. The most common approach for eliminating these contributions

is termed referenced encoding, and consists of a flow-compensated scan to measure background phase followed by the velocity encoding scan with the same timing parameters. While this encoding scheme compensates for many types of errors, major sources often persist in the form of gradient non-linearity, non-compensated eddy currents, and concomitant gradient fields (40-43).

Velocity encoding depends on the strength and direction of the gradient first moments. The assumption that magnetic gradients vary linearly with distance over their entire area only holds in a small region near the isocenter of the main magnetic field. This assumption is often accurate for 2D PC MR scans, as the imaging slice is prescribed at the magnet isocenter and vessels of interest are placed at the center of the imaging field-of-view (FOV). Gradient non-linearity becomes a concern at greater distances from the isocenter, such as in volumetric 3D PC MR, causing error in both the magnitude of encoded velocities and the velocity encoded direction. A gradient field model in reconstruction corrects spatial distortion, while local gradients are used to rectify first moment misrepresentations (42,43).

Concomitant fields are a result of Maxwell's equations, which imply that uniform imaging gradients are accompanied by higher order spatially varying magnetic fields (44). They are characterized by cross terms of the magnetic gradients (i.e. the longitudinal gradient in the z-direction with a transverse gradient in the x- or y-direction), and result in phase errors. Waveform design considerations can alleviate these phase errors, however this approach generally increases the echo time of the acquisition. Knowledge of the gradient waveforms, coupled with their effects according to Maxwell's equations, are commonly used during image reconstruction to correct for concomitant phase errors (41).

Switching of magnetic field gradients results in fast changes of magnetic flux, thereby causing eddy currents and distorting expected gradient waveforms. Modern scanners have built-in pre-emphasis systems for correction of eddy currents, but not all are compensated completely, specifically eddy currents with short time constants in sequences with short repetition times. In PC MR, eddy currents are produced by the velocity encoding gradient since the actual phase image is formed by subtracting two images with identical timing parameters. Subsequent velocity encodes lead to different eddy current phase changes, so that simple subtraction of phase images does not eliminate these errors.

Three methods are currently used to correct for eddy current phase offsets in PC MR. The first uses the phase in stationary tissue adjacent to the vessel of interest, and corrects all other voxels in the image based on the measured phase angle in the stationary tissue. This method assumes that the phase offset is constant over the image (45) and is implemented as a correction method in commercial flow analysis packages. The second approach employs an interpolated phase map automatically calculated from static tissue points through time. Typically a first- or second-order polynomial function is fit to the phase map for characterization of eddy currents. The third method is used if no tissue is present. A phase-offset can be directly measured from a repeated scan with the exact same scan parameters in a stationary phantom. The correction produces a voxel-wise field map that is accurate wherever there is signal in the phantom and is used to correct for the in-vivo data. This approach creates highly improved measurements but is generally not clinically feasible because of added scan time (46-48).

2.4 4D Flow MRI

2.4.1 Introduction

The majority of the work in this thesis will focus on a variant of the PC MR acquisition sequence, known as 4D Phase Contrast MRI or 4D flow MRI. This technique, consisting of 3-directional velocity encoding that is time-resolved to the cardiac cycle, enables both volumetric angiographic visualization and quantitative assessment of blood flow velocities (49). While the conception of 4D flow MRI dates back over two decades (50), recent advances in hardware, software, and acquisition strategy (some of which are detailed below) have made these sequences reliable and acquirable in manageable scan times of 5 to 20 minutes.

Following the reconstruction of 4D flow MRI, a wealth of information is available, giving rise to a number of quantitative and qualitative strategies for the post-processing of data. The visualization of a dynamic vector quantity over a volume is challenging and easily overwhelming for the human observer. Figure 2-7 displays an example of the available information from a 4D flow MRI scan in cardiac vasculature. Time-averaged velocity fields can be used for visualizations of average velocity streamlines, while time-resolved velocity fields can be visualized with streamlines, velocity-vectors, and particle traces (49). Such visualizations allow for qualitative assessment of potentially abnormal flow throughout the imaging volume averaged over the cardiac cycle, at a single instant (e.g. end-systole), or throughout the cardiac cycle in animated format.

For quantitation of 4D flow MRI data, 2D double-oblique analysis planes are reformatted and placed across the vessels of interest. Flow is calculated by integrating the 3-directional sum-squared velocity field over the vessel area and the cardiac cycle. Additional hemodynamic parameters derived from the velocity fields, such as pressure gradients (51,52), pulse wave

velocity (53,54), kinetic energy (55), turbulence (56,57), and wall sheer stress (58-60), have been

shown to be clinically significant in certain vascular pathologies and provide areas of active and

growing research.
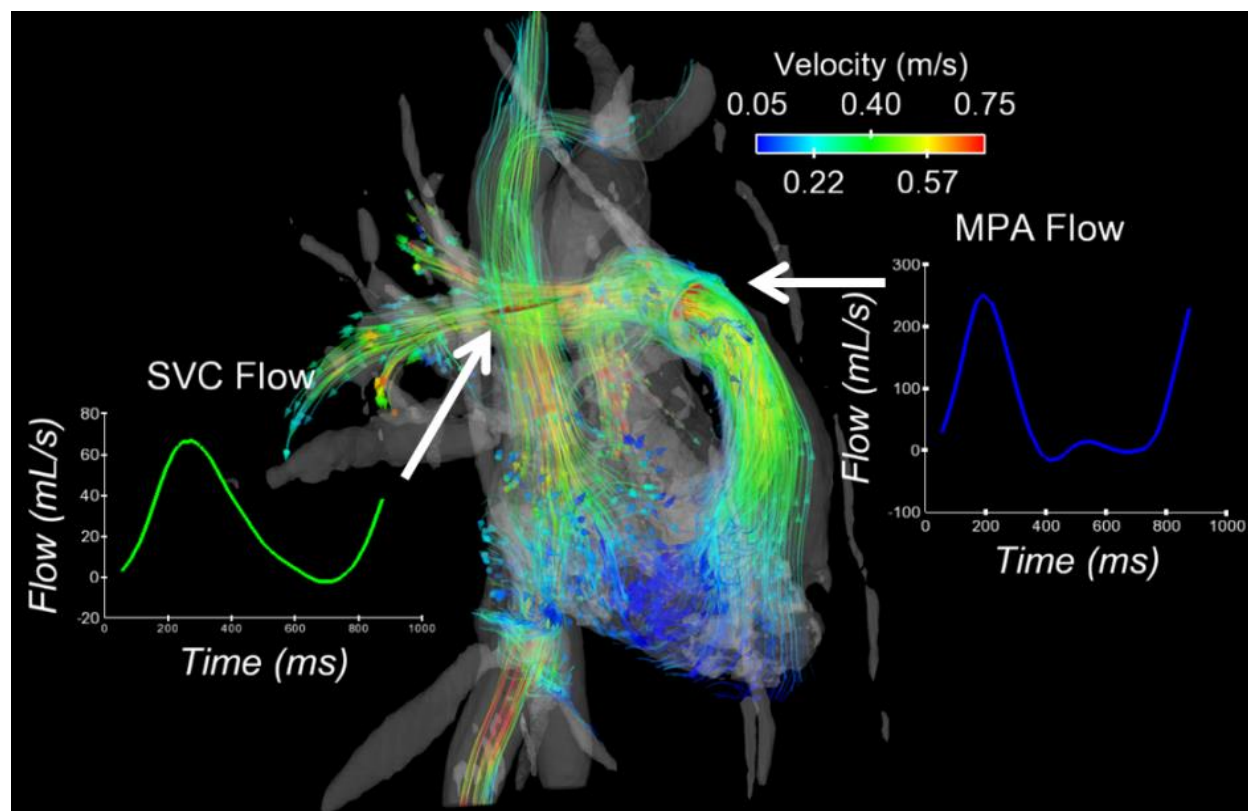
Figure 2-7. Example post-processed 4D flow MRI exam in the cardiac vessels. Velocity streamlines in right-side vessels at specific time-points provide qualitative visual assessment of flow patterns. Two-dimensional cutplanes (white arrows) can be interactively placed in vessels of interest (shown here in the superior vena cava – SVC and the main pulmonary artery – MPA). Integration of velocity values gives characteristic flow curves over the cardiac cycle.

This powerful approach has been explored in a number of vascular systems and

pathologies, both for validation and clinical assessment of disease. These include: peripheral

vessels (61), renal and hepatic vasculature (62,63), intra- and extra-cardiac vasculature

(59,64,65), and intra- and extra-cranial vasculature (i.e. the head and neck) (66-69). The most

commonly studied vessel has been the aorta due to its size and, thereby less challenging spatial resolution requirements and various clinically important hemodynamic questions.

2.4.2 Accelerated 4D flow MRI

K-space considerations

The amount of data to acquire for a given desired FOV or imaging volume and spatial resolution is determined by the Nyquist limit, which is dependent on the highest sampled spatial frequency in k-space and the spacing between successive points. Sampling below this limit is known as undersampling and has negative consequences for image quality and artifacts. An example is shown in Figure 2-8.

To fill k-space with data in the traditional 2D Cartesian (i.e. checkerboard or grid-like, as in Figure 2-8) manner, two orthogonal magnetic gradients must be applied. The first, a frequency-encoding gradient, linearly varies the resonance frequencies of spins along the readout direction. The second, a phase-encoding gradient, is perpendicular to the frequency-encoding gradient and linearly varies the phase of spins. One variation or step in the phase-encoding direction precedes the acquisition of data along an entire line of k-space in the frequency-encoding direction, making phase-encoding much less efficient. The time between (and number of) phase-encoding steps essentially determines the length of the MR acquisition. In a 3D Cartesian scan, an additional orthogonal phase-encoding is added, further increasing the time to fill in k-space and complete the scan. Acceleration of Cartesian acquisition can be accomplished by decreasing the time between successive phase encodes, yet is limited by gradient slew rates, subject heating considerations, and peripheral nerve stimulation.

With recent improvement of hardware design, non-Cartesian trajectories are becoming easier to implement in research settings. Advantages of moving to a non-Cartesian over

Cartesian acquisition are higher sampling efficiency, relative insensitivity to subject motion, and incoherent undersampling artifacts. These trajectories include spirals (70-72), radials (73,74), propeller (75), and others.

As mentioned above, a major hindrance in the clinical implementation and utility of 4D flow MRI lies in the lengthy acquisition required for collection of data. Recall that 2D PC MR requires two scans (flow-compensated and flow-encoded), and allows only for assessment of velocity in a single direction through a 2D slice. To move to 3-directional velocity encoding in a single slice, therefore, a total of four scans are required. For 4D flow MRI, 3-directional velocity encoding is coupled with a volumetric and cine acquisition, vastly increasing the scan time required for full data acquisition. For example, a typical intracranial 3D PC MR (ungated to any physiological signal) scan aims to acquire whole brain coverage with isotropic resolution (320 x 320 x 320 imaging matrix) at a repetition time (TR) of 7 ms, the acquisition time would be:

$$Acquisition\ Time = TR\ x\ N_{phase\ encoding\ steps}\ x\ N_{encodes}$$

$$= 7\ ms\ x\ 320^2\ x\ 4 \approx 48\ minutes \qquad \text{2-11}$$

Evidently acceleration techniques must be employed for clinically feasible scan times with 4D flow MRI. The following will highlight some of these strategies.

Cartesian limitations

In cases where a limited volumetric acquisition or spatial resolution produces the required information needed to make an assessment, such as in aortic disease (76), a simple Cartesian acquisition scheme can be acquired in a reasonable scan time. For larger volumetric coverage or in regions where higher spatial resolution is needed to observe smaller vessels, alternate acquisition schemes or data manipulation must be utilized to mitigate scan time.

In the Cartesian realm, undersampling below the Nyquist criteria often produces ghosting or wraparound artifacts that confound image quality and PC MR velocity measurement accuracy (Figure 2-8). Parallel imaging utilizes information from multiple receiver coils together with measured coil sensitivity profiles to reduce the total sampling time requirements of a scan. A few are frequently used in clinical practice (77,78).

Much research is currently being performed on additional acceleration methods. In k-t GRAPPA (79,80), missing data points are synthesized based on intelligent undersampling patterns both in k-space and through time. This has been shown to produce accurate and repeatable 4D flow MRI measurements with acceleration factors (acceleration over traditional full-Cartesian acquisition) of 3-5. Such acceleration factors provide a means to acquiring data for 4D flow MRI in reasonable scan times, on the order of 8-10 minutes for the aorta or 10-20 minutes for whole-heart coverage. In compressed sensing (CS) (81), some measure of sparseness is promoted in the reconstructed image via a cost function; this is usually presented as a minimization problem to promote data consistency. Relative to 4D flow MRI, CS takes advantage of the relatively sparse nature of images generated via PC MR, in which only selected portions of the image (i.e. vessels) contain most of the generated signal.

Parallel acquisitions can also be coupled with compressed sensing algorithms for much higher acceleration factors. While in their relative infancy, these techniques have been shown to: decrease velocity errors in-vivo while reducing scan time by a factor of 8 (82), increase temporal resolution and accuracy of cardiac output (83,84), and are internally consistent (85). Despite advances, these techniques remain complex and difficult to perform, such that additional assumptions regarding data consistency and computation time become concerns.

Radial Sampling

MRI acquisition can also be accelerated via undersampling using radial trajectories. Radial k-space trajectories involve reading out a projection that passes through the central k-space point. This is often described as a spoke as in 2D. The first reported approach for image encoding in MRI by P. Lauterbur was based on radial sampling (86) but was dropped in favor of Cartesian sampling due to hardware limitations and inaccuracies in the k-space trajectory leading to significant image artifacts. In a fully-sampled 3D k-space, the endpoints of these projections resemble regularly spaced points on a sphere (Figure 2-9). Contrary to Cartesian encoding, radial sampling plays out 2 or 3 simultaneous readout gradients (for 2D and 3D, respectively), effectively eliminating phase encoding and changing the frequency encoding direction with each projection angle. As each projection passes through the center of k-space, low-frequencies are inherently oversampled and high frequencies are undersampled. The resulting artifacts appear as incoherent noise in the image and are generally more tolerable than the ghosting artifact from missing lines in a Cartesian acquisition (Figure 2-8). At the center of k-space, the sampling density is high and a fully sampled radius exists which grows as the number of projections increases.
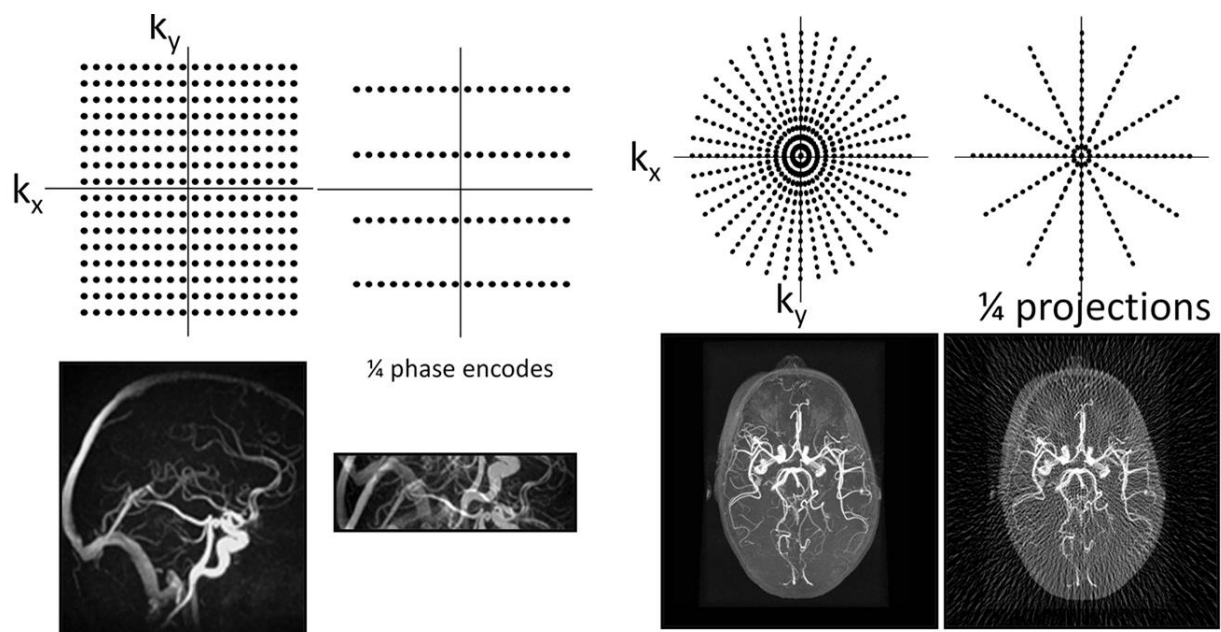
Figure 2-8. Left: Cartesian undersampling in the phase direction. Missing data produces wraparound artifacts which are detrimental to image quality and angiogram vessel conspicuity. Right: Radial undersampling creates incoherent, noise-like artifacts, producing diffuse streaking in the image. (Image courtesy of Dr. Frank Korosec, UW-Madison)
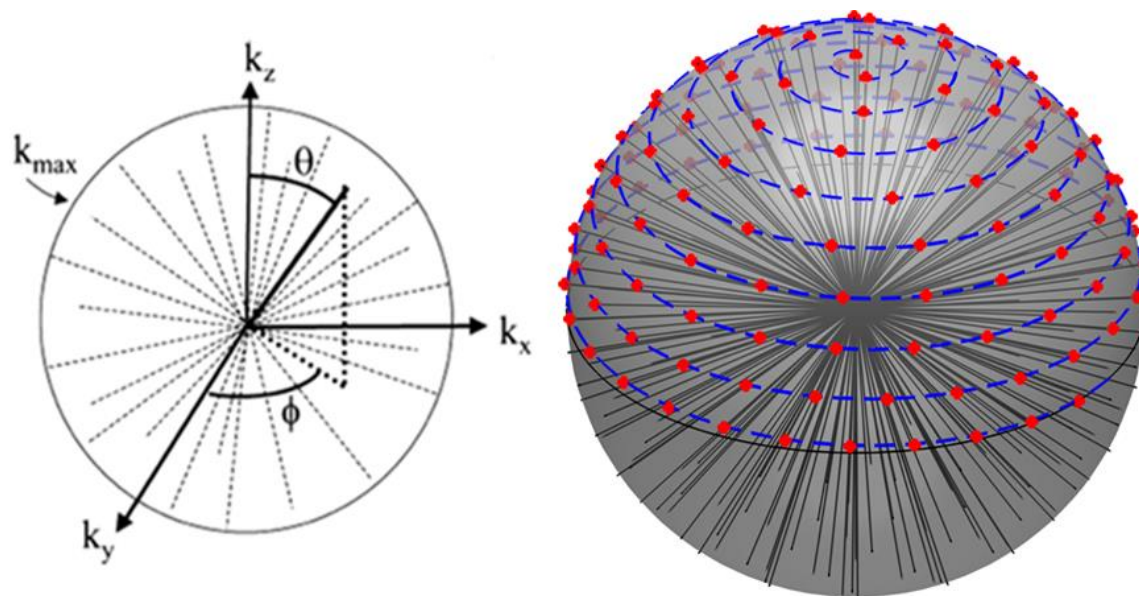
Figure 2-9. 3D radial trajectory. Left: Each projection passes through the center of k-space, and can be described using a spherical coordinate system with radial distance k_{max}, azimuthal angle θ, and polar angle φ. Right: Even distribution of projection origins (red dots) is traced along a spiral (blue line) from pole to equator, achieving relatively even coverage of k-space for a given set of projections.

PC VIPR

The 4D flow MRI technique used exclusively in this thesis, Phase Contrast Vastly-undersampled Isotropic Projection Reconstruction (PC VIPR) (87,88), is an innovative, flow sensitive MRA sequence with a radial acquisition scheme. Due to the high image contrast and sparse signal representation in MRA, PC VIPR has relatively benign undersampling artifacts that yield high spatial and temporal resolution capabilities, important in assessing blood velocity throughout the cardiac cycle. Most prominently, PC VIPR covers a large volume with high isotropic spatial resolution; in the cranial context whole brain vasculature coverage is achieved.

Gating considerations

Equation 2-11 describes the time for acquisition of a non-time-resolved 4D flow MRI acquisition (3D PC MR). In almost any vessel where measurements of blood velocity are desired, a dynamically changing blood flow waveform will be present in the form of a cardiac pulse. Therefore gating of the data acquisition to these signals must be performed to account for cardiac periodicity and the motion of both the heart and chest during respiration. Extra acquisition of data for a given number of cardiac timeframes must be performed to account for these physiological effects.

PC MR data can be either prospectively or retrospectively gated to cardiac and respiratory motion. An example of both methods for cardiac gating is shown in Figure 2-10. Prospective gating tracks the motion of physiological signals during the acquisition. When a threshold in these signals is reached, data is acquired. Threshold values for data acquisition depend on the gating signal, but generally aim to ensure data acquisition at the same point in the cardiac or respiratory cycle (e.g. during cardiac end-systole or respiratory end-expiration). In

Cartesian 4D flow MRI acquisition, prospective cardiac and respiratory gating is preferred. Data acquisition (from triggers) is synchronized with the physiological signal, filling separate k-space lines and frames accordingly. Coupled with parallel acquisitions in which high frequency k-space lines are acquired less frequently than low frequency k-space lines, manageable scan times are achievable.

Retrospective gating is performed by acquiring data throughout the cycle of interest while simultaneously recording the signal. Thus data are continuously acquired unrelated to the physiological state. Trigger points within the physiological cycle, such as systolic peak, are used to sort the data after scan completion, labelling it with a time since last trigger. Data within a certain window (e.g. 100 – 200 ms since last trigger) is pooled after the scan has been performed and reconstructed. Retrospective gating often employs arrhythmia rejection windows on the order of 10-20% to ensure that all reconstructed data has been acquired within a fixed heart beat window. For patients with frequent ectopic beats or unstable heart rates, much data may be discarded, resulting in degraded image quality. Exams must be therefore lengthened for the appropriate amount of data to be collected.

Radial imaging is well-suited for retrospective gating, as arbitrary sets of projections may be chosen for reconstruction of particular time frames. This is due to its high sampling density near the center of k-space and relatively even filling of k-space. These properties allow for flexibility in the reconstruction of retrospectively gated radial data to produce a compromise between image quality and temporal resolution.

Our standard implementation of PC VIPR uses a combination of retrospective cardiac gating, monitored through either ECG signal or a pulse oximeter, and prospective respiratory gating (in anatomical locations where such motion must be monitored or accounted for).
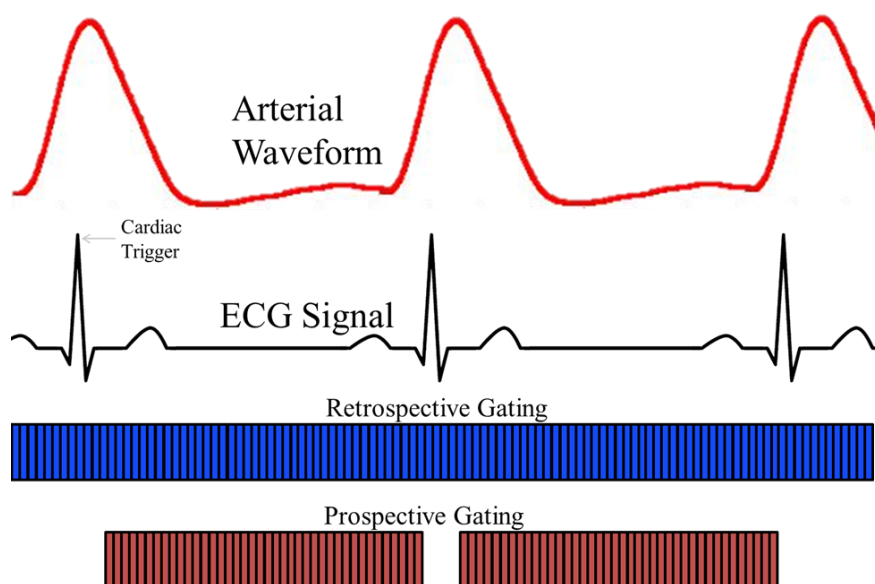
Figure 2-10. Retrospective versus prospective gating example for cardiac applications. The ECG signal triggers at the detection of the peak of the R-wave. Retrospective gating collects data continuously throughout the cardiac cycle and the entire scan, after which data is sorted into phases according to cardiac position. Prospective gating acquires data during a specific acquisition window, so that some parts of the cardiac cycle may be missed.

2.4.3   Intracranial resolution considerations

Much of the discussion concerning 4D flow MRI thus far has centered on regions of the body in which vessels are large, relatively straight, and contain highly dynamic flow over the course of the cardiac cycle. These include the major vessels seen in a 4D flow MRI cardiac scan, such as the aorta, pulmonary arteries, and the superior/inferior vena cava. Due to the relatively large size of these vessels, 4D flow MRI spatial resolution requirements are less stringent than in other areas of the body, such as in the head and neck. An average aorta has a diameter of 2-3 cm (89), so that a 4D flow scan with 1.25 mm isotropic spatial resolution would produce an aorta that is 16-20 pixels in diameter. For the same number of pixels to be present in the internal carotid artery, which has an average diameter of 0.43 to 0.77 cm (90), the required 4D flow spatial resolution would be 0.27-0.32 mm. Previous studies have shown that for 10% accuracy of blood

flow assessment using PC MR, the number of voxels spanning the diameter of a vessel should be at least 5-6 (91). At lower values partial volume effects at the edge of the vessel will produce erroneous flow measurements. This spatial resolution requirement must be reconciled with scan time (see Equation 2-11) and signal to noise ratio, SNR, which in 3D MRI is approximated by:

$$SNR \propto (voxel\ size)\ x\ \sqrt{T_s}$$

2-12

where T_s is the sampling duration. Thus SNR is directly proportional to voxel size, so that a decrease in spatial resolution in all three directions by 1/2 would produce 1/8 or 12.5% of the original SNR.

As a compromise, our standard PC VIPR cranial acquisition covers the entire brain at a spatial resolution of 0.69 mm isotropic resolution, and has been shown to be consistent with 2D PC MR in cerebral arteries and to correlate with pressure measurements in a carotid stenosis animal model (69,92).

Chapter 3: Reproducibility of Cerebrospinal Venous Blood Flow and Luminography using PC VIPR and CE MRA

This chapter presents a test-retest investigation into the reproducibility and reliability of measuring and visualizing venous blood flow. 4D flow MRI of major head, neck, and chest veins is performed and flow is quantified in ten healthy subjects. MRA of the internal jugular veins is scored by two experienced radiologists and compared from day-to-day. The material in this chapter was presented at ISMRM 2012 (1), ISMRM 2013 (2) and is published in the American Journal of Neuroradiology (3).

3.1 Introduction

In the hypothesis attributed to *Zamboni et al.* known as Chronic Cerebrospinal Venous Insufficiency (CCSVI) (93), obstructed venous outflow from the brain and spinal cord promotes tissue iron deposition that triggers the neuroinflammatory cascade of events characteristic of multiple sclerosis (MS). Zamboni published now controversial results claiming 100% sensitivity and specificity in distinguishing MS from non-MS subjects using cerebrospinal venous flow-specific criteria (94). This hypothesis in the diagnosis and potential treatment of MS has raised awareness and increased interest in both intra- and extra-cranial venous flow measurements, namely in the deep cerebral veins (DCVs), the internal jugular veins (IJVs), and the azygos vein (AV). In the wake of invasive venoplasty and stenting (so-called "liberation") procedures being conducted (93) and published results that are contrary to Zamboni's findings (95-98), the CCSVI hypothesis has prompted much discussion concerning accuracy and reproducibility of cerebrospinal venous flow measurements (99).

The diagnosis of CCSVI using the protocol originally designed and implemented by Zamboni employs duplex (gray-scale and color Doppler) ultrasound in the aforementioned veins of interest. Potential issues with ultrasound accuracy and reproducibility are well documented: it is highly operator dependent (with special training required for Zamboni's exam) and blinding of technicians and clinicians to the disease status of experimental subjects is difficult and inefficient, possibly leading to study bias. Additionally, specialized hardware is required for intracranial flow detection through the skull to investigate DCVs, making diagnosis only possible at a limited number of sites. MR can be implemented in the diagnosis of CCSVI to overcome these issues and is already being employed at some sites (100,101). MR has several benefits compared with US: it is well established in MS diagnosis, measurements are far less user dependent (easily repeatable protocols from patient to patient), entire vessels can be assessed non-invasively (including vessels inaccessible to ultrasound), and technician/radiologist bias can be easily removed through blinding. Drawbacks of MRI include: non-realtime, ECG gated acquisitions that last several cardiac cycles, and all measurements have to be conducted in the supine position so that positional flow changes which are part of the ultrasound-based protocol introduced by Zamboni cannot be assessed (94).

While much has been made of the potential diagnosis and treatment possibilities CCSVI has to offer, relatively little effort has been made to investigate the reproducibility of venous blood flow measurement and luminography, especially using MR (102). Owing to the fact that MR flow imaging and MRA have historically concentrated almost exclusively on arteries outside the head, relatively little is known about the accuracy and reproducibility of venous flow assessment with PC MR and venous lumen assessment with MRA. Previous studies have shown that venous flow (particularly in the neck) is sensitive to body position - MR is always supine

(103), head position in which tilt/rotation alters cross sectional area and thus blood flow (104,105), respiratory state - higher flows during inspiration than during expiration (106), hydration level (105), and other contributing factors (103). Venous luminography is additionally difficult to accomplish because unlike rigid, muscular arteries, veins have thin, non-muscular walls that make for an easily compressible and distensible lumen.

The aims of this study were threefold: First, the internal consistency of PC VIPR venous blood flow measurements was evaluated in cerebral veins. Second, the test-retest reproducibility of venous blood flow measurements using PC VIPR was assessed in a healthy volunteer population and compared to test-retest reproducibility of arterial blood flow measurements. Finally, the image quality and reproducibility of venous luminography using CE MRA was assessed.

3.2 Materials and Methods

3.2.1   Experimental subjects and study design

Under an IRB-approved protocol, ten healthy adult volunteers (7F, age 36 ± 14 years) underwent anatomical (CE MRA) and flow-sensitive (PC VIPR) MRI on a 3T clinical scanner (Discovery MR750, GE Healthcare, WI, USA). Each subject was scanned twice on separate days in a test-retest fashion (14 ± 9 days between scans), yielding ten matched pairs of acquired exams. Subjects were selected to exclude any known vascular, neurologic, or psychiatric disorders.

3.2.2   Data Acquisition

A 3-station PC VIPR exam was performed in the head, neck and chest to obtain flow measurements in the cerebral veins, IJVs, and AV, respectively. Cardiac triggers were recorded for retrospective cardiac gating. Sample MRI parameters for the PC VIPR head scan were: 3D

radial free-breathing acquisition, repetition time TR = 15.9 ms; flip angle $\alpha = 25^0$; FOV = 24 x 24 x 16 cm3; acquired spatial resolution = $(0.6 \text{ mm})^3$, scan time: 7 minutes 30 seconds. Velocity (encoding) sensitization was set at 20 cm/s for head and chest scans, and 70 cm/s for neck scans. Since the purpose of this study was to examine the reproducibility of cerebrospinal venous blood flows under normal conditions, the aforementioned potential confounds such as hydration, meal challenge, etc. were not controlled.

A 2-station CE MRA exam (same locations as neck and chest PC VIPR above) consisted of a single injection of gadofosveset trisodium (Ablavar, Lantheus Medical Imaging, MA, USA) at a dose of 0.03-0.05 mmol/kg and a rate of 3 mL/s. Ablavar binds to serum albumin, giving longer intravascular presence with less loss to extracellular space. This unique property of blood-pool contrast agents allowed for a single injection to be used for all CE MRA and PC VIPR exams (5 separate scans in all), with less contrast volume and higher prolonged signal than would be needed using extravascular contrast agents.

3.2.3   Data Analysis

Twenty phase contrast time frames were reconstructed for each PC VIPR scan, giving velocity and magnitude images gated to the cardiac cycle. 3D image sets were segmented using commercial software (*Mimics*, Materialise, Belgium) and exported using an in-house magnitude and velocity conversion tool (*Matlab*, The MathWorks, MA, USA). Velocity data were then visualized (*Ensight*, CEI Software, NC, USA) and measured over the cardiac cycle (107) at specific 2D cutplanes retrospectively selected. To quantify reflux, percent retrograde flow (%RF) was calculated as total negatively directed flow (away from the heart) divided by total positively directed flow (toward the heart) over the cardiac cycle. Total flow (Q, in mL) was also calculated as the integration of mean velocity over the cardiac cycle of the cross sectional area of the vessel.

Cerebral Veins

The accuracy and reproducibility of PC VIPR has been established in arteries, specifically the carotid and cerebral arteries (108), aorta (109), liver (62) and renal arteries (110), but it had not been investigated in veins. As an initial test of internal consistency, a conservation of mass (COM) criterion was applied at the confluence of venous sinuses, or torcular herophili (Figure 3-1a). COM requires that total flow entering and exiting the confluence over the cardiac cycle must be equal. Figure 3-1a also shows the placement of 2D cutplanes used for these COM measurements: in the straight sinus (SRS, red arrow), superior sagittal sinus (SSS, green arrow), and the left and right transverse sinuses (LTS, RTS, yellow arrows). Example blood flow waveforms for these 4 vessels are shown in Figure 3-1b. Thus the COM formula to test becomes:

$$Q_{SRS} + Q_{SSS} = Q_{LTS} + Q_{RTS} \qquad\qquad 3\text{-}1$$

Twenty (two scans for each volunteer) inflow and outflow measurements were compared to internally validate Equation 3-1, with mean percent difference between inflow and outflow averaged over all volunteers. Inter-scan reproducibility of flow measurements in the same 4 veins was tested (scan 1 versus scan 2) using Bland-Altman analysis (111). Finally, percent retrograde flow (%RF) over the cardiac cycle was determined for the same 4 veins as well as for the visualized DCVs.
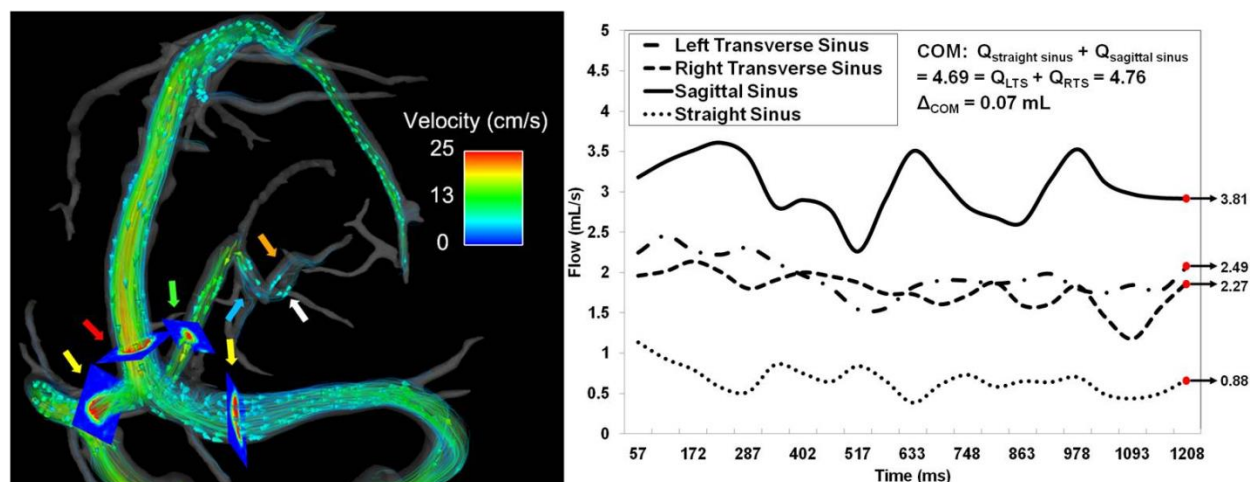
Figure 3-1. Example of flow visualization for COM (A). Arrows: yellow indicates left/right transverse sinus; red, sagittal sinus; green, straight sinus; blue, vein of Galen; internal cerebral veins: left (orange), right (white). Planes mark location of flow measurement. Blood flow waveforms (B) exemplify COM at the torcular herophili, with total flow measurements differing by only 0.37%.

Internal Jugular Veins

IJV flow measurement reproducibility was assessed. Similar to the analysis performed by Haacke (ms-mri.com), 3 measurement planes were placed along the length of a centerline cubic spline. Measurements were taken at the level just below the jugular bulb (upper), at the midpoint of the spline (mid), and just above the IJV junction with the subclavian vein (lower). An example 3D rendering and placement of planes along the spline are shown in Figure 3-2 (left). Interscan Bland-Altman 95% LOA and biases across all levels and volunteers were calculated. Figure 3-2 (right) shows sample IJV blood flow waveforms for each location (left), with detection of retrograde flow in the lower measurement plane. Comparing this lower waveform with a Doppler ultrasound–acquired jugular flow waveform (Figure 3-3), PC VIPR is capable of resolving, both spatially and temporally, the triphasic flow waveform typical in the IJV.
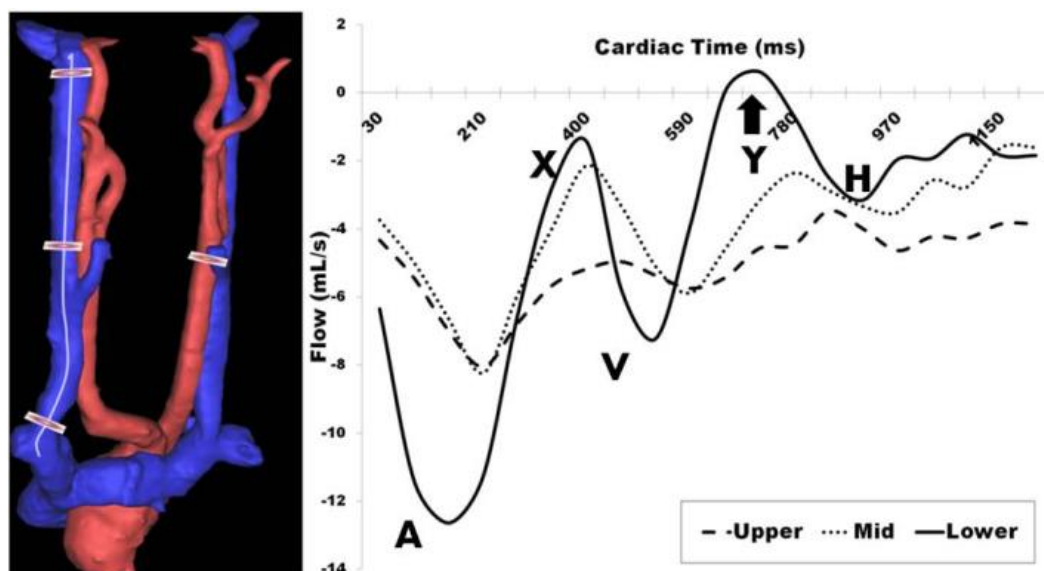
Figure 3-2. Left: Example placement of measurement planes in the right IJV down a centerline cubic spline and in the left common carotid artery. Right: Blood flow waveforms over the cardiac cycle indicate increasing pulsatility proximal to the heart, with a portion of the lower waveform showing retrograde flow (arrow). A indicates atrial systole; X, atrial relaxation; V, ventricular systole; Y, tricuspid reopening; H, atrial refilling.
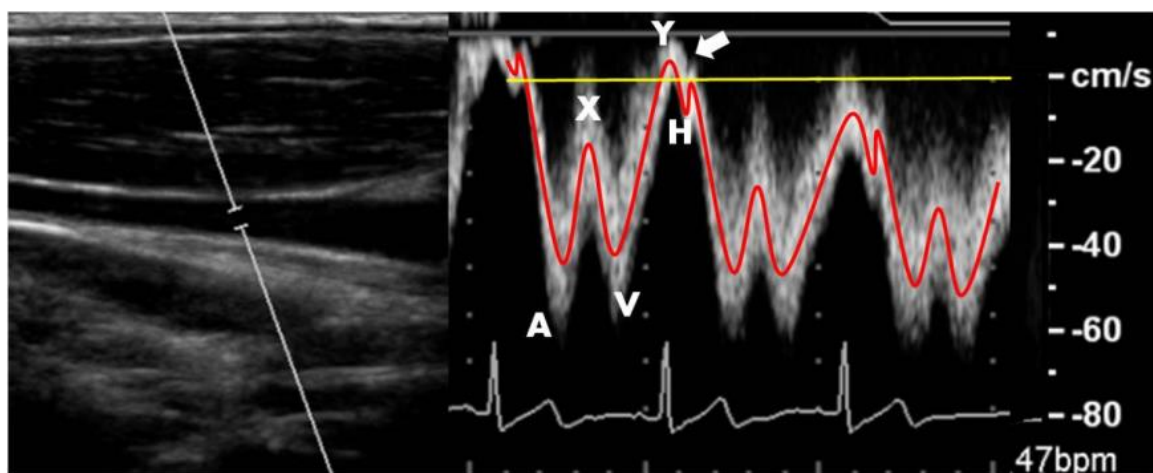
Figure 3-3. Left: B-mode anatomic location of right IJV blood flow. Right: Doppler ultrasonography displays triphasic IJV blood flow waveform as indicated in Figure 3-2. Arrow indicates minor normal reflux during the tricuspid valve reopening.

Azygos Vein

As the primary outflow route of blood from the spinal cord in the upright position, Zamboni considered the detection of narrowing in the AV using invasive venography to be an inherent corollary of CCSVI (93). MRI allows non-invasive assessment of the AV. From the chest PC VIPR scan, measurements of %RF were taken 2 centimeters from the AV junction with the superior vena cava (SVC) and were compared between scans within each volunteer.

Venous/Arterial Comparison

To compare blood flow changes from one scan to the next throughout the cerebrospinal venous system, Q was measured in several locations: in the TS, the 'Upper' and 'Lower' IJV and in the AV. To summarize flow in the cerebrospinal venous system, total flows were added from the left and right TS as well as from the left and right IJVs, providing total venous drainage at a single S/I location. Flows through the common left and right carotid arteries (CCA) were similarly analyzed in order to compare arterial and venous reproducibility across all volunteers. Percent change, calculated as inter-scan difference in total flow from normalized to scan 1 flow, was calculated at all locations. This metric was chosen to identify measured inter-scan changes. Average percent difference between scans and paired t-test p-values were calculated across all volunteers.

CE MRA

To assess the reproducibility of semi-quantitative assessments of venous caliber, CE MRAs were scored by two experienced radiologists blinded to subject identity, date/sequence of scan, and each other's scores. The scoring followed the scaled introduced by Zivadinov et al. (112): ability to assess the IJV and AV (1-poor, 2-acceptable, 3-good, 4-excellent), AV morphology (1-diffusely irregular/narrowed, 2-focally narrowed at central aspect, 3-caliber

increasing from peripheral to central), and IJV morphology at its narrowest point (1-absent, 2-pinpoint, 3-flattened, 4-crescentic, 5 ellipsoidal/round). Cohen's kappa with linear weights was used to assess agreement between ratings in scan 1 and scan 2 (with both readers combined), and between readers (both scans combined). Kappa (κ) values were computed with the irr package (*R,* R Development Core Team, Austria).

3.3 Results

Cerebral veins

Bland-Altman plots of cerebral venous flow measurements between scans within an individual volunteer and for individual vessels are shown in Figure 3-4. A modification of Bland-Altman analysis accounting for repeated measurements within a subject was used for LOA calculations. Inter-scan LOA for Q across all 20 scans (40 vessels) were small with respect to the mean (-2.924, 3.369 mL). Figure 3-5 displays Bland-Altman plots for COM analysis. COM LOA across both scans were also small (scan 1: -2.202, 1.914 mL, scan 2: -1.717, 0.922 mL), with the average percent difference between inflow and outflow equal to 2.2%. All visualized vessels of interest yielded zero retrograde flow (%RF = 0).
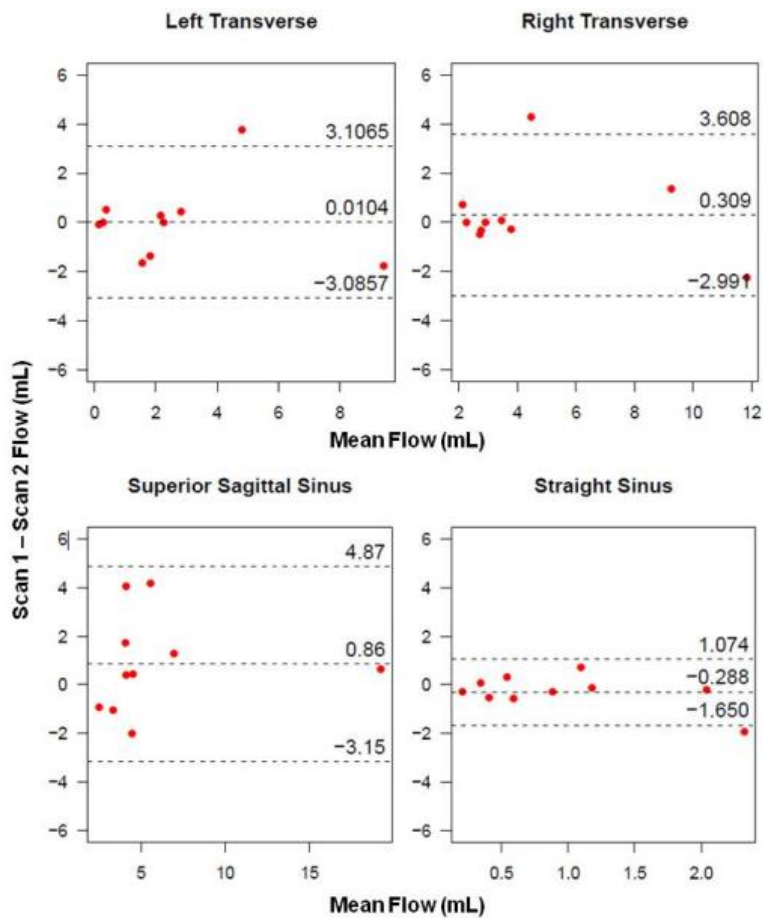
Figure 3-4. Interscan Bland-Altman plots for cerebral vein analysis within individual veins. Small biases and LOA indicate reproducibility of PC VIPR in assessment of cerebral venous flow.
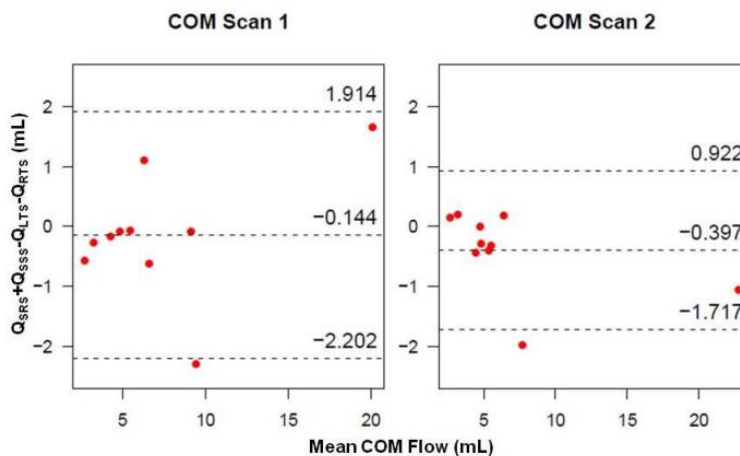
Figure 3-5. Bland-Altman plots of COM analysis for scan 1 (left) and scan 2 (right), showing small biases and LOA.

Internal Jugular Veins

Measurements of Q at each of the three measurement planes along the length of each IJV are presented in Table 3-1. Shaded 'zeroes' indicate no (or negligible) detection of flow at that particular location. Large differences can be observed within single volunteers between scans. Notable asymmetric flow patterns were observed, with complete side dominance in volunteers 1, 3, and 9. Average and peak %RF calculations over all volunteers were computed for each measurement location and are shown in Table 3-1 (bottom row). Both average and peak %RF increase as blood nears the heart. Bland-Altman analysis across all measurement planes yielded inter-scan large LOA in the LtIJV (-2.06, 2.48 mL, bias: 0.21 mL) and in the RtIJV (-5.08, 3.92 mL, bias: -0.58 mL). Inter-scan LOA for %RF in the LtIJV were (-14.187, 13.023 %, bias: -0.58 %) and in the RtIJV were (-10.130, 9.143 %, bias: -0.49 %). Large LOAs relative to the mean are observed, indicating high variability between scan 1 and scan 2 and across all measurement locations.

Volunteer	Left IJV						Right IJV					
	Upper		Mid		Lower		Upper		Mid		Lower	
	S1	S2	S1	S2	S1	S2	S1	S2	S1	S2	S1	S2
1	0	0	0	0	0	0	1.90	8.36	2.00	7.15	3.95	3.07
2	4.36	4.42	4.45	2.80	4.63	4.11	6.03	6.40	4.56	3.34	9.59	8.47
3	3.35	2.63	4.39	1.41	1.99	0.31	0	0	0	0	0	0
4	2.09	2.82	0.80	3.34	2.14	3.70	3.40	3.02	2.99	6.53	2.78	8.75
5	3.89	2.03	1.84	1.74	2.46	1.09	2.37	0.46	2.73	1.86	1.47	0.37
6	1.00	1.68	0.98	1.44	2.26	2.82	3.53	5.37	2.90	4.27	1.39	3.48
7	0.49	0.46	0.82	0.33	0.57	0.50	6.35	4.31	4.91	2.82	5.25	3.63
8	4.18	4.77	3.60	4.01	2.95	4.24	4.54	5.39	3.42	5.72	2.69	5.53
9	2.87	0.74	2.54	1.14	0.64	0.34	0	0	0	0	0	0
10	3.09	3.25	2.60	2.59	1.03	0.99	3.99	3.33	3.75	2.35	1.28	1.19
Average/Max	0.79/6.15		2.98/14.39		6.02/24.59		0.30/4.83		1.19/12.31		3.52/29.46	

Table 3-1. Total flow (mL/cardiac cycle), delineated by side, measurement level, and scan, in all volunteers. Average and maximum retrograde flow percentage is also presented (bottom row).

Azygos Vein

For both scan 1 and scan 2, we were unable to visualize the AV for volunteers 8 and 10. From the remaining 16 measurements, 10 had significant (> 1%) retrograde flow. The average detected %RF among the 8 visualized veins was 7.2%.

Venous/Arterial Comparison

Figure 3-6 includes boxplots of Q, with average percent differences from scan 1 to scan 2. The day-to-day variation in flow in the CCA as measured by PC VIPR was very low (5.1 ± 4.2 %). The venous flow measurements in the IJV and AV showed much larger variations, whereas variations in the TS are much smaller and comparable to those in the CCA (6.8 ± 7.6 %). Figure 3-7 displays percent change in total flows across all head/neck/chest veins and volunteers. Eight

of ten (8/10) volunteers exhibited similar changes (increase/positive or decrease/negative) for 3/4 of the venous flow measurements.
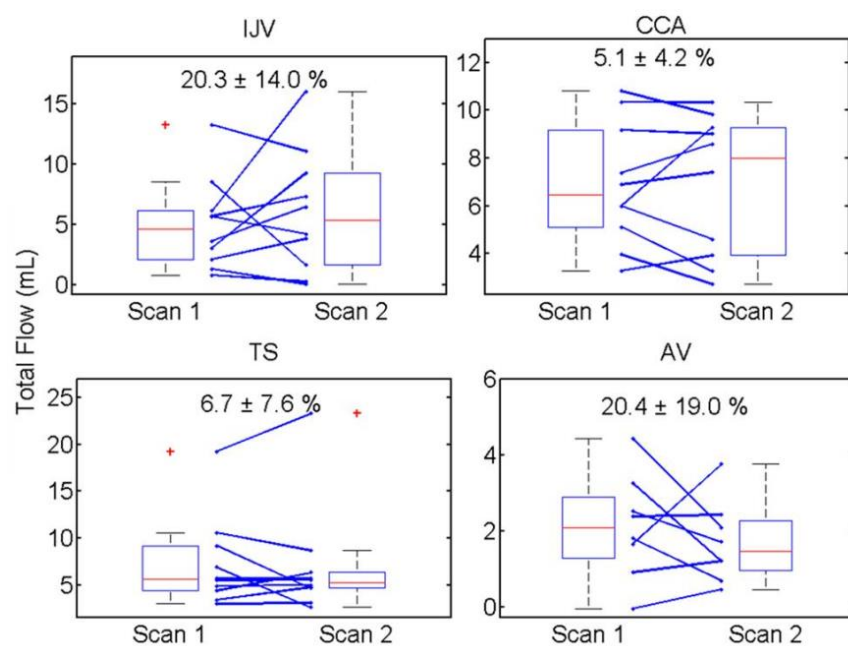
Figure 3-6. Boxplot results for all measurement locations. Individual changes (blue lines) show high variation in both the IJV and AV from scan to scan. No differences were considered significant ($p < .05$).
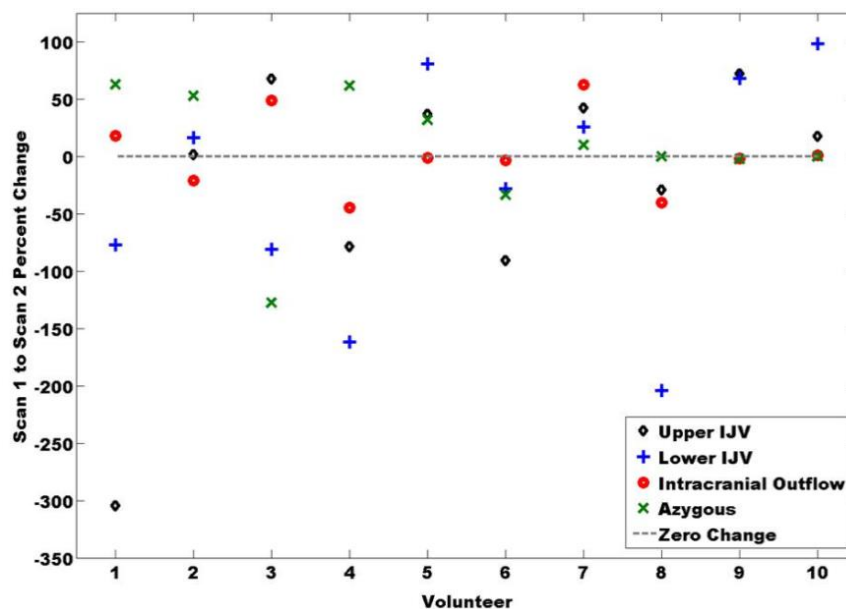
Figure 3-7. Percent change in total flow from scan 1 to scan 2 across volunteers. Volunteers 5–10 have similar directional changes in all measurements.

CE MRA

Scoring average for all acquired scores along with Cohen's kappa for the blinded radiologists' scoring of the CE MRAs are presented in Table 3-2. Higher variation for morphology scores are observed. Inter-scan results pooled for both radiologists indicate fair agreement for LtIJV and RtIJV Morphology, and slight to no agreement for the other three scores. Inter-rater results pooled for all scans show slight to no agreement across all scores.

	IJV Image Quality	Lt IJV Morphology	Rt IJV Morphology	AV Image Quality	AV Morphology
Scoring (Average ± StDev)	3.70 ± 0.56	2.93 ± 1.00	3.40 ± 1.26	3.08 ± 0.89	2.95 ± 0.22
Inter-scan Kappa	-0.064	0.474	0.366	0.202	-0.053
Inter-rater Kappa	-0.042	-0.055	0.281	0.104	--

K < 0 : no agreement, 0-0.20: slight, 0.21-0.40: fair, 0.41-0.60: moderate, 0.61-0.80: substantial, 0.81-1: almost perfect

Table 3-2. Average (± stdev) scores from CE MRA from both radiologists and across all scans. Inter-scan and inter-rater agreement is slight or non-existent across scoring.

3.4 Discussion

As demonstrated in Figure 3-1, PC VIPR allows for flow visualization and quantification in the cerebral venous system, including the relatively small DCVs such as the internal cerebral veins. With PC VIPR the user can retrospectively select vessels to interrogate after the scan, unlike traditional MRV methods that require selecting a limited subset of vessels a priori. Sample cerebral venous flow waveforms in Figure 3-1b satisfy COM over the cardiac cycle. Waveforms show little variation through time, indicating low pulsatility far from the heart in the cerebral veins.

From the Bland-Altman analysis in each cerebral vessel (Figure 3-4), biases fall near the difference of zero, indicating that no consistent bias from the two independent measurements of vessel flow was detected. Tight inter-scan LOAs with respect to mean values across all vessels provide evidence of reproducibility in PC VIPR measurements of cerebral venous blood flow. In COM analysis (Figure 3-5), the small inter-scan average difference in the cerebral vessels (2.2%)

and the tight LOAs are further evidence of reproducibility of intracranial venous blood flow measurements using PC VIPR. To our knowledge, this validation of internal consistency by a COM test is the first of its kind in venous vasculature using PC VIPR. It points to the use of PC VIPR as a reliable measurement tool for venous blood flow. Although many variables have been shown to affect the measurement of extracranial venous blood flow, our findings indicate minimal effect on the reproducibility of intracranial venous flow. This finding may be useful in future CCSVI studies, or in other venous blood flow related pathologies such as cerebral venous sinus thrombosis or idiopathic intracranial hypertension.

The tortuous and varied nature of the IJV, within a single volunteer and across a healthy control population, causes difficulty in measuring blood flow at various locations along its length. PC VIPR is ideal as a 4D flow retrospective measurement tool for this vascular territory. Figure 3-2 (left) demonstrates using a centerline cubic spline in placing of measurement planes, permitting measurements orthogonal to the expected direction of true flow. Figure 3-2 (right) reveals differing pulsatility that S/I locations along the IJV exhibit. Each flow waveform is triphasic in nature. As we move closer toward the beating heart, and incidentally to locations where the IJV is directly adjacent to and often physically touching the CCA, the IJV exhibits greater pulsatility. The 'Lower' waveform of Figure 3-2 (right) exhibits retrograde flow over a short period of the cardiac cycle. This triphasic waveform is expected, corresponding to variations in carotid pulsatile motion (113). An independent Doppler US of the IJV (Figure 3-3) confirms the triphasic waveform and minor retrograde flow seen in a normal, healthy volunteer.

In analyzing retrograde flow over the cardiac cycle (Table 3-1, bottom row), average and peak %RF increase as we measure in the superior to inferior direction. Larger %RF is due in part to the greater pulsatility observed in 'Lower' measurement planes across our healthy subjects, and

may reflect a normal result of greater oscillations in blood flow proximal to the beating heart. Other factors may contribute to retrograde flow seen in a healthy population, such as IJV valve incompetence (114). Despite this finding, most of the measurement planes experienced less than 1% retrograde flow for all locations (81/120), indicating the strong tendency of constantly anterograde blood flow throughout the cardiac cycle within the IJV.

Table 3-1 illustrates wide variance of Q values and varying side dominance in the IJV in a healthy control population, confirming earlier work (115). The unpredictable nature of venous anatomy and blood flow characteristics are relevant as they convey difficulties likely to be encountered in clinical situations. Considering the variables that were not accounted for in this study, the inter-scan heterogeneity within a volunteer should be expected, yet is contrary to previous work (116). This work points to the need for controlling of variables that may affect venous return.

The Bland-Altman results for the IJVs indicate that there are no systematic differences between test occasions. The small biases (left: 0.209, right: -0.58) between scans again lend support to the reproducibility of PC VIPR; however, large LOAs and spread in the data indicate that flow in the IJVs is not repeatable within subjects. Error proportional to the mean was observed in the inter-scan %RF Bland-Altman analysis.

In the AV, high variability in %RF was seen. Notably, visualization of the AV using PC VIPR is difficult due to cardiorespiratory induced motion. Indeed, of the 20 chest PC VIPR scans taken, the AV was reliably visualized 80% of the time. The significant average %RF (= 7%) additionally suggests that retrograde flow may be a normal supine attribute of the AV measured 2 cm from its junction with the SVC. This non-invasive probing of AV flow exemplifies another benefit of using PC VIPR.

Individual variations of flow on Figure 3-6 reveal inter-scan consistency in CCA flow. The low arterial variation (5.1 ± 4.2 %) confirms both physiologic reproducibility of arterial flow and technical reproducibility of PC VIPR. Small variation (6.8 ± 7.6 %) was also observed in the TS, indicating comparable cerebral venous flow reproducibility. In contrast, large variations in neck and chest venous flow (> 20%) were observed, logically resulting from inter-scan physiologic changes. Figure 3-7 confirms these changes systemically affecting cerebrospinal venous blood flow. The number of similar, one-sided changes across the veins indicate a physiological (i.e. not technical) change. These results strongly point to controlling for venous flow altering variables.

The scoring results from the CE MRA analysis (Table 3-2) indicate good image quality for both the IJV and AV, with higher values for the IJV (3.70 ± 0.56 vs. 3.08 ± 0.89). This difference is likely a result of the mitigating motion in the chest during prospectively gated respiratory exams versus the stationary neck exams. AV caliber increased as it neared the junction with the SVC. Turbulent flow from the much larger SVC increases the venous lumen in the AV near its junction with the SVC. Left and right IJV morphology scores had higher variances (3.0 ± 1.1 and 3.7 ± 1.3). These results are expected given the demonstrated differences in IJV flow across a healthy volunteer population. Single volunteer variation is corroborated by observing the low agreement from the inter-scan kappa values. Low inter-rater agreement in the presence of good image quality points to a lack reproducible identification of IJV and AV morphology, due in part to the varied sizes and shapes of venous structures across a healthy population.

This study is not without its limitations. First, some chest scans and resulting AV image quality were quite poor but still usable. This is a direct result of breathing effects purposefully not accounted for in each of the PC VIPR scans, and may have caused the lack of either

visualization or measurable flow in the AV for volunteers 8 and 10. Second, to mitigate on the table scan time for each volunteer, Venc optimization was not performed prior to the PC VIPR scans. No phase aliasing was observed for any of the 60 PC VIPR scans, though low velocity in some of the IJVs caused the velocity to noise ratio to suffer, which would have been improved with a lower Venc setting in these cases. Finally, results from this study differ from extracranial venous scoring by McTaggart (117), where a linearly increasing flattening scale (118) was used to score the IJV. Our semi-quantitative approach to venous lumen morphology, though taken from literature (112), made decisions between available choices difficult. This may have led to poor inter-observer and inter-scan agreement (Table 3-2).

In summary, the use of PC VIPR as a reliable measurement tool for assessing venous flow has been demonstrated; however, only the intracranial veins show excellent day-to-day reproducibility of flow measurements, comparable to that of normal arteries. Normal venous flow in the neck (IJV) and chest (AV) is much more variable from day-to-day. This is presumably due to confounding variables related to normal cardiorespiratory and positional effects that are dampened at the level of the intracranial veins. The detection of retrograde flow has been shown to be a normal finding in the lower IJV and AV of healthy volunteers. These findings have important implications in the CCSVI hypothesis in which normal day-to-day variation in venous flow may be construed as diagnostically relevant.

Chapter 4:   Preliminary Results – Multiparameter CCSVI Study

This chapter presents data from a larger CCSVI study that is currently underway at our institution. Patients with multiple sclerosis and age- and sex-matched healthy controls underwent a battery of MRI scans to look at quantitative biomarkers in normal appearing white matter and venous blood flow. After processing of data, subject statuses were unblinded and compared across all parameters of interest. This work has been accepted for presentation at ISMRM 2015 (4,5).

4.1 Introduction

Chronic cerebrospinal venous insufficiency (CCSVI) posits vascular dysfunction to the level of the deep cerebral veins as a possible mechanism for the cause and/or exacerbation of multiple sclerosis (MS). When first described and published as a possible reversible condition related to MS, CCSVI received extremely high attention among patients and physicians. *Zamboni et al.* (93), using extracranial color Doppler US and transcranial Doppler US, found CCSVI in all of their MS patients and zero healthy controls, while simultaneously hypothesizing and testing a simple endovascular treatment that claimed to improve the clinical course of MS (94). Several studies testing the validity of CCSVI hypothesis have been conducted since its original description. The results across multiple imaging modalities have been conflicting.

Minor confirmatory evidence has been published: using Doppler US (112,119) and using susceptibility-weighted MR to detect iron presence in CCSVI positive patients (120).

Refutations of CCSVI are more abundant in literature: using the original criteria from Zamboni with Doppler US (95,98,121), using PC MR in the internal jugular veins (IJV) (122-

124), using a combination of Doppler US and blood-iron metabolism assessment (125), using a combination of Doppler US and PC MR (126), and even using the 'gold standard' technique of catheter venography combined with Doppler US (127).

In comparison with Doppler ultrasound used to diagnose CCSVI, assessment of cerebrospinal venous flow using PC MR has been shown to be reliable (3), is less user-dependent, and allows for a truly blinded study design. 4D flow MRI provides volumetric coverage so that a number of venous structures may be interrogated with a single scan.

Several MR-derived biomarkers are able to detect pathology in normal-appearing white matter (NAWM) of patients with MS, making them potentially more meaningful measures of disease status than conventional T_1- or T_2-weighted lesion load. These include fractional anisotropy (FA) garnered from diffusion tensor imaging, magnetization transfer ratio (MTR) (128), and mean transit times (MTT) from dynamic perfusion data (129).

While a number of the above mentioned studies used a large cohort of MS patients and healthy controls, none have conducted studies into the relationship between the established MR-derived biomarkers in MS brains and the CCSVI criteria laid out by Zamboni. The purpose of this preliminary data analysis was to determine whether MS-related changes in multiparametric MR-derived biomarkers in NAWM would be predicted by venous flow parameters derived from 4D flow MRI in the head, neck, and chest, in MS patients and healthy controls (HC).

4.2 Methods

Demographics

As part of a larger CCSVI study currently underway at our institution, 34 MS patients (Age: 46.7 ± 10.8 yrs, 16M/18F) and 25 age and sex matched HCs (Age: 44.7 ± 12.1 yrs, 12M/13F) were randomly selected for preliminary analysis.

MR Acquisition

A clinical 3T scanner (Discovery MR750, GE Healthcare, Waukesha, WI) was used to collect the following scans: 1) T1 BRAVO (TE/TR/α = 3.2ms/8.2ms/12°, resolution = 0.94x0.94x1.5 mm); 2) T2 CUBE-FLAIR (TE/TR/α = 126ms/6000ms/90°, resolution = 1x1x2 mm); 3) DTI SE-EPI (25 directions, TR = 7400ms, bvalue = 1000 sec/mm^2, resolution = 0.94x0.94x2.84 mm); 4) MT on/off 3D GRE (TE/TR/α = 3.2ms/35ms/5°, resolution = 0.94x0.94x1.5 mm); 5) Dynamic susceptibility-weighted (DSC) perfusion (TE/TR/α = 45ms/1500ms/60°, resolution = 1.7x1.7x5 mm); 6) 4D flow with radial undersampling: PC VIPR head (TE/TR/α = 3.5/9.0/15°, resolution = (0.69 mm)^3 isotropic, Venc = 20 cm/s); 7) PC VIPR neck (TE/TR/α = 3.0/7.9/15°, resolution = (0.86 mm)^3, Venc = 40 cm/s); 8) PC VIPR chest (TE/TR/α = 2.7/6.9/15°, resolution = (1.25 mm)^3, Venc = 40 cm/s). Cardiac triggers were recorded for retrospective cardiac gating; all scans were reconstructed to 20 cardiac timeframes (~ 50 ms temporal resolution).

Image Processing

All image processing was completed by one person uninvolved with image acquisition and fully blinded to group membership. Table 4-1 summarizes biomarkers, as well as MRI scans and software used to generate data. Non-flow data were co-registered with the BRAVO image using FMRIB's Linear Image Registration Tool (*FLIRT*). NAWM and lesions (total lesion volume and lesion ratio, %) were automatically segmented using SPM's Lesion Segmentation Tool (*LST*) with dual inputs of BRAVO (T$_1$-weighted) and CUBE-FLAIR (T$_2$-weighted) images. Values of FA, MTR, and MTT in NAWM were computed using FMRIB's Software Library (*FSL*). For FA, MTR, and MTT in NAWM, a histogram analysis was performed on each subject, resulting in metrics of peak location, peak count, and full-width at half the maximum (FWHM).

	Processing	MRI Scan(s)	Software
NAWM	Lesion Segmentation		
	Lesion volume (mL)	T_1-w, T_2-FLAIR	*SPM, LST*
	Lesion ratio (%)		
	FA	Diffusion Tensor	*FSL*
	MTR	3D SPGR MT on/off	*FSL*
	MTT (s)	DSC-MRI	*FSL*
Flow	Cerebrospinal Veins		
	Total Flow		
	(mL/cycle)	4D flow MRI	*Matlab, Ensight*
	Peak Flow (mL/s)		
	Retrograde Flow (%)		

Table 4-1. Summary of measured quantitative parameters with corresponding MRI scans and processing software.

Flow data image sets were segmented based on the PC angiogram (*Mimics*, Materialise, Belgium) and exported to advanced visualization software (*Ensight*, CEI Software, NC, USA). Flow measurements were obtained from reformatted 2D planes manually placed orthogonally to the direction of flow (107). Figure 4-1 displays anatomical location of the analysis planes: 1) Head – superior sagittal sinus, left/right transverse sinus, left/right internal cerebral vein, and left/right basal vein; 2) Neck – left/right IJV at three stations (Upper, Mid, Lower); and 3) Chest – azygos vein 2 cm from junction with the superior vena cava. Measured flow parameters were total flow (mL/cycle), peak flow (mL/s), and percent retrograde flow (%). In relation to Zamboni's original criteria for detection of CCSVI using Doppler ultrasound (94), our analysis allows for assessment of directional flow in the cervical and intracranial veins (criteria 1 and 2), anomalies/stenoses of IJVs (criteria 3, Figure 4-1C), and blocked outflow in cervical veins (criteria 4). Criteria 5, which identifies cross-sectional area changes in the IJV from supine to sitting positions, was not assessed.
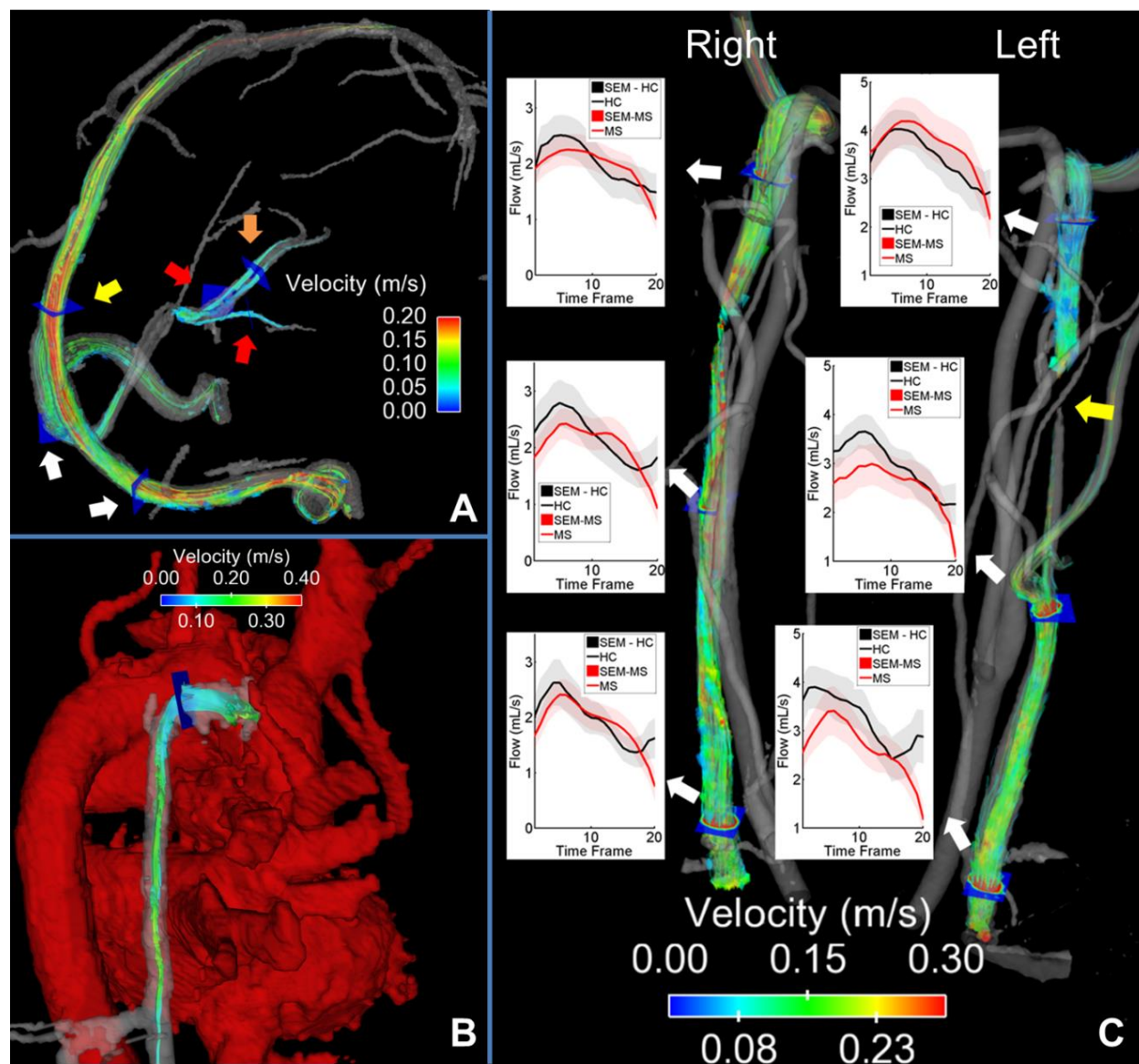
Figure 4-1. Measurement locations and example velocity streamline visualizations in the cerebrospinal vasculature. A – superior sagittal sinus (yellow arrow), left/right transverse sinus (white), left/right internal cerebral vein (orange), left/right basal vein (red); B – azygos vein with heart vasculature in red; C – left/right IJV at upper, mid, and lower. Inset shows average flow waveforms (± standard error of the mean, SEM) at these measurement locations between MS and HC. Note the apparent IJV stenosis observable with 4D flow MRI (yellow arrow).

Statistics

For all quantitative metrics, including NAWM parameters and flow parameters at different

vessels and locations, group differences were assessed on a per-vessel/location basis using two-

sample unpaired Student's t-tests. Values were considered significant at the 5% level ($p < 0.05$). Additionally, parameter relationships were assessed using Pearson's correlation analysis with NAWM lesion ratio (%) used as the control variable to tease out differences between groups (MS = 0.81 ± 0.99 %, HC = 0.03 ± 0.07 %, $p = 0.0002$). False discovery rate control was used to correct for multiple comparisons in NAWM and at different vessel locations (130).

4.3 Results

Example output from NAWM processing is shown in Figure 4-2 – top with lesion identification (red arrow). Figure 4-2 – bottom shows average (± std dev) histogram values for FA, MTR, and MTT measurements in NAWM between groups. In MS patients, lower peak heights and locations for FA and MTR and prolonged MTTs are observed. Corrected t-test *p-values* in NAWM were statistically significant for Lesion Volume and Lesion Ratio ($p = 0.0002$; $p = 0.0002$), MTT peak height and FWHM ($p = 0.0003$; $p = 0.005$), FA peak height, FWHM, and peak location ($p = 0.002$; $p = 0.02$; $p = 0.03$), and MTR FWHM ($p = 0.01$).
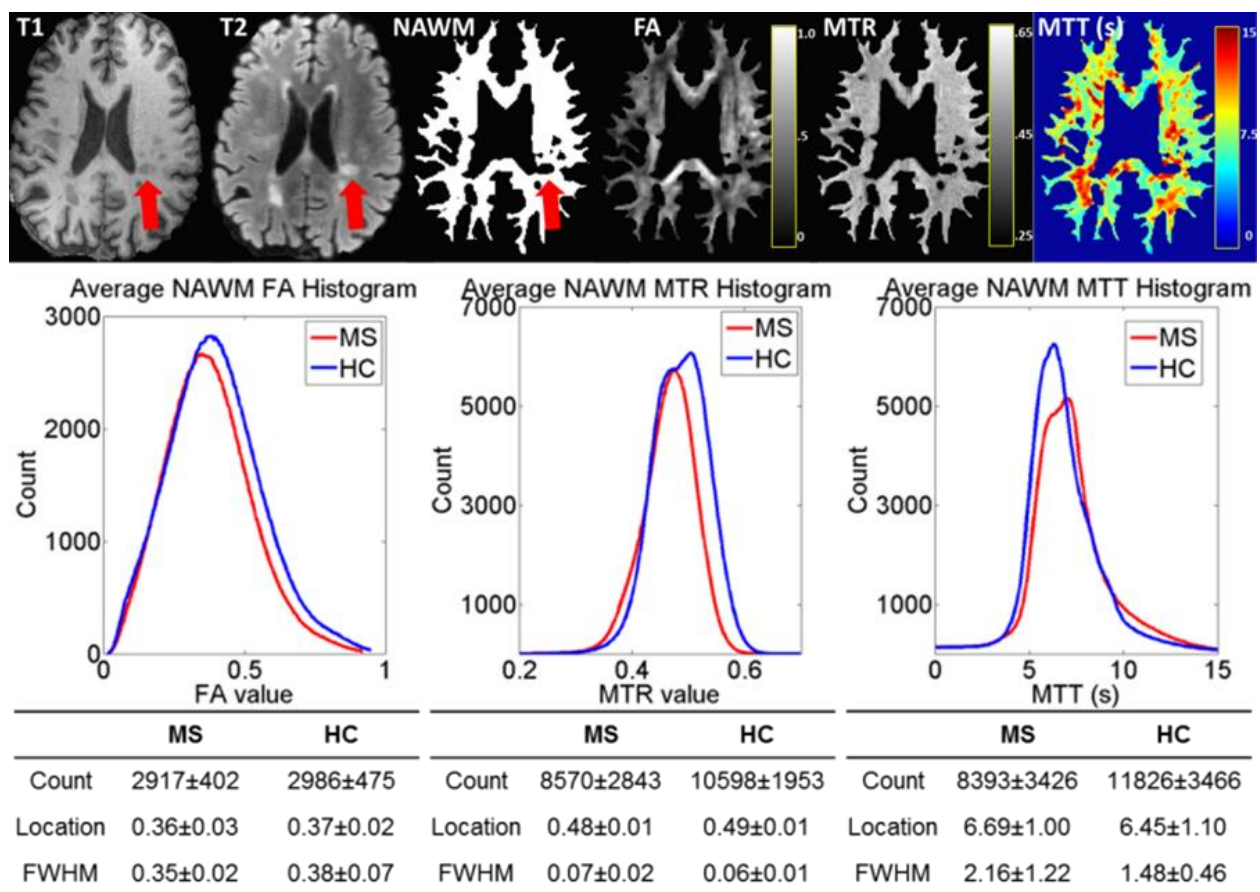
Figure 4-2. Top: Example NAWM segmentation and quantitative processing in a patient with MS. Middle: Average histogram distributions for NAWM metrics for MS and HC subjects for FA, MTR, and MTT. Bottom: Average ± standard deviation results for histogram analysis between groups.

Figure 4-1C displays average flow waveforms (± standard error) over the cardiac cycle for each group at measurement locations within the IJV. Table 4-2 summarizes total flow (mean ± std dev) between groups. No statistically significant differences between the MS and HC were observed for any measurement location, for any tested parameter.

Total Flow (mL/cardiac cycle)						
Head						
	Superior Sagittal	Left Transverse	Right Transverse	Left Internal Cerebral	Right Internal Cerebral	Left Rosenthal	Right Rosenthal
MS	3.2 ± 1.3	2.2 ± 1.7	3.2 ± 1.9	0.3 ± 0.1	0.3 ± 0.1	0.2 ± 0.2	0.3 ± 0.2
HC	3.4 ± 2.3	2.1 ± 1.9	4.1 ± 2.9	0.4 ± 0.2	0.4 ± 0.2	0.2 ± 0.2	0.3 ± 0.2

	Neck - Internal Jugular Vein						Chest
	Left Upper	Left Mid	Left Lower	Right Upper	Right Mid	Right Lower	Azygos Vein
MS	1.7 ± 1.5	1.8 ± 1.5	1.5 ± 1.1	2.8 ± 2.6	2.1 ± 1.9	2.2 ± 2.1	3.2 ± 2.0
HC	2.1 ± 2.7	2.6 ± 3.7	2.2 ± 2.5	3.3 ± 2.4	2.9 ± 1.8	3.4 ± 2.9	3.4 ± 1.5

Table 4-2. Total flow measurements (mean ± standard deviation) between HC and MS subjects across all selected locations. No statistically significant differences were observed for any parameters or locations.

When correlating flow parameters with NAWM metrics, only one was statistically significant (FA peak height, $r = -0.49$, $p = 0.004$). For MS flow data, no statistically significant correlations with lesion ratio were observed for any metric in any vessel. HC flow data exhibited significant correlation at one location only (right internal cerebral vein peak flow, $r = -0.73$, $p < 0.001$).

4.4 Discussion

In this study groupwise multiparameter comparisons for clinical and research sequences were investigated between patients with MS and age/sex-matched HCs for metrics in NAWM and cerebrospinal flow. In agreement with previous studies (128,129), analysis of diffusion, magnetization transfer, and perfusion based metrics revealed statistically significant differences between these groups. In contrast, no flow parameters derived from 4D flow MRI in 14 cerebrospinal vessel segments showed between-group differences.

IJV flow has been shown to have high interscan variability in healthy subjects (3), potentially preventing small between-group flow alterations from being detected without large sample sizes. However, in the intracranial veins, which are necessarily the conduit by which a venous flow disturbance would be transmitted to the brain, flow is much less variable and still no differences were detected.

While this preliminary analysis represents only roughly 25% of the subject data that will be in the final analysis, these negative results do not support a relationship between altered cerebrospinal venous drainage and MS. This is in agreement with a number of non-confirmatory CCSVI imaging studies performed in recent years (95,98,121-127). Processing of larger group numbers and statistical correlation analysis is warranted to describe combinations of NAWM metrics to distinguish MS patients from HCs.

Chapter 5: Respiratory-Induced Venous Blood Flow Effects Using Flexible Retrospective Double-Gating

This chapter introduces a novel simultaneously cardiac and respiratory double-gated PC MR acquisition and reconstruction technique, allowing for assessment of changes in flow caused by respiration. The theory of this technique and results from measurements in the internal jugular vein of a healthy volunteer group are presented. The material in this chapter was presented at the ISMRM/SCMR workshop 2012 (6), ISMRM 2012 (7), and is published in the Journal of Magnetic Resonance Imaging (8).

5.1 Introduction

Phase Contrast (PC) MRI is a useful tool for assessing velocities and flow in larger vessels for clinical and research applications (131). Typical 2D acquisitions with one-directional velocity encoding require cardiac gating to capture variations throughout the cardiac cycle. Breathholds are implemented to compensate for respiratory-induced motion. Recently, 4D flow MRI has become more widespread for volumetric and dynamic capture of the velocity vector field (49). These acquisitions are too long to be completed in a single breathhold; instead, they are usually gated to the respiratory cycle to limit data acquisition to the expiration plateau. Both respiratory motion compensation schemes mask the effects that respiratory-induced intrathoracic pressure changes can have on flow measurements in the chest and nearby venous vascular territories, such as the superior and inferior vena cava (SVC, IVC) (132,133).

Thin, non-muscular, and pliable walls of veins are susceptible to changes in pressure (134). Respiration generates intrapleural (Ppl) and right atrial pressure (P_{RA}) gradients, depicted in Figure 5-1. 1: End-expiration represents the point of greatest positive Ppl. 2: Active inspiration,

with chest expansion and diaphragm contraction, induces a negative pressure gradient. Outside of the chest cavity, this effectively acts as a vacuum, constricting veins and siphoning blood more quickly toward the chest. 3: End-inspiration, when lungs are most inflated, represents the lowest, most negative Ppl and P_{RA}. 4: Active expiration induces diaphragm relaxation, widens the veins and slows venous return.
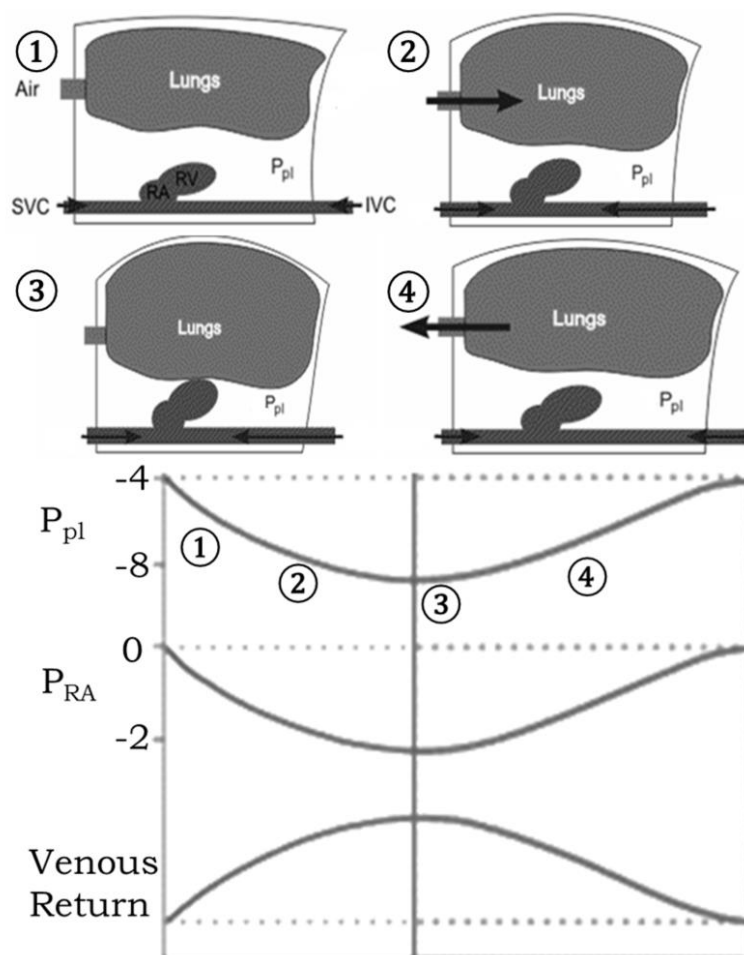
Figure 5-1. Schematic of pressures and venous flow in the chest during the respiratory cycle. During end-expiration (1), the pleural pressure (Ppl) and right atrial pressure (P_{RA}) are at their peaks and the venous return to the right atrium (RA) and right ventricle (RV) through the superior vena cava (SVC) and inferior vena cava (IVC) are reduced. In active inspiration (2), negative Ppl gradient increases IVC and SVC flows, which reach their maximum during end-inspiration (3). Active expiration (4) reverses Ppl and P_{RA} sign, counteracting the increase in venous flow (Adapted with permission from RE Klabunde, www.cvphysiology.com, 2014)

65

Respiration has previously been shown to affect: vessel size of the SVC using serial angiography (132), IVC flow using MR – inspiration flow measured 1.85 times higher than expiration flow (135), and internal jugular vein (IJV) flow using ultrasound (US) – inspiration velocity 29% higher than expiration (136). However, these differences have been generally ignored or are not fully addressed in current clinical MRI because of the complexity and associated prolonged scan time when gating both respiratory and cardiac cycles.

In contrast, several routine US examinations target such changes (137): in constrictive pericarditis and cardiac tamponade for both cardiovascular hemodynamics and function, in evaluation of IVC diameter changes during respiration as a marker for right atrial pressure during transthoracic echocardiograms, and expiratory variation in SVC systolic forward flow as a promising severity index for assessment of chronic obstructive pulmonary disorder. In addition, certain US studies such as venous Doppler flow measurements in the neck are routinely recorded during expiration to ensure reproducibility.

This vascular territory has recently become of interest in the context of the controversial Chronic Cerebrospinal Venous Insufficiency (CCSVI) hypothesis (94). CCSVI hypothesizes that a pathologic reflux of cerebral venous blood drainage causes amplified iron deposition and a neuroinflammatory cascade of events ultimately resulting in Multiple Sclerosis (MS) lesions and symptoms. Although some research into using PC MR for testing of the CCSVI hypothesis has been performed (138,139), little attempt has been made to account for respiratory effect in cerebrospinal venous blood flow.

Here we introduce a novel acquisition and retrospective cardiorespiratory double-gated reconstruction scheme, performed with both 2D (140) and volumetric (87,88) radially

undersampled, velocity sensitive acquisitions. This free breathing approach can provide cardiac gated cine series for multiple phases of the respiratory cycle to 1) provide more consistency of venous flow measurements and 2) to assess the flow differences introduced by the breathing cycle for diagnostic purposes. The respiratory effect on IJV blood flow is investigated in a group of healthy volunteers.

5.2 Materials and Methods

Acquisition

All data were acquired using a high-definition 8-channel neurovascular coil (USA Instruments, Aurora, Ohio) during free-breathing to exemplify flow differences under normal breathing in the supine position. Six healthy volunteers (Age 24-29 years old, mean – 26, 6 males) were imaged after informed consent and institutional ethics review on a clinical 3.0T system (Discovery MR750, GE, Waukesha, WI) using a radially undersampled 2D PC sequence prescribed axially at the level of the carotid bifurcation. Scan parameters were: FOV = 22 x 22 cm, number of projections $\approx$ 10000, 256 points per projection - .86 x .86 mm^2 in-plane resolution, slice thickness = 5 mm, temporal resolution = 12 or 16 cardiac frames (see below), scan time = 3 min, TR/TE = 8.2/4.9 ms, α = 15°, receiver bandwidth = ± 125 kHz, one direction through-plane velocity encoding (Venc) = 70 cm/s. To demonstrate capability of using this technique in 3D, a single 4D flow MRI exam (88) covering the entire IJV was performed in a single healthy volunteer (volunteer 6 from above, age 24, male). Scan parameters were: FOV = (18 cm)^3, number of projections $\approx$ 40000, 256 points per projection - 0.7 mm isotropic resolution, scan time = 17 min, TR/TE = 7.6/2.5 ms, α = 15°, receiver bandwidth = ± 167 kHz, Venc (optimized with 2D Cartesian PC) = 50 cm/s.

Double-gating

Radial projections oversample the center of k-space, allowing for azimuthal undersampling while keeping spatial resolution unchanged at the expense of streak-like artifacts (141). The acquired projections were retrospectively divided into fixed phases based on respiratory waveforms recorded from system bellows placed around the abdomen just below the diaphragm as per standard clinical scan setup. Adequate image quality was maintained by preserving relatively uniform sampling density with pseudo-random projection ordering (141). Data can be subdivided into respiratory phases of different durations, thereby trading off image quality, scan time, and streak-like artifacts. Cardiac timeframes within each respiratory phase are reconstructed with temporal filtering as previously described for time-resolved contrast enhanced MRA with a 3D radial acquisition (142). This is similar to view sharing in a Cartesian acquisition (143).

Three double-gated reconstructions are presented here (Figure 5-2): (a) two respiratory phases (inspiration/expiration plateau) with 16 cardiac timeframes using *a moving average* filter as an adaptive threshold, (b) two respiratory phases (active inspiration/expiration) with 12 cardiac timeframes using the respiratory waveform *gradient*, and (c) *10 respiratory phases* averaged over the cardiac cycle to capture fluctuations induced only by breathing. For the *moving average* reconstruction (Figure 5-2a), a 1D Fourier transform of the bellows signal is calculated to select the average period of respiration. This period is used as the aperture of the moving average filter, subsequently sorting projections into either inspiration plateau (above the moving average) or expiration plateau (below the moving average).

Active inspiration and active expiration (Figure 5-2b) are determined by first finding maxima and minima for the respiratory waveform. These points correspond to end-inspiration

and end-expiration, respectively. Projections near these transition extremes are removed to capture only active portions of the respiratory curve. Because some projections are discarded, a lower number of cardiac timeframes were reconstructed, in this case 12, to preserve image quality. A *gradient* operation then sorts data into active phases.

Finally, reconstruction using *10 respiratory phases* first calculates inspiration peaks over the whole scan. Each breath is then divided into 10 phases containing an equal number of projections. Resulting sorted projections then undergo a time-averaged reconstruction, eliminating cardiac influence on flow. Figure 5-2c demonstrates that generally, phases 2-4 represent active expiration, phases 5-6 expiration plateau, phases 7-9 active inspiration, and phases 1 and 10 inspiration plateau.
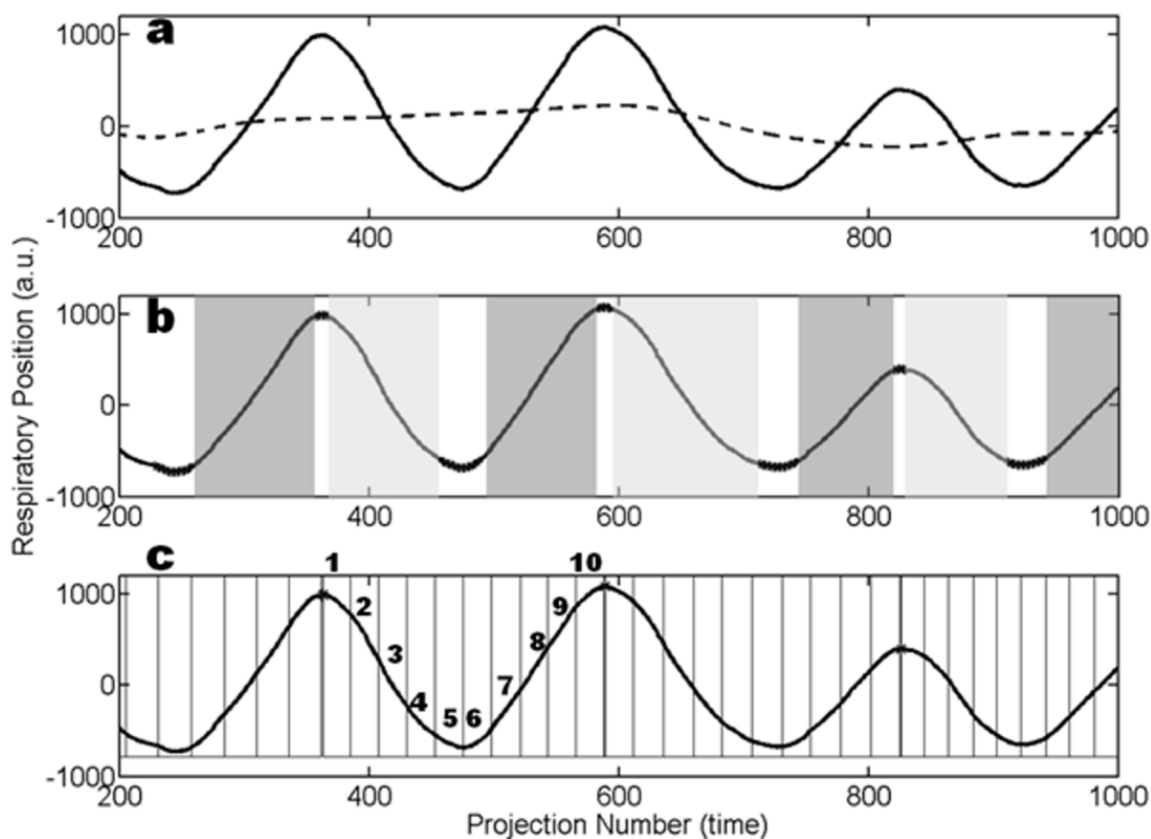
Figure 5-2. Example partitioning of data based on respiratory bellows position; three double-gating reconstruction schemes are used: (a) Waveform (solid line) is split into inspiration and expiration based on a *moving average* filter (dashed line); (b) Respiration plateaus are discarded (markers) and *gradient* operation is performed to give active expiration (light gray shading) and active inspiration (dark gray shading); (c) Equal number of projections are sorted between each peak to give *ten labeled respiratory phases*.

Data analysis

2D data

In *moving average* and *gradient* cardiorespiratory reconstruction methods, blood flow, calculated as mean velocity in a region of interest (ROI) multiplied by ROI area, was measured in the left and right IJV (LtIJV, RtIJV) for each method and each volunteer. ROIs were manually interactively contoured from phase images for all cardiac timeframes using ImageJ (*ImageJ*, U.S. National Institutes of Health, Bethesda, Maryland, USA).

Total flow and peak flow over the cardiac cycle were calculated for comparison between expiration and inspiration phases. As a test of consistency, total flow was also calculated and summed from the right and left internal carotid arteries.

For the *10 respiratory phase* reconstruction, area and velocity measurements were performed in the LtIJV and RtIJV for all phases across all volunteers. Phase at which IJV area was smallest (most constricted) and phase at which mean velocity was largest were calculated.

3D dataset

In the 4D flow acquisition, the *gradient* reconstruction method was used for defining respiratory phases. Commercial software (*Ensight*, CEI Software, Apex, North Carolina) was used to create and place ten equally spaced measurement cutplanes in both the RtIJV and LtIJV. Using a threshold on the complex difference values within each cut plane, mean velocity and peak velocity over cardiac cycle were measured to determine respiratory effect on blood flow as it nears the chest. After averaging values from the LtIJV and RtIJV, percent change from expiration to inspiration was calculated.

Statistical Analysis

For the 2D data using the *moving average* and *gradient* reconstructions, paired t-tests were performed between inspiration/expiration in each method and volunteer to detect presence of statistical significance. This was performed on both total flow and peak flow measurements. Paired t-tests were also performed between inspiration/expiration for the 3D dataset using the gradient reconstruction. These tests were performed on both mean and peak velocity. Differences were considered significant at the 5% ($p \leq 0.05$) level.

5.3 Results

Figure 5-3 depicts representative volunteer IJV 2D PC MR blood flow waveforms based on respiratory position for the three reconstruction methods. In Figure 5-3a LtIJV and RtIJV flows are summed to give a measure of total IJV flow. Differences in blood flow between active inspiration and expiration from the *gradient* method are clearly delineated, whereas flow changes in different plateau positions from the *moving average* method are minimal. Table 5-1 summarizes total IJV flow parameters for all reconstruction methods across all volunteers. The *moving average* method (Table 5-1 left) displays minor, conflicting, and ultimately statistically insignificant results. The *gradient* method (Table 5-1 middle), however, shows a strongly significant increase in blood flow from active expiration to active inspiration across both IJVs for peak and total flow values, which are over 10% for RtIJV, LtIJV, and their summed values. Conversely, summed left and right internal carotid arterial flow percent changes between expiration and inspiration were low and insignificant (*moving average*: 4.4 ± 2.4 %, $p = 0.75$; *gradient*: 2.1 ± 9.7 %, $p = 0.67$).

Figure 5-3b exemplifies anatomical and mean velocity changes caused by respiration alone (cardiac time-averaged) in a single volunteer. Cross-sectional area measurements are highest during end-expiration (phases 4 and 5), while velocity is greatest during active inspiration (phases 7-9). Table 5-1 right summarizes this analysis over all volunteers. On average, the smallest area measurements lie between phases 6.5 and 9 (active inspiration), while largest velocity measurements are during transition from end-expiration to active inspiration (phases 5-6).
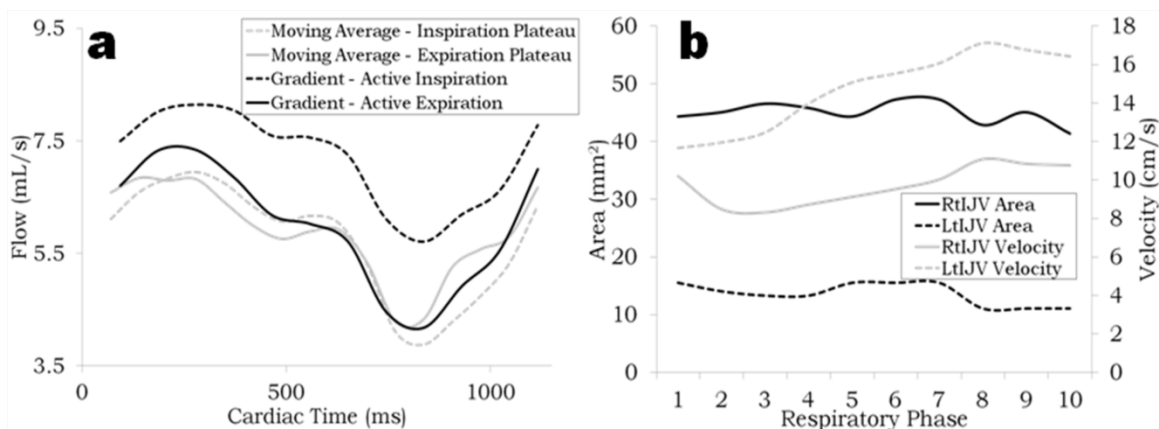
Figure 5-3. 2D radial results from a single volunteer for the three reconstruction methods. (a) Flow in the internal jugular vein over the cardiac cycle for *moving average* (respiration plateaus) and *gradient* (active respiration) double-gating for a single volunteer. (b) *Ten respiratory phases* throughout respiratory cycle with cardiac data averaged. Shown are variations of internal jugular vein cross-sectional and velocity as a function of respiratory phase.

Percent Change (Expiration to Inspiration) Averaged over all Volunteers						Respiratory Phase (mean ± std)			
Recon Method	**Moving Average**			**Gradient**			**Ten Respiratory Phases**		
	RtIJV	LtIJV	Summed	RtIJV	LtIJV	Summed		RtIJV	LtIJV	Summed
Peak Flow	3.3 ± 25.2	6.5 ± 12.4	4.4 ± 9.7	11.0 ± 6.8*	13.2 ± 11.0**	11.9 ± 5.9**	Smallest Area	8.8 ± 1.6	7.2 ± 3.2	6.5 ± 3.6
Total Flow	-0.4 ± 4.7	6.3 ± 5.1	2.0 ± 2.4	13.1 ± 10.0*	13.3 ± 13.8**	11.5 ± 8.0**	Largest Velocity	5.8 ± 2.9	4.8 ± 3.6	6.2 ± 3.2
* p < 0.05, ** 0.001 ≤ p < 0.01									

Table 5-1. Summary of 2D radial double-gating reconstruction methods. Significant percent changes are present for active inspiration/expiration (middle). Active inspiration (phases 5-8, right) represents the smallest area and largest velocity in the internal jugular vein (IJV).

Figure 5-4A illustrates cardiac time-averaged velocity vector plots from the 4D flow acquisition in ten measurement cutplanes along the length of the right IJV. Figure 5-4B shows that magnitude of these velocity vectors is larger during inspiration compared to expiration. Plotted results of mean and peak velocity percent changes averaged between left and right IJV and in each cut plane are shown in Figure 5-4C. Larger average velocity and peak velocity is seen in inspiration compared with expiration. For mean velocity over the ROI and cardiac cycle,

these percent changes were statistically significant (mean: 39 ± 30 %, range: 0 – 93 %, p = 0.001). Greater increases were seen in more inferior planes.
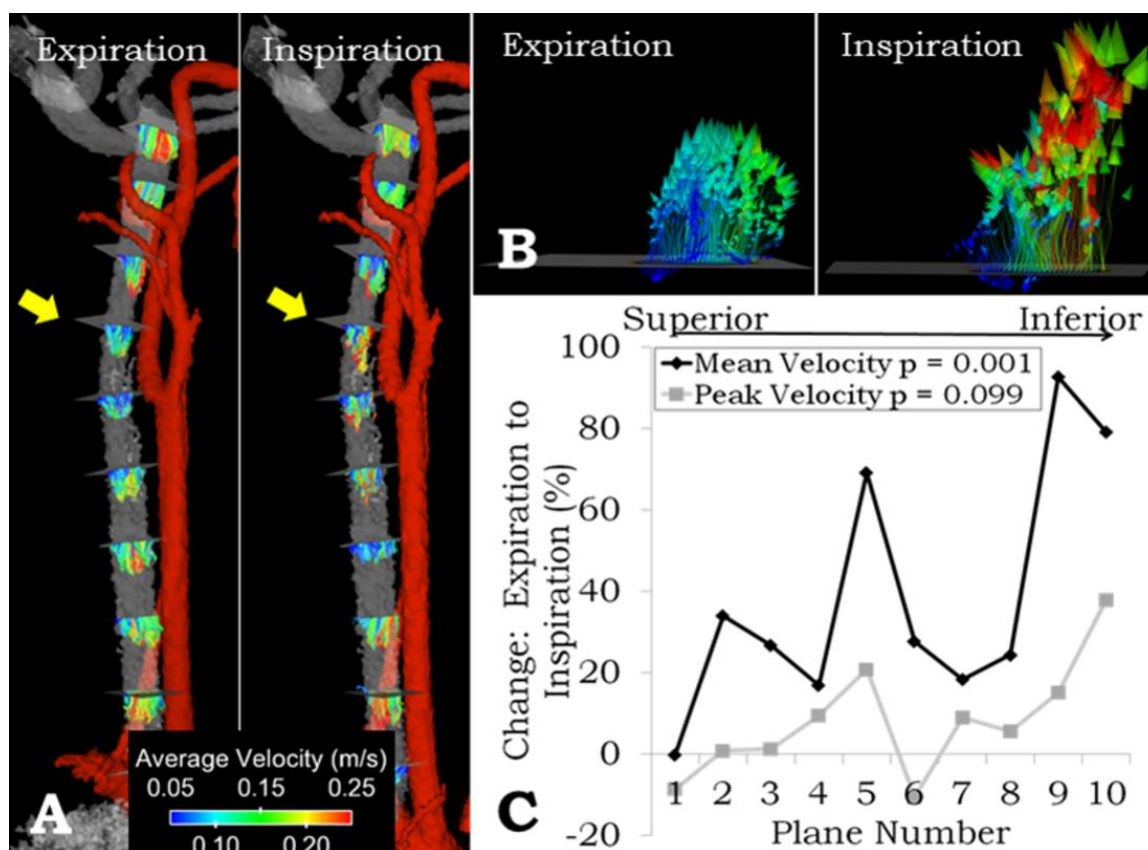
Figure 5-4. Results from the 4D flow volunteer scan. A: 3D whole vessel renderings of the right internal jugular vein and right internal carotid artery (veins in gray, arteries in red) and cardiac time-averaged velocity vector plots. In the superior to inferior direction, ten equally spaced measurement planes are placed orthogonal to the internal jugular vein. B: Selected cut plane visualization from A (yellow arrows) demonstrating increase in velocity vectors magnitude during inspiration. Note also the apparent decrease in cross-sectional area during inspiration. C: Plotted percent changes for both mean and peak velocity across averaged left and right internal jugular vein cutplanes in the superior to inferior direction. Paired t-tests reveal significance (p < 0.05) for mean velocity between respiration phases.

5.4 Discussion

The proposed radial sampling and double gating scheme, in either 2D or 3D, allows for adaptable reconstructions. It provides high flexibility in choosing gating windows after scan completion. Any relevant or meaningful component of the respiratory cycle may be probed.

Combined with our cardiac reconstruction, independent cardiac and respiratory variability can be extracted from the data regardless of the MRI acquisition type. In the cardiorespiratory-resolved technique from *Thompson and McVeigh* (135), raw k-space data is sorted onto a cardiorespiratory phase grid. Images for a certain combination of cardiac and respiratory phase are then reconstructed by convolution with an interpolation kernel for weighting of nearby k-space points. Both this technique and the *10 respiratory phase* reconstruction here depend on the assumption of identical respiratory motion throughout the scan. This may cause some inhomogeneity in true respiratory phase reconstructed. The *moving average* and *gradient* methods presented here directly work on all respiratory cycles, breaking them into their inspiration and expiration components without any dependence on potentially variable breathing patterns.

In contrast to prospectively gated exams that discard 50-60% of data (144), continuous acquisition during free-breathing with our technique uses all imaging data without any additional scan time. This 100% respiratory gating efficiency coupled with radial sampling and retrospective motion correction has been recently demonstrated to reduce scan time for performing whole-heart coronary MRA (145). Undersampling below a certain threshold can introduce image-streak artifacts that may interfere with diagnostic quality. Scans for this study purposefully oversampled the imaging volume to ensure an adequate number of projections for reconstruction of each phase, although radial velocity measurements from a reduction in data have been shown to maintain accuracy (108).

The relatively short phase contrast temporal resolutions for both the 2D (time resolution = 2*TR = 16.4 ms) and 4D (5-point time resolution = 5*TR = 38 ms) acquisitions are much faster

than any physiologically induced temporal blood flow changes, such as from cardiac pulsatility. This allows for retrospective sorting of these projections into any relevant respiratory phase. Large and significant changes between active inspiration and active expiration were observed. This indicates that despite reduced vessel size caused by negative pressure compressing veins, resulting increase in velocity eclipses constriction to produce larger flow values as flow is the product of mean velocity and vessel area. This flow increase in inspiration agrees with a previous Doppler US study in the IJVs (136) in which inspiration flow velocity was 27-31% higher than expiration.

Small and insignificant differences are seen from the *moving average* reconstruction method. This may be explained by resulting portions of the respiratory waveform closest to the moving average which are effectively part of active respiration yet are placed in the plateau phases. As noted above, the active portions of respiration are most influential on venous blood flow, meaning for each plateau there is a muddling of these effects when both active portions are mixed into a single phase. Further study on discarding parts of the waveform nearest to the moving average to remove active portions may help tease out more plateau specific changes.

The near-zero and non-significant changes in summed left and right internal carotid artery total flow measurements serve as an internal control for our presented results. Due to the muscular nature of arteries, the blood flow of which is driven entirely by cardiac pulsatility, no change was expected between respiration phases. The difference from breathing phases induced in IJV flow, with no changes in arteries, suggest alternate outflow pathways for venous drainage during expiration. Further studies into respiratory effect on smaller draining veins may be warranted.

Over the respiratory cycle, while cross-sectional area changes occur, larger magnitude discrepancies occur with mean velocity, effectively dictating flow changes. In healthy volunteers, cardiac independent changes caused by respiration are present in both venous anatomy and blood velocity in the neck.

The cut plane velocity vector visualization exhibits respiratory changes in the velocity vector fields. Qualitative changes are evident, with larger magnitude cardiac time-averaged velocity vectors in inspiration versus expiration. This increase was shown to increase in the superior to inferior direction along the IJV. As the IJV increases in caliber and flow load (receiving additional drainage from the facial vein) and as it nears the SVC and right side of the heart, pressure variations play a larger role in determining flow, encompassed in changes of cross-sectional area and velocity.

There are some limitations to this study. First, Venc optimizations were not performed prior to each 2D scan. While no phase-aliasing was observed in any resulting images, the high Venc used (70 cm/s) caused some images to have low velocity to noise ratio (VNR). Effects of respiration were still observed despite not having optimal VNR. Second, as mentioned above, the *10 respiratory phase* reconstruction assumed the same respiratory period throughout the entire scan. End-expiration length (approximately phases 4-7) varies the greatest from one cycle to the next. These phases would therefore have the greatest error in terms of anatomical and velocity differences induced by respiration. Despite this limitation, peak velocity and minimum area were observed at or near their expected phase locations.

Further optimization of respiratory waveform segmentation is necessary in order to target a specific venous disease state, such as: IJV flow in the context of CCSVI (94), hepatic venous

flow dependence on respiration in Fontan patients (146), or to compare with mechanical models of pulsus paradoxus (147).

In conclusion, the double-gating free-breathing acquisition and reconstruction technique presented here demonstrates the flexibility radial acquisitions offer for retrospective sorting of data. This pilot study exhibits viability of novel 2D and 3D reconstruction algorithms that allow for simultaneous retrospective cardiorespiratory gating. A *gradient* operation on the respiratory waveform exhibited large statistical differences in IJV flow during active respiration, specifically when measured proximal to the heart. Although often ignored in MR imaging but targeted or controlled in Doppler US, these differences could help identify healthy from diseased venous return.

Chapter 6:   Fast 4D flow MRI intracranial segmentation and quantification in tortuous arteries

This chapter presents the development, phantom and in-vivo validation, and in-vivo testing of a 4D flow MRI processing technique that removes user-variability and decreases processing time for large datasets. The material in this chapter was presented at ISMRM 2014 (9) and has been accepted for publication in the Journal of Magnetic Resonance Imaging (10).

6.1 Introduction

6.1.1   Challenges in 4D flow MRI post-processing

4D flow MRI is a 3-directional velocity encoding that is time-resolved to the cardiac cycle, enabling both volumetric angiographic and quantitative assessment of blood flow velocities (49). However, several translational obstacles for the clinical adaptation of 4D flow remain: 3D velocity acquisition through time results in large datasets and consequently long acquisition, reconstruction, and post-processing times.

To mitigate scan time, non-Cartesian trajectories and parallel acquisitions have been developed and implemented (148,149). The 4D flow MRI technique used here, Phase Contrast Vastly-undersampled Isotropic Projection Reconstruction (PC VIPR) (87,88), is an innovative, flow sensitive MRA sequence with a radial acquisition trajectory. Reduced scan time is achieved through k-space edge undersampling. Due to the high image contrast and sparse signal representation after background suppression, PC VIPR demonstrates benign undersampling artifacts that yield high temporal resolution capabilities, important in assessing blood velocity throughout the cardiac cycle. Most prominently, PC VIPR covers a large volume with high isotropic spatial resolution; in the cranial context whole brain vasculature coverage is achieved.

In the post-processing step for 4D flow MRI, accurate flow quantification and flow profile assessment generally requires manual segmentation and careful placements of double-oblique cutplanes orthogonal to the direction of the vessel path to localize measurements. Analysis time and reproducibility become concerns, especially when several measurement locations within the volume are assessed across a large patient population. In vessels with a tortuous path, such as in the siphon of the internal carotid artery (ICA_{siphon}), segmentations and measurements become increasingly user-dependent and time-consuming. Therefore, automated segmentation methods are preferred for robust and consistent measurements, but in the context of 4D flow MRI, have only been presented in large and relatively straight intrathoracic arteries (150,151).

This work aims to develop and implement a fast and internally consistent intracranial whole-vessel semi-automated segmentation and flow quantification centerline processing scheme (CPS) for 4D flow MRI.

6.2 Materials and Methods

6.2.1 Centerline Processing Scheme

Processing Chain

See Figure 6-1. After data loading, foreground vessels are separated from background noise using a time-maximum intensity projection (tMIP) image, which was formed by projecting the maximum complex difference signal of each voxel through all cardiac timeframes. Thus it is based on both phase and magnitude information. The complex difference approach provides high signal and good noise performance, allowing for background suppression and visualization of distal vessels (152).

Background signal is not completely nulled in the complex difference image, exhibiting a normal-like distribution. To threshold the tMIP and remove background signal during segmentation, a minimum variance unbiased estimator was used to fit a normal distribution to all voxels within the FOV, producing mean and standard deviation of the fit (μ, σ). After convergence, the tMIP threshold was automatically set as $\mu + 4\sigma$. This process ensures that background noise will not be present in the whole volume vessel segmentation, making this step completely automatic and user-independent.

Skeletonization on the binary volume was performed according to a thinning procedure suitable for elongated objects such as blood vessels, resulting in a one-voxel wide vessel centerline representation (153). Branch endpoints and junction points were automatically identified and labeled within the vascular tree, producing a unique branch identification for each vessel. Vessels can be segmented based on these vessel identifiers (see below).
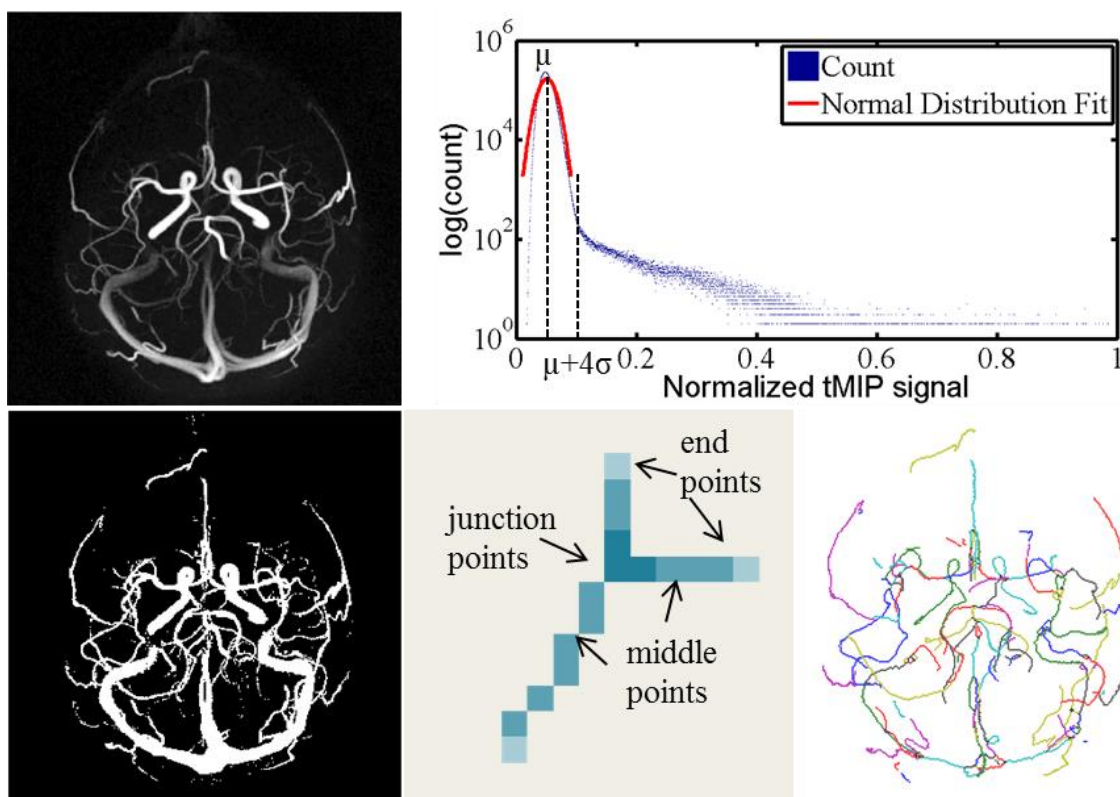
Figure 6-1. Example images and post-processing steps for the centerline processing scheme (CPS). Upper left: Axial time maximum intensity projection (tMIP) of the intracranial vessels. Upper right: Histogram of normalized tMIP signal. After fitting of a normal distribution to the low level background, the threshold is automatically chosen as the mean plus 4 times the standard deviation of the fit (μ+4σ). Anything above this is considered part of the vasculature. Lower left: Binary result. Lower middle: After skeletonization, centerline points are looped over to find junctions, endpoints, and middle points. Lower right: The skeletonized vasculature with each color identifying a separate vessel branch or segment.

At each centerline voxel along the length of the vessel, two points before and after the currently analyzed centerline location were used to calculate and extract orthogonal cutplanes with respect to the propagation of the vessel. Within each cutplane, 2X linear interpolation was performed. Regions of interest (ROIs) were automatically contoured based on k-means clustering (Figure 6-2). Input features for clustering were tMIP and the sum-square of the temporal mean velocity within the extracted cutplane. These features were chosen under the assumption that any cross section will contain two regions: 1. low-signal background and 2. vessels. The clustering

algorithm minimizes the sum of point-to-centroid distances to determine clusters; this approach

has previously been utilized in whole volume automatic particle trace seeding for cardiac 4D

flow MRI data visualization (154). Anatomical and blood flow parameters were then quantified

from the ROI and acquired time-resolved velocity data.
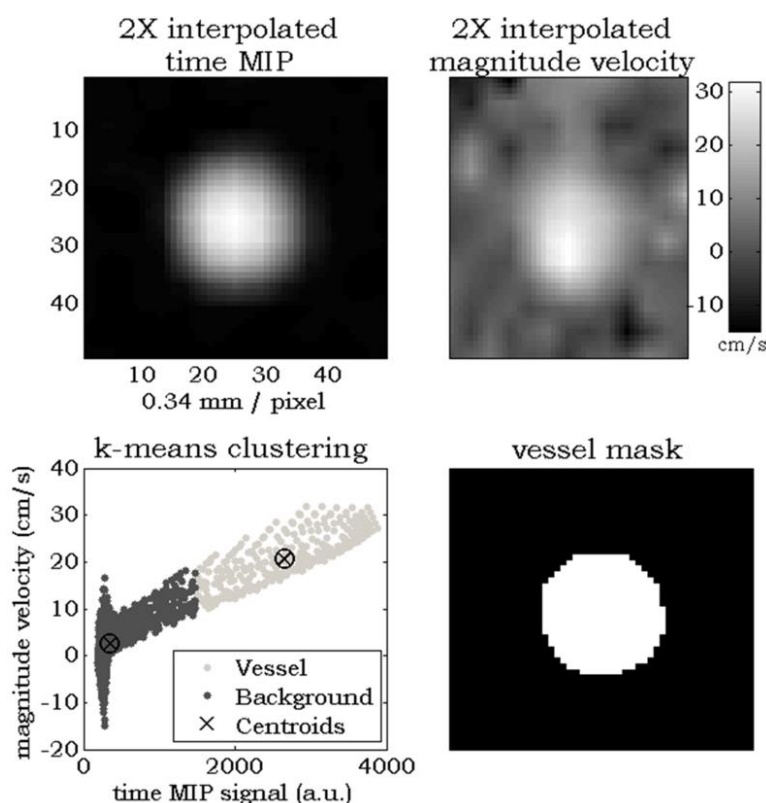
Figure 6-2. Example cutplane k-means analysis in a healthy ICA. In each cutplane along the
length of a centerline, 2X interpolated time MIP signal and sum-squared mean velocity (top row)
are used as input features for the k-means clustering algorithm (bottom left). After the two
clusters are separated, region growing from the center pixel ensures exclusion of extra vessels
within the cutplane to produce a measurement region of interest (bottom right).

Graphical User Interface

For ease of use with the CPS, a graphical user interface (GUI) was developed using

commercial software (*Matlab*, The Mathworks, MA, USA) and is shown in Figure 6-3. System

hardware used for processing was a desktop computer, running *Windows 7* 64-bit (4 core *Intel* i7-4770 3.40 GHz processors, 32 GB RAM). Simple push buttons control data-loading, cropping, segmentation and calculation of parameters. Interactive localization via axial, coronal, and sagittal magnitude images from 4D flow MRI allowed for one-click selection of the vessel of interest, which was automatically segmented using its unique centerline identifier. Points along the segmented vessel display cutplane measurement number, which can be further interrogated with plots and can be individually saved.
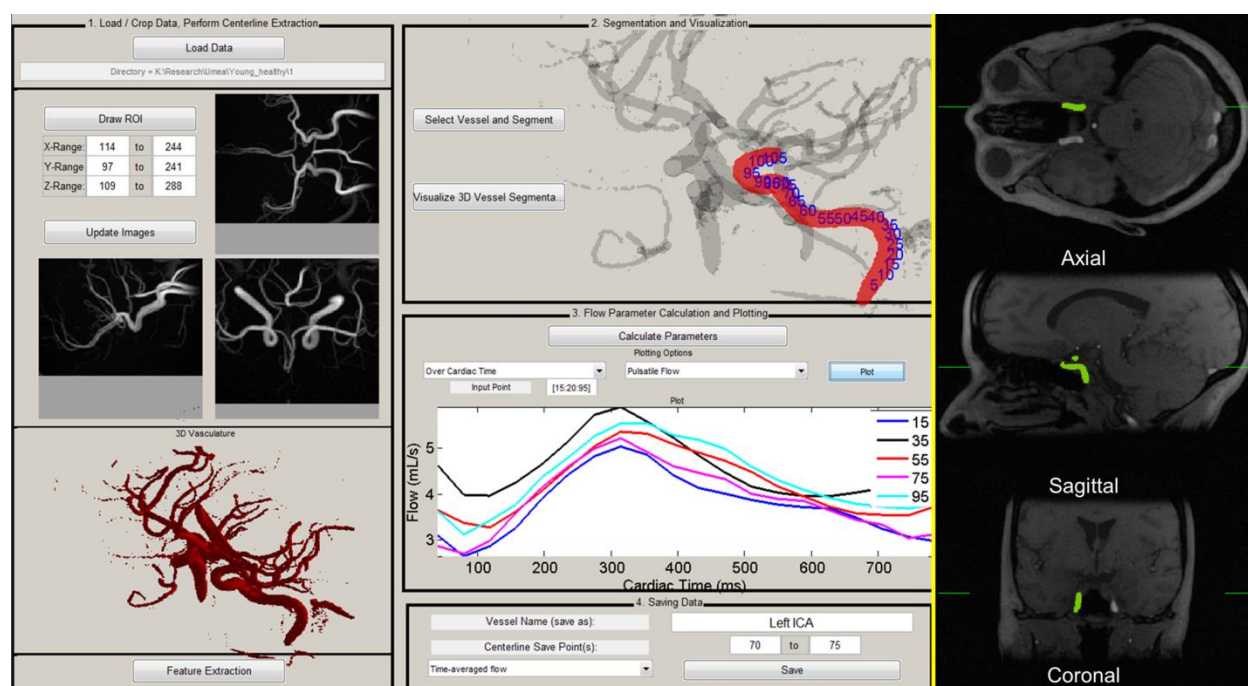
Figure 6-3. 4D flow centerline processing scheme (CPS) graphical user interface. After data loading (1), cropping, automatic thresholding, and visualization of 3D vasculature, vessel centerlines are extracted. The user selects the vessel for segmentation via time-averaged magnitude images with time maximum intensity projection overlaid (right). The segmented 3D vessel with centerline point labels (2) is then visualized, and dynamic parameters can be calculated and plotted for all cardiac phases, shown for pulsatile flow here over 5 locations (3). Parameters can then be saved for specific centerline points (4).

6.2.2   Phantom validation

For validation of the CPS, scans were performed using a clinical 3T system (Discovery MR750, *GE Healthcare*, Waukesha, WI, USA) on an intracranial flow phantom (Model H+N-R-A-010, *Shelley Medical Imaging Technologies*, London, ON, Canada) containing water doped with a single dose of gadolinium contrast equivalent to the amount used for a 70 kg (at 0.2 mmol/kg) subject; this was used to mimic clinical contrast. Six levels of constant flow input values (0.85, 0.95, 1.05, 1.15, 1.25, and 1.35 L/min) were assigned according to normal in-vivo ranges of total intra- plus extra-cerebral blood flow (155). Constant flow was chosen to compare area and flow measurements.

PC VIPR scans were performed with the following parameters: FOV = 22 x 22 x 22 cm^3, acquired spatial resolution - 0.69 mm isotropic, velocity encoding (optimized to maximum signal for highest flow in the middle cerebral artery, MCA) = 70 cm/s, $\alpha = 15^0$, TR/TE = 11.4/3.9 ms, number of projections = 1500. Phase offsets from eddy currents were automatically corrected during reconstruction. For each scan, flow was calculated as cross sectional vessel area multiplied by mean blood velocity. 2D PC scans based on clinical protocols were used for comparison. These were performed in the basilar artery, left and right internal carotid artery, and right MCA of the flow phantom: FOV - 8.0 x 8.0 cm, 0.31 x 0.31 mm in-plane resolution, 3 mm slice thickness, velocity encoding = 50 cm/s for BA/ICA; 70 cm/s for MCA, $\alpha = 15^0$, TR/TE = 7.5/4.6 ms, 2 averages. No eddy current compensation was performed for 2D scans because static parts of the phantom displayed negligible velocity bias (< 1 cm/s). Time for processing each case (4D CPS and manual) was recorded.

6.2.3 In-vivo validation

For the assessment of the CPS in a clinical intracranial territory with pulsatility, ten healthy (7M, age 37 ± 9 years) subjects were imaged after informed consent and IRB approval. PC VIPR scans were performed on a 3T magnet of identical build. Scan parameters: 32 channel head coil, FOV = 22 x 22 x 22 cm^3, (0.69 mm)^3 isotropic resolution, scan time = 9.5 min, Venc = 110 cm/s, 20 reconstructed cardiac timeframes. Data were reconstructed from an acquisition matrix of (300)^3 to (320)^3 using zero padded interpolation during reconstruction. For comparison a single 2D PC scan was performed, covering the left and right ICA at the level of the carotid C3-C4 segment. Scan parameters: 0.35 x 0.35 mm in-plane resolution, 3 mm slice thickness, velocity encoding = 80 cm/s, $\alpha = 15^0$, TR/TE = 7.5/4.6 ms, 6 views per segment, 32 reconstructed cardiac timeframes. This data has been used in a previous study to compare pulsatile flow in PC VIPR versus 2D PC (156). Here we aim not to re-validate pulsatility measures between 2D PC and 4D flow MR, but to demonstrate the use of the CPS to provide accurate semi-automated results in pulsatile flow. CPS waveforms were interpolated to 32 timeframes, allowing one-to-one comparisons of flow throughout the cardiac cycle. For evaluation, waveforms from both 2D PC and the CPS were temporally aligned via cross correlation and averaged across all volunteers. An additional measure of pulsatility index (PI), calculated as:

$$PI = \frac{|Flow_{max} - Flow_{min}|}{Flow_{mean}} \qquad \text{6-1}$$

was used to further compare waveforms.

6.2.4 Demonstration along vessel

To demonstrate the use of the CPS along the length of an entire vessel, whole ICA$_{siphon}$ measurements of area and flow using the CPS were generated from the above in-vivo data.

6.2.5   Statistical Analysis

All processing of data was completed by a researcher (E.S.) with 4+ years of experience in MR flow image processing. In the validation analyses, 4 consecutive centerline points were averaged to closely match slice thickness in 2D PC scans (giving a roughly equivalent slice thickness of 4 x .69 mm = 2.75 mm). Both phantom and in-vivo validation results were compared using least squares regression and Bland-Altman analysis (157). In the whole vessel demonstration, left and right ICA_{siphon} area and flow were partitioned and averaged based on segment (C1 – C7) according to Bouthillier et al (158). Statistical comparisons between each ICA_{siphon} segment were tested using one-way ANOVA (159).

6.3   Results

6.3.1   Phantom validation

Linear regression and Bland-Altman analysis between 2D PC and the 4D CPS is shown in Figure 6-4A. Results comparing both area and flow calculated from the 2D PC scan, and both manual and the CPS 4D flow output are shown in Table 6-1 – top. Very high correlation from regression analysis was seen between different methods, and Bland-Altman results showed roughly 20% limits of agreement. Compared with the 2D PC output, the 4D flow MRI CPS outperformed the 4D manual processing (R = 0.94 vs. R = 0.88). Both forms of 4D processing overestimated the vessel area, yet were still highly correlated (4D manual bias = 2.61 mm^2; R = 0.93, CPS bias = 4.77 mm^2; R = 0.95). Average processing time per vessel across all flow settings using the CPS, including data loading, thinning and centerline extraction, vessel selection and segmentation, and quantification was 56.0 ± 3.6 s. This was less than the time required achieving a single measurement per vessel by processing the data manually (261.4 ± 23.1 s).

6.3.2   In-vivo validation

Similar flow waveforms are observed when comparing between 2D PC and the 4D CPS in both the right and left ICA in-vivo (Figure 6-4B), with overall lower values from the 4D flow scans. Results comparing these flow waveforms, both throughout the waveforms and with PI are shown in Table 6-1 – bottom. A moderate agreement (R = 0.48) for PI was observed, and similar to the phantom results, a strong linear correlation (R = 0.93) was observed for the waveform comparison. The CPS slightly overestimated PI (bias = 0.097), while flow was underestimated (bias = 0.26 or ~ 7% lower than 2D PC).
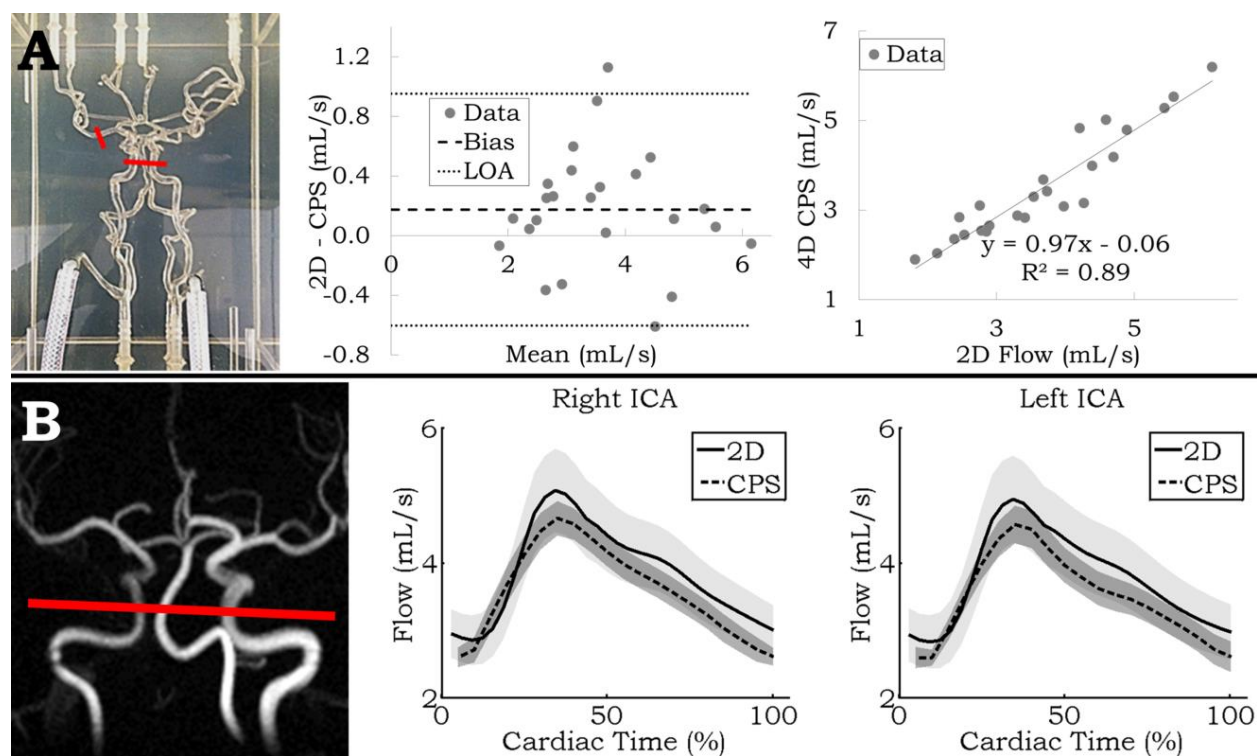
Figure 6-4 A: left – Front view photo of the neurovascular phantom; red segments delineate measurement locations. middle/right – Linear regression and Bland-Altman analysis between the measurements from the 4D centerline processing scheme (CPS) and 2D PC MR. B: left – Limited MIP of PC VIPR in-vivo with 2D PC and CPS measurement location in red. middle/right – 2D PC and CPS flow waveforms averaged across all volunteers for the right and left ICA for 32 timeframes. Shading represents the standard deviation of the mean at each timeframe.

Phantom Validation							
Flow comparison				Area comparison			
	2D vs. CPS	2D vs. 4D manual	CPS vs. 4D manual		2D vs. CPS	2D vs. 4D manual	CPS vs. 4D manual
Slope	0.97	0.94	0.89	Slope	1.42	1.54	0.98
R	0.94	0.88	0.85	R	0.95	0.93	0.86
Bias (mL/s) [upper LOA, lower LOA]	0.18 [0.95, -.60]	0.56 [1.74, -0.61]	-0.39 [0.91, -1.69]	Bias (mm^2) [upper LOA, lower LOA]	-4.77 [2.42, -11.96]	-2.61 [6.72,11.93]	2.16 [7.91, -3.59]

In-vivo Validation			
Pulsatility Index comparison		Flow waveform comparison	
Slope	0.85	Slope	0.93
R	0.48	R	0.93
Bias [upper LOA, lower LOA]	-0.97 [0.26, -0.46]	Bias (mL/s) [upper LOA, lower LOA]	0.26 [0.80, -0.27]

Table 6-1. Top: Linear regression and Bland-Altman analysis results for 2D PC versus 4D (manual and the centerline processing scheme - CPS) comparison of flow (left) and area (right) from N = 24 measurements. Bottom: Linear regression and Bland-Altman analysis performed on in-vivo pulsatile data across ten healthy volunteers for pulsatility index in right and left ICA (N = 20, left) and flow waveform comparison in right and left ICA (frame by frame, N = 64, right). LOA - limit of agreement.

6.3.3 Demonstration along vessel

Figure 6-5 – middle displays boxplot results for left and right summed and segmented ICA$_{siphon}$ averaged area across all volunteers. Figure 6-5 – right shows the same analysis performed on flow. In the C7 segment, area was significantly lower than in the C4-C5 segments, while area in the C6 segment was significantly lower than the C5 segment ($p = 0.0017$). Flow conservation along the length of the ICA$_{siphon}$ was accurately represented by the CPS as no statistical differences were observed between segments ($p = 0.84$).
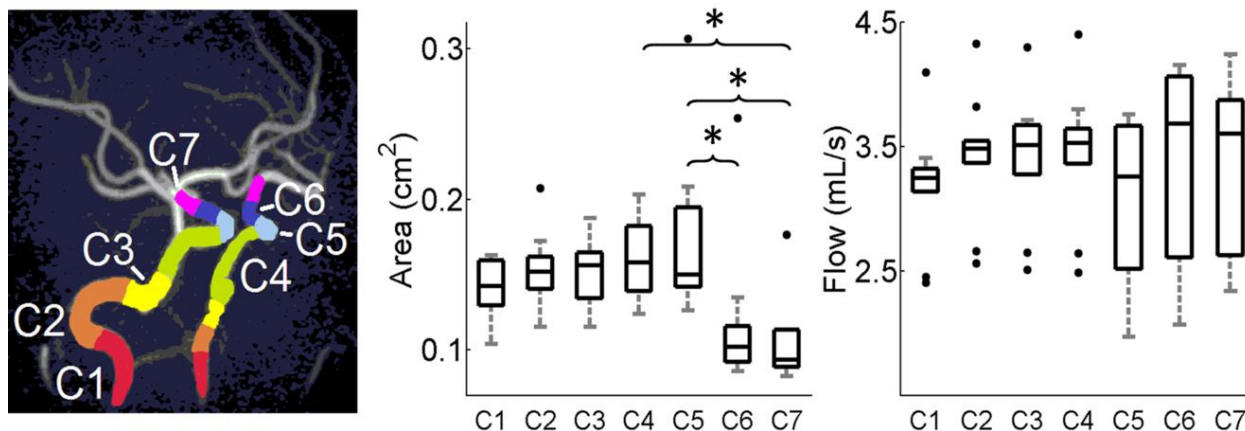
Figure 6-5. Left: Time maximum intensity projection image of arterial vasculature with color overlaid segments. Middle and right: Boxplots of averaged area and flow measurements across all ICA segments shows decreased cross-sectional area in more superior segments while flow is conserved. Upper and lower box boundaries represent the 1st and 3rd quartile of the data, respectively. * - $p < 0.05$

6.4 Discussion

This manuscript presents a reliable and fast post-processing CPS for the assessment of blood flow related parameters derived from 4D flow MRI. Its value lies in the ability to perform user-independent segmentation and quantification in tortuous arterial segments which would be otherwise very difficult to study with other flow sensitive techniques such as transcranial Doppler ultrasound.

Figure 6-3 demonstrates the use of an interactive GUI designed on a commercial software platform and implemented for this study. Vessel segmentation was performed through simple one-click selection on 2D magnitude data. Blood flow over the cardiac cycle can be visualized at specific centerline points in the 3D volume. Because segmentation and flow quantification was automated, results are user-independent and completely repeatable.

Results through both Bland-Altman analysis and linear regression revealed the validity of using the CPS. The CPS allows for faster analysis than can currently be performed for 4D flow

manual post-processing in the brain. Direct comparison of processing times does not elucidate that as the number of locations of interest for interrogation within the neurovasculature increases, time per measurement will decrease. This is because the bulk of processing time is devoted to data loading, which is dependent on the number of reconstructed timeframes (for in-vivo dataset of 20 timeframes and hardware used here, roughly 2 minutes). By comparison, skeletonization and centerline extraction were much quicker (on the order of tens of seconds). After these steps are performed the user was free to select any number of vessels of interest for quantification quickly and efficiently.

Among automated segmentation techniques that have been published elsewhere, the active surface model method by van Pelt (150), while fast, accurate, and topologically stable, is affected by limited spatial resolution and can therefore not segment smaller arteries which are the target of cerebral 4D flow MRI scans. Although pulsatility likely changes luminal diameters in the ICA, such differences in the common carotid artery are on the order of 1 mm in healthy young volunteers (160). Thus active surface modelling would not be needed for these small luminal changes intracranially throughout the cardiac cycle. Additionally, the initial isosurface used in van Pelt (150) was generated with a varying manually-defined threshold on their version of the tMIP. These manual interactions potentially introduce user-dependence and are not part of our automated segmentation scheme.

A centerline approach, in which manual seed points are used for centerline calculation, has been presented before and is currently used for pathological aortic flow assessment (151). While this approach is efficient and integrated into vendor software, it has not been tested in small vascular structures, such as intracranial vessels shown here. Some user interaction of seed point placement for aortic centerline extraction is required, which may introduce user-dependent

variability. The centerline extraction in our method was performed automatically on all vasculature so that the only user interaction is the selection of the vessel branch of interest. Vessel segmentation was performed through simple one-click selection on 2D orthogonal magnitude data. Blood flow over the cardiac cycle can be visualized at specific centerline points in the 3D volume. Because segmentation and flow quantification was automated, results are user-independent and completely repeatable.

Flow estimations were generated at each centerline point along a given arterial branch, which can then be averaged to produce a better estimate of the flow in the branch. As shown with the grouping of different segments of the ICA$_{siphon}$, several consecutive flow measurements can be combined and averaged to give a less noisy representation of blood flow. These combinations of points could be chosen arbitrarily so that particular locations or parameters of interest for the user may be further retrospectively investigated.

Among the ways to measure flow in-vivo, the choice of using 2D PC MR as the gold standard is supported by its high performance in larger vessels such as the ICA (67). There was particularly high correlation between 2D PC and the CPS for area, total flow, and across pulsatile waveforms. While good correlation was still observed between 2D PC and 4D manual output, it was lower than that from the CPS. Potentially confounding and user-dependent factors, including manual placement of orthogonal cutplanes and manual drawing of ROIs, likely contributed to this larger disagreement but are removed in the CPS. Moreover, while the manual processing measures flow through a one-voxel thick cutplane, the CPS results were averaged over consecutive cutplanes to match the slice thickness used in 2D PC measurements. This likely factored into higher correlation seen from the automated results, and illuminates another benefit of this technique.

The higher values and lower correlation in PI from the CPS compared to 2D PC data likely stem from a number well-known factors when comparing 4D flow with 2D PC, including: lower temporal resolution, longer scan times resulting in temporal smoothing of beat to beat variations in waveforms, and lower spatial resolution causing partial volume effects at vessel lumens. Despite these effects, 4D flow and 2D PC have been shown to have the same measurement variability (156), pointing to 4D flow results having equal measurement consistency as 2D PC.

Whole ICA$_{siphon}$ results from the CPS show that, on average, cross-sectional area of the ICA$_{siphon}$ decreases significantly in the distal C7 segment, while blood flow is unchanged. Before bifurcation into the MCA and ACA, the ICA has at most two drainage pathways: the ophthalmic artery in the C5 segment and the posterior communicating artery in the C6 segment (in about 20% of adults). However, due to the small cross-sectional area and observed velocity in these vessels (161), flow was not expected to change significantly along the length of the ICA. This is substantiated by a previous study in the ophthalmic artery of healthy individuals assessing average blood flow to be 0.17 mL/s (162), far below total ICA flow observed in our study. The conservation of mass (i.e. flow) along the length of the ICA$_{siphon}$ shown here is yet another validation of the internal consistency of the presented CPS.

This study has some limitations. First, the CPS relies heavily on good image quality within the tMIP for automated processing in: the global threshold, the vessel segmentation, and the quantification within a cross section using k-means clustering. While this was not an issue in the data for this study, in patients with atypically high or low flow with respect to the Venc, such as flow jets or in slow aneurysm flow, signal dropout in the reconstructed tMIP may cause missed areas of segmentation. This issue would still be present in the 4D manual processing,

however, and can only be ameliorated through some phase unwrapping of the data or a dual-Venc approach in cases where a large flow range is expected (38). Second, this method was introduced and presented only in intracranial arteries for demonstration. It could in theory work in other complicated extracranial vasculature. Examples may include liver and abdominal vessels, or the draining cerebrospinal veins. Further studies are warranted to investigate these territories of interest.

In conclusion, this study exhibits the integration of a number of image processing methods into a fast and internally consistent 4D flow MRI intracranial segmentation and quantification CPS. By viewing vasculature as a tree of unique vessel branches, segmentation of any individual vessel (or concatenated vessels to follow blood along a certain route) provides comprehensive knowledge of flow along the entire vessel. The flexible functionality of the CPS may be of use in other vascular territories or in assessment of blood flow in neurovascular diseases such as stroke or vascular dementia.

Chapter 7:   Summary and Recommendations

7.1 Summary of Research Findings

Within neurovascular diseases, 4D flow MRI provides a platform for complete appraisal of theorized causative parameters. While providing the measurement of volumetric 3-directional velocity fields over time, it also suffers from both long processing times and non-standardized processing methods; its wealth of garnered information must be reliable and consistent for the assessment of many neuropathologies, especially in large patient studies. Furthermore, understanding and quantifying the effect of various physiological processes on blood flow, such as respiratory-induced or day-to-day alterations, enables contextual assessment of post-processed data and may help push 4D flow MRI closer to clinical realization.

Specific contributions of this work include:

- The assessment of 4D flow MRI venous flow healthy population using PC VIPR. Internal consistency in intracranial veins was demonstrated while day-to-day flow in the IJV was shown to be irreproducible.

- A preliminary analysis performed in relation to the CCSVI hypothesis, comparing metrics in NAWM and venous return blood flow. No correlations between altered flow and MS histogram metrics were found.

- The development of a double-gated (both cardiac and respiratory) MRI blood flow acquisition and reconstruction; its assessment in the IJV exhibited respiratory-induced blood flow changes in a group of healthy volunteers.

- The development, validation, and in-vivo implementation of an automated intracranial vessel segmentation and flow parameter measurement software tool (centerline processing scheme, CPS) for fast and consistent 4D flow post-processing analysis.

7.2 Recommendations

As shown in the study concerning the reproducibility of venous blood flow, PC VIPR is internally consistent, even in small intracranial veins. This work may be referenced in future work concerning the use of PC VIPR in other venous territories of interest. Normal day-to-day variations in the internal jugular veins may reach up to 20%. In the CCSVI hypothesis these variations may be construed as diagnostically relevant when in fact they are normal results of subtle changes in head position, hydration level, caffeine level, respiration, etc. Future processing of the CCSVI data must keep these results in mind, either factoring this uncertainty in measured day-to-day changes or by accounting for these many varied effects using some normalization of experimental methods (fasting, scan all patients at the same time of day, etc.). Processing of larger group numbers and statistical correlation analysis is warranted to describe combinations of NAWM metrics to distinguish MS patients from HCs.

For the double-gating acquisition and reconstruction scheme, further optimization of the respiratory waveform partitioning is necessary to target specific venous disease states. In the cardiac realm, a number of potential disease states could be investigated with this technique, such as total cavo-pulmonary connections in Fontan patients. However, image quality may suffer from the added effect of cardiac and respiratory motion. Thus special care must be taken to successfully target respiration plateaus. This may be performed through the use of the *moving average* filter previously described. After filtering, a percentage of projections above and below the moving average (to remove active portions of the respiratory waveform) would provide more accurate representation of the respiration plateaus. Though this would likely result in a longer scan time needed for the appropriate amount of projections in plateaus to be collected. Some optimization of these values must be performed to maintain data consistency and image quality.

Future work regarding the centerline processing scheme (CPS) should focus on expanding its functionality to other anatomies with complicated vasculature. These could include hepatic, abdominal, renal, or draining cerebrospinal veins. In the cardiac vasculature, or in vessels where the lumen diameter and thus the cross-sectional area changes throughout the cardiac cycle, the CPS must be updated to do time-resolved frame-by-frame cutplane segmentations. In typical cardiac measurements from 4D flow MRI, long post-processing times are mitigated by choosing a single segmentation threshold for the entire cardiac cycle (e.g. at end-systole or end-diastole). This type of analysis may lead to errors in flow measurements, as well as flow-derived biomarkers such as turbulent kinetic energy or pressure gradients. An updated CPS would alleviate these concerns while simultaneously providing a faster method for processing these large datasets. Additionally, further improvements should be made to process very large vessels, such as the aorta or vena cava, as the presented version of the CPS is optimized for relatively small intracranial vasculature. Optimization of the skeletonization process needs to be performed for larger vessels. Finally, streamlining of the processing could be improved with better mapping of data input/output. Research into the optimization of the CPS with respect to more powerful processing hardware and PC VIPR datasets will further augment its performance.

References:

1.   Schrauben EM, Johnson KM, Reeder SM, Field A, Wieben O. Reproducibility of Venous Luminography and Flow Quantification Related to the CCSVI Hypothesis. International Society of Magnetic Resonance in Medicine. Melbourne, AUS; 2012. p. 3100.

2.   Schrauben EM, Johnson KM, Huston J, Field A, Wieben O. Cerebrospinal Arterial and Venous Blood Flow Variability assessed with 4D flow MRI. International Society for Magnetic Resonance in Medicine. Salt Lake City, UT, USA; 2013. p. 0622.

3.   Schrauben EM, Johnson KM, Huston J, et al. Reproducibility of cerebrospinal venous blood flow and vessel anatomy with the use of phase contrast-vastly undersampled isotropic projection reconstruction and contrast-enhanced MRA. AJNR Am J Neuroradiol 2014;35(5):999-1006.

4.   Schrauben EM, Johnson KM, Field A, Wieben O. 4D flow MRI assessment of Cerebrospinal Venous blood flow in Multiple Sclerosis Patients and Age/Sex-Matched Controls. International Society for Magnetic Resonance in Medicine. Toronto, CAN; 2015. p. 4565.

5.   Schrauben EM, Johnson KM, Field A, Wieben O. Normal-appearing White Matter and Venous flow Multiparameter comparison Multiple Sclerosis and Healthy Control Subjects. International Society for Magnetic Resonance in Medicine; 2015. p. 4352.

6.   Schrauben EM, Anderson AG, Johnson KM, Field A, Wieben O. Respiratory Effects on Phase Contrast Imaging of the Jugular Vein. SCMR-ISMRM Flow & Motion. Orlando, FL, USA; 2012. p. W4.

7.   Schrauben EMA, A.G., Johnson KM, Wieben O. Double-Gating Shows Respiratory Effects on Venous Phase Contrast Imaging. International Society of Magnetic Resonance in Medicine. Melbourne, AUS; 2012. p. 1005.

8.   Schrauben EM, Anderson AG, Johnson KM, Wieben O. Respiratory-induced venous blood flow effects using flexible retrospective double-gating. J Magn Reson Imaging 2014.

9.   Schrauben E, Wahlin A, Ambarki K, Malm J, Wieben O, Eklund A. Automated 4D Flow Whole Vessel Segmentation and Quantification using Centerline Extraction. International Society for Magnetic Resonance in Medicine. Milan, Italy; 2014.

10.   Schrauben E, Wåhlin A, Ambarki K, et al. Fast 4D flow MRI intracranial segmentation and quantification in tortuous arteries. J Magn Reson Imaging 2015.

11.   Brown WR, Thore CR. Review: cerebral microvascular pathology in ageing and neurodegeneration. Neuropathol Appl Neurobiol 2011;37(1):56-74.

12. Oostendorp M, Post MJ, Backes WH. Vessel growth and function: depiction with contrast-enhanced MR imaging. Radiology 2009;251(2):317-335.

13. Troprès I, Grimault S, Vaeth A, et al. Vessel size imaging. Magn Reson Med 2001;45(3):397-408.

14. Ryu CW, Kwak HS, Jahng GH, Lee HN. High-resolution MRI of intracranial atherosclerotic disease. Neurointervention 2014;9(1):9-20.

15. Tofts PS. Modeling tracer kinetics in dynamic Gd-DTPA MR imaging. J Magn Reson Imaging 1997;7(1):91-101.

16. Moran PR. A flow velocity zeugmatographic interlace for NMR imaging in humans. Magn Reson Imaging 1982;1(4):197-203.

17. Calamante F, Thomas DL, Pell GS, Wiersma J, Turner R. Measuring cerebral blood flow using magnetic resonance imaging techniques. J Cereb Blood Flow Metab 1999;19(7):701-735.

18. Curley PJ, Norrie L, Nicholson A, Galloway JM, Wilkinson AR. Accuracy of carotid duplex is laboratory specific and must be determined by internal audit. Eur J Vasc Endovasc Surg 1998;15(6):511-514.

19. Ansari SA, Schnell S, Carroll T, et al. Intracranial 4D flow MRI: toward individualized assessment of arteriovenous malformation hemodynamics and treatment-induced changes. AJNR Am J Neuroradiol 2013;34(10):1922-1928.

20. Edjlali M, Roca P, Rabrait C, et al. MR selective flow-tracking cartography: a postprocessing procedure applied to four-dimensional flow MR imaging for complete characterization of cranial dural arteriovenous fistulas. Radiology 2014;270(1):261-268.

21. Loecher M, Johnson K, Turski P, Wieben O. Robust Whole-Brain Blood Tracking for 4D flow using Displacement Corrected Probabilistic Streamlines. International Society of Magnetic Resonance in Medicine. Milan, Italy; 2014.

22. Kecskemeti S, Johnson K, Wu Y, Mistretta C, Turski P, Wieben O. High resolution three-dimensional cine phase contrast MRI of small intracranial aneurysms using a stack of stars k-space trajectory. J Magn Reson Imaging 2012;35(3):518-527.

23. Bauer AM, Amin-Hanjani S, Alaraj A, Charbel FT. Quantitative magnetic resonance angiography in the evaluation of the subclavian steal syndrome: report of 5 patients. J Neuroimaging 2009;19(3):250-252.

24. Amin-Hanjani S, Du X, Zhao M, Walsh K, Malisch TW, Charbel FT. Use of quantitative magnetic resonance angiography to stratify stroke risk in symptomatic vertebrobasilar disease. Stroke 2005;36(6):1140-1145.

25. Amin-Hanjani S, Shin JH, Zhao M, Du X, Charbel FT. Evaluation of extracranial-intracranial bypass using quantitative magnetic resonance angiography. J Neurosurg 2007;106(2):291-298.

26. Dolan JM, Kolega J, Meng H. High wall shear stress and spatial gradients in vascular pathology: a review. Ann Biomed Eng 2013;41(7):1411-1427.

27. Zhang C, Xie S, Li S, et al. Flow patterns and wall shear stress distribution in human internal carotid arteries: the geometric effect on the risk for stenoses. Journal of biomechanics 2012;45(1):83-89.

28. Jeong SK, Rosenson RS. Shear rate specific blood viscosity and shear stress of carotid artery in patients with lacunar infarction. BMC neurology 2013;13(1):36.

29. Lauric A, Hippelheuser J, Cohen AD, Kadasi LM, Malek AM. Wall shear stress association with rupture status in volume matched sidewall aneurysms. Journal of neurointerventional surgery 2013.

30. Rivera-Rivera LA, Schrauben EM, Johnson SC, et al. 4D Flow MRI for intracranial hemodynamic assessment in Alzheimer's Disease. International Society of Magnetic Resonance in Medicine. Milan, Italy; 2014.

31. Roher AE, Garami Z, Tyas SL, et al. Transcranial doppler ultrasound blood flow velocity and pulsatility index as systemic indicators for Alzheimer's disease. Alzheimers Dement 2011;7(4):445-455.

32. Wåhlin A, Schrauben E, Wieben O, Ambarki K, Malm J, Eklund A. Distal Cerebral Arterial Pulsatility using 4D flow MRI. International Society of Magnetic Resonance in Medicine. Milan, Italy; 2014.

33. Hashemi RH, Bradley Jr. WG, Lisanti CJ. MRI - The Basics. Philadelphia, PA, USA: Lippincott Williams & Wilkins: 2010.

34. Tubridy N, McKinstry CS. Neuroradiological history: Sir Joseph Larmor and the basis of MRI physics. Neuroradiology 2000;42(11):852-855.

35. Weishaupt D, Kochli VD, Marincek B. How Does MRI Work?An Introduction to the Physics and Function of Magnetic Resonance Imaging Berlin, Germany: Springer-Verlag: 2008.

36. Bernstein MA, King KF, Zhou XJ. Handbook of MRI Pulse Sequences. Burlington, MA, USA: Elsevier Academic Press: 2004.

37. Stanisz GJ, Odrobina EE, Pun J, et al. T1, T2 relaxation and magnetization transfer in tissue at 3T. Magn Reson Med 2005;54(3):507-512.

38. Nett EJ, Johnson KM, Frydrychowicz A, et al. Four-dimensional phase contrast MRI with accelerated dual velocity encoding. J Magn Reson Imaging 2012;35(6):1462-1471.

39.   Knobloch V, Binter C, Gülan U, et al. Mapping mean and fluctuating velocities by Bayesian multipoint MR velocity encoding-validation against 3D particle tracking velocimetry. Magn Reson Med 2014;71(4):1405-1415.

40.   Walker PG, Cranney GB, Scheidegger MB, Waseleski G, Pohost GM, Yoganathan AP. Semiautomated method for noise reduction and background phase error correction in MR phase velocity data. J Magn Reson Imaging 1993;3(3):521-530.

41.   Bernstein MA, Zhou XJ, Polzin JA, et al. Concomitant gradient terms in phase contrast MR: analysis and correction. Magn Reson Med 1998;39(2):300-308.

42.   Peeters JM, Bos C, Bakker CJ. Analysis and correction of gradient nonlinearity and B0 inhomogeneity related scaling errors in two-dimensional phase contrast flow measurements. Magn Reson Med 2005;53(1):126-133.

43.   Markl M, Bammer R, Alley MT, et al. Generalized reconstruction of phase contrast MRI: analysis and correction of the effect of gradient field distortions. Magn Reson Med 2003;50(4):791-801.

44.   King KF, Ganin A, Zhou XJ, Bernstein MA. Concomitant gradient field effects in spiral scans. Magn Reson Med 1999;41(1):103-112.

45.   Lankhaar JW, Hofman MB, Marcus JT, Zwanenburg JJ, Faes TJ, Vonk-Noordegraaf A. Correction of phase offset errors in main pulmonary artery flow quantification. J Magn Reson Imaging 2005;22(1):73-79.

46.   Chernobelsky A, Shubayev O, Comeau CR, Wolff SD. Baseline correction of phase contrast images improves quantification of blood flow in the great vessels. J Cardiovasc Magn Reson 2007;9(4):681-685.

47.   Giese D, Haeberlin M, Barmet C, Pruessmann KP, Schaeffter T, Kozerke S. Analysis and correction of background velocity offsets in phase-contrast flow measurements using magnetic field monitoring. Magn Reson Med 2012;67(5):1294-1302.

48.   Holland BJ, Printz BF, Lai WW. Baseline correction of phase-contrast images in congenital cardiovascular magnetic resonance. J Cardiovasc Magn Reson 2010;12:11.

49.   Markl M, Frydrychowicz A, Kozerke S, Hope M, Wieben O. 4D flow MRI. J Magn Reson Imaging 2012;36(5):1015-1036.

50.   Dumoulin CL, Souza SP, Walker MF, Wagle W. Three-dimensional phase contrast angiography. Magn Reson Med 1989;9(1):139-149.

51.   Lum DP, Johnson KM, Paul RK, et al. Transstenotic pressure gradients: measurement in swine--retrospectively ECG-gated 3D phase-contrast MR angiography versus endovascular pressure-sensing guidewires. Radiology 2007;245(3):751-760.

52.   Rengier F, Delles M, Eichhorn J, et al. Noninvasive pressure difference mapping derived from 4D flow MRI in patients with unrepaired and repaired aortic coarctation. Cardiovasc Diagn Ther 2014;4(2):97-103.

53.   Wentland AL, Wieben O, François CJ, et al. Aortic pulse wave velocity measurements with undersampled 4D flow-sensitive MRI: comparison with 2D and algorithm determination. J Magn Reson Imaging 2013;37(4):853-859.

54.   Dyverfeldt P, Ebbers T, Länne T. Pulse wave velocity with 4D flow MRI: systematic differences and age-related regional vascular stiffness. Magn Reson Imaging 2014;32(10):1266-1271.

55.   Carlsson M, Heiberg E, Toger J, Arheden H. Quantification of left and right ventricular kinetic energy using four-dimensional intracardiac magnetic resonance imaging flow measurements. Am J Physiol Heart Circ Physiol 2012;302(4):H893-900.

56.   Zajac J, Eriksson J, Dyverfeldt P, Bolger AF, Ebbers T, Carlhäll CJ. Turbulent kinetic energy in normal and myopathic left ventricles. J Magn Reson Imaging 2014.

57.   Dyverfeldt P, Hope MD, Tseng EE, Saloner D. Magnetic resonance measurement of turbulent kinetic energy for the estimation of irreversible pressure loss in aortic stenosis. JACC Cardiovasc Imaging 2013;6(1):64-71.

58.   Bieging ET, Frydrychowicz A, Wentland A, et al. In vivo three-dimensional MR wall shear stress estimation in ascending aortic dilatation. J Magn Reson Imaging 2011;33(3):589-597.

59.   Barker AJ, Roldán-Alzate A, Entezari P, et al. Four-dimensional flow assessment of pulmonary artery flow and wall shear stress in adult pulmonary arterial hypertension: Results from two institutions. Magn Reson Med 2014.

60.   van Ooij P, Potters WV, Collins J, et al. Characterization of Abnormal Wall Shear Stress Using 4D Flow MRI in Human Bicuspid Aortopathy. Ann Biomed Eng 2014.

61.   Frydrychowicz A, Winterer JT, Zaitsev M, et al. Visualization of iliac and proximal femoral artery hemodynamics using time-resolved 3D phase contrast MRI at 3T. J Magn Reson Imaging 2007;25(5):1085-1092.

62.   Roldán-Alzate A, Frydrychowicz A, Niespodzany E, et al. In vivo validation of 4D flow MRI for assessing the hemodynamics of portal hypertension. J Magn Reson Imaging 2013;37(5):1100-1108.

63.   Frydrychowicz A, Landgraf BR, Niespodzany E, et al. Four-dimensional velocity mapping of the hepatic and splanchnic vasculature with radial sampling at 3 tesla: a feasibility study in portal hypertension. J Magn Reson Imaging 2011;34(3):577-584.

64. Markl M, Kilner PJ, Ebbers T. Comprehensive 4D velocity mapping of the heart and great vessels by cardiovascular magnetic resonance. J Cardiovasc Magn Reson 2011;13:7.

65. Markl M, Geiger J, Arnold R, et al. Comprehensive 4-dimensional magnetic resonance flow analysis after successful heart transplantation resolves controversial intraoperative findings and reveals complex hemodynamic alterations. Circulation 2011;123(11):e381-383.

66. Kadbi M, Negahdar M, Traughber M, Martin P, Amini AA. Assessment of flow and hemodynamics in the carotid artery using a reduced TE 4D flow spiral phase-contrast MRI. Conf Proc IEEE Eng Med Biol Soc 2013;2013:1100-1103.

67. Wåhlin A, Ambarki K, Hauksson J, Birgander R, Malm J, Eklund A. Phase contrast MRI quantification of pulsatile volumes of brain arteries, veins, and cerebrospinal fluids compartments: repeatability and physiological interactions. J Magn Reson Imaging 2012;35(5):1055-1062.

68. Ambarki K, Hallberg P, Jóhannesson G, et al. Blood flow of ophthalmic artery in healthy individuals determined by phase-contrast magnetic resonance imaging. Invest Ophthalmol Vis Sci 2013;54(4):2738-2745.

69. Wahlin A, Ambarki K, Birgander R, et al. Measuring pulsatile flow in cerebral arteries using 4D phase-contrast MR imaging. AJNR American journal of neuroradiology 2013;34(9):1740-1745.

70. Nayak KS, Tsai CM, Meyer CH, Nishimura DG. Efficient off-resonance correction for spiral imaging. Magn Reson Med 2001;45(3):521-524.

71. Ahn CB, Kim JH, Cho ZH. High-speed spiral-scan echo planar NMR imaging-I. IEEE Trans Med Imaging 1986;5(1):2-7.

72. Yang Y, Glover GH, van Gelderen P, et al. Fast 3D functional magnetic resonance imaging at 1.5 T with spiral acquisition. Magn Reson Med 1996;36(4):620-626.

73. Schäffter T, Rasche V, Carlsen IC. Motion compensated projection reconstruction. Magn Reson Med 1999;41(5):954-963.

74. Glover GH, Pauly JM. Projection reconstruction techniques for reduction of motion effects in MRI. Magn Reson Med 1992;28(2):275-289.

75. Pipe JG. Motion correction with PROPELLER MRI: application to head motion and free-breathing cardiac imaging. Magn Reson Med 1999;42(5):963-969.

76. Hope MD, Meadows AK, Hope TA, et al. Images in cardiovascular medicine. Evaluation of bicuspid aortic valve and aortic coarctation with 4D flow magnetic resonance imaging. Circulation 2008;117(21):2818-2819.

77. Pruessmann KP, Weiger M, Scheidegger MB, Boesiger P. SENSE: sensitivity encoding for fast MRI. Magn Reson Med 1999;42(5):952-962.

78. Sodickson DK, Manning WJ. Simultaneous acquisition of spatial harmonics (SMASH): fast imaging with radiofrequency coil arrays. Magn Reson Med 1997;38(4):591-603.

79. Schnell S, Markl M, Entezari P, et al. k-t GRAPPA accelerated four-dimensional flow MRI in the aorta: effect on scan time, image quality, and quantification of flow and wall shear stress. Magn Reson Med 2014;72(2):522-533.

80. Stankovic Z, Fink J, Collins JD, et al. K-t GRAPPA-accelerated 4D flow MRI of liver hemodynamics: influence of different acceleration factors on qualitative and quantitative assessment of blood flow. MAGMA 2014.

81. Lustig M, Donoho D, Pauly JM. Sparse MRI: The application of compressed sensing for rapid MR imaging. Magn Reson Med 2007;58(6):1182-1195.

82. Knobloch V, Boesiger P, Kozerke S. Sparsity transform k-t principal component analysis for accelerating cine three-dimensional flow measurements. Magn Reson Med 2013;70(1):53-63.

83. Hsiao A, Lustig M, Alley MT, Murphy MJ, Vasanawala SS. Evaluation of valvular insufficiency and shunts with parallel-imaging compressed-sensing 4D phase-contrast MR imaging with stereoscopic 3D velocity-fusion volume-rendered visualization. Radiology 2012;265(1):87-95.

84. Hsiao A, Lustig M, Alley MT, et al. Rapid pediatric cardiac assessment of flow and ventricular volume with compressed sensing parallel imaging volumetric cine phase-contrast MRI. AJR Am J Roentgenol 2012;198(3):W250-259.

85. Tariq U, Hsiao A, Alley M, Zhang T, Lustig M, Vasanawala SS. Venous and arterial flow quantification are equally accurate and precise with parallel imaging compressed sensing 4D phase contrast MRI. J Magn Reson Imaging 2013;37(6):1419-1426.

86. Lauterbur PC. Magnetic resonance zeugmatography. Pure and Applied Chemistry 1974;40(1-2):149-157.

87. Johnson KM, Lum DP, Turski PA, Block WF, Mistretta CA, Wieben O. Improved 3D phase contrast MRI with off-resonance corrected dual echo VIPR. Magn Reson Med 2008;60(6):1329-1336.

88. Gu T, Korosec FR, Block WF, et al. PC VIPR: a high-speed 3D phase-contrast method for flow quantification and high-resolution angiography. AJNR Am J Neuroradiol 2005;26(4):743-749.

89. O'Gara PT. Cardiology patient page. Aortic aneurysm. Circulation 2003;107(6):e43-45.

90. Limbu YR, Gurung G, Malla R, Rajbhandari R, Regmi SR. Assessment of carotid artery dimensions by ultrasound in non-smoker healthy adults of both sexes. Nepal Med Coll J 2006;8(3):200-203.

91. Hofman MB, Visser FC, van Rossum AC, Vink QM, Sprenger M, Westerhof N. In vivo validation of magnetic resonance blood volume flow measurements with limited spatial resolution in small vessels. Magn Reson Med 1995;33(6):778-784.

92. Turk AS, Johnson KM, Lum D, et al. Physiologic and anatomic assessment of a canine carotid artery stenosis model utilizing phase contrast with vastly undersampled isotropic projection imaging. AJNR Am J Neuroradiol 2007;28(1):111-115.

93. Zamboni P, Galeotti R, Menegatti E, et al. Chronic cerebrospinal venous insufficiency in patients with multiple sclerosis. Journal of neurology, neurosurgery, and psychiatry 2009;80(4):392-399.

94. Zamboni P, Galeotti R. The chronic cerebrospinal venous insufficiency syndrome. Phlebology 2010;25(6):269-279.

95. Doepp F, Paul F, Valdueza JM, Schmierer K, Schreiber SJ. No cerebrocervical venous congestion in patients with multiple sclerosis. Annals of neurology 2010;68(2):173-183.

96. Baracchini C, Perini P, Causin F, Calabrese M, Rinaldi F, Gallo P. Progressive multiple sclerosis is not associated with chronic cerebrospinal venous insufficiency. Neurology 2011;77(9):844-850.

97. Yamout B, Herlopian A, Issa Z, et al. Extracranial venous stenosis is an unlikely cause of multiple sclerosis. Mult Scler 2010;16(11):1341-1348.

98. Centonze D, Floris R, Stefanini M, et al. Proposed chronic cerebrospinal venous insufficiency criteria do not predict multiple sclerosis risk or severity. Annals of neurology 2011;70(1):51-58.

99. Fox RJ, Rae-Grant A. Chronic cerebrospinal venous insufficiency: have we found the cause and cure of MS? Neurology 2011;77(2):98-100.

100. Utriainen D, Feng W, Elias S, Latif Z, Hubbard D, Haacke EM. Using magnetic resonance imaging as a means to study chronic cerebral spinal venous insufficiency in multiple sclerosis patients. Techniques in vascular and interventional radiology 2012;15(2):101-112.

101. Utriainen D, Trifan G, Sethi S, et al. Magnetic resonance imaging signatures of vascular pathology in multiple sclerosis. Neurological research 2012;34(8):780-792.

102. Menegatti E, Genova V, Tessari M, et al. The reproducibility of colour Doppler in chronic cerebrospinal venous insufficiency associated with multiple sclerosis. International angiology : a journal of the International Union of Angiology 2010;29(2):121-126.

103. Klabunde RE. Cardiovascular physiology concepts. Philadelphia, PA: Lippincott Williams & Wilkins/Wolters Kluwer: 2012. xi, 243 p. p.

104. Khatri VP, Wagner-Sevy S, Espinosa MH, Fisher JB. The internal jugular vein maintains its regional anatomy and patency after carotid endarterectomy: a prospective study. Annals of surgery 2001;233(2):282-286.

105. Lu M, Raber L, L. B. Ultrasound evaluations of chronic cerebrospinal venous insufficiency (CCSVI): Important factors to consider. AAN Annual Meeting Honolulu, HI, USA; 2011.

106. Nordenstrom B, Norhagen A. Effect of respiration on venous return to the heart. The American journal of roentgenology, radium therapy, and nuclear medicine 1965;95(3):655-661.

107. Stalder AF, Russe MF, Frydrychowicz A, Bock J, Hennig J, Markl M. Quantitative 2D and 3D phase contrast MRI: optimized analysis of blood flow and vessel wall parameters. Magn Reson Med 2008;60(5):1218-1231.

108. Wentland AL, Wieben O, Korosec FR, Haughton VM. Accuracy and reproducibility of phase-contrast MR imaging measurements for CSF flow. AJNR American journal of neuroradiology 2010;31(7):1331-1336.

109. Frydrychowicz A, Wieben O, Niespodzany E, Reeder SB, Johnson KM, François CJ. Quantification of thoracic blood flow using volumetric magnetic resonance imaging with radial velocity encoding: in vivo validation. Invest Radiol 2013;48(12):819-825.

110. Wentland AL, Grist TM, Wieben O. Repeatability and internal consistency of abdominal 2D and 4D phase contrast MR flow measurements. Acad Radiol 2013;20(6):699-704.

111. Bland JM, Altman DG. Agreement between methods of measurement with multiple observations per individual. J Biopharm Stat 2007;17(4):571-582.

112. Zivadinov R, Marr K, Cutter G, et al. Prevalence, sensitivity, and specificity of chronic cerebrospinal venous insufficiency in MS. Neurology 2011;77(2):138-144.

113. Garg N, Garg N. Jugular Venous Pulse: An Appraisal. Indian Academy of Clinical Medicine 2000(1):260-269.

114. Lin S-KC, Y-J.; Yang, F-Y.;. Hemodynamics of the Internal Jugular Vein: An Ultrasonographic Study. Tzu Chi Medical Journal 2009;21(4):317-322.

115. Chung CP, Hsu HY, Chao AC, Wong WJ, Sheng WY, Hu HH. Flow volume in the jugular vein and related hemodynamics in the branches of the jugular vein. Ultrasound in medicine & biology 2007;33(4):500-505.

116. De Diego JI, Prim MP, Garcia-Raya P, Madero R, Gavilan J. Reproducibility of ultrasonographic measures in internal jugular veins of normal subjects. Auris, nasus, larynx 2001;28(1):71-74.

117. McTaggart RA, Fischbein NJ, Elkins CJ, et al. Extracranial venous drainage patterns in patients with multiple sclerosis and healthy controls. AJNR American journal of neuroradiology 2012;33(8):1615-1620.

118. Zaharchuk G, Fischbein NJ, Rosenberg J, Herfkens RJ, Dake MD. Comparison of MR and contrast venography of the cervical venous system in multiple sclerosis. AJNR American journal of neuroradiology 2011;32(8):1482-1489.

119. Al-Omari MH, Rousan LA. Internal jugular vein morphology and hemodynamics in patients with multiple sclerosis. Int Angiol 2010;29(2):115-120.

120. Zivadinov R, Schirda C, Dwyer MG, et al. Chronic cerebrospinal venous insufficiency and iron deposition on susceptibility-weighted imaging in patients with multiple sclerosis: a pilot case-control study. Int Angiol 2010;29(2):158-175.

121. Barreto AD, Brod SA, Bui TT, et al. Chronic cerebrospinal venous insufficiency: case-control neurosonography results. Ann Neurol 2013;73(6):721-728.

122. Sundström P, Wåhlin A, Ambarki K, Birgander R, Eklund A, Malm J. Venous and cerebrospinal fluid flow in multiple sclerosis: a case-control study. Ann Neurol 2010;68(2):255-259.

123. Wattjes MP, van Oosten BW, de Graaf WL, et al. No association of abnormal cranial venous drainage with multiple sclerosis: a magnetic resonance venography and flow-quantification study. J Neurol Neurosurg Psychiatry 2011;82(4):429-435.

124. Macgowan CK, Chan KY, Laughlin S, Marrie RA, Banwell B. Cerebral arterial and venous blood flow in adolescent multiple sclerosis patients and age-matched controls using phase contrast MRI. J Magn Reson Imaging 2014;40(2):341-347.

125. Van den Berg PJ, Van den Berg GB, Westerhuis LW, Visser LH. Occurrence of CCSVI in patients with MS and its relationship with iron metabolism and varicose veins. Eur J Neurol 2013;20(3):519-526.

126. Blinkenberg M, Akeson P, Sillesen H, et al. Chronic cerebrospinal venous insufficiency and venous stenoses in multiple sclerosis. Acta Neurol Scand 2012;126(6):421-427.

127. Traboulsee AL, Knox KB, Machan L, et al. Prevalence of extracranial venous narrowing on catheter venography in people with multiple sclerosis, their siblings, and unrelated healthy controls: a blinded, case-control study. Lancet 2014;383(9912):138-145.

128. Moll NM, Rietsch AM, Thomas S, et al. Multiple sclerosis normal-appearing white matter: pathology-imaging correlations. Ann Neurol 2011;70(5):764-773.

129. Law M, Saindane AM, Ge Y, et al. Microvascular abnormality in relapsing-remitting multiple sclerosis: perfusion MR imaging findings in normal-appearing white matter. Radiology 2004;231(3):645-652.

130. Glickman ME, Rao SR, Schultz MR. False discovery rate control is a recommended alternative to Bonferroni-type adjustments in health studies. J Clin Epidemiol 2014;67(8):850-857.

131. Gatehouse PD, Keegan J, Crowe LA, et al. Applications of phase-contrast flow and velocity imaging in cardiovascular MRI. Eur Radiol 2005;15(10):2172-2184.

132. Nordenström B, Norhagen A. Effect of respiration on venous return to the heart. Am J Roentgenol Radium Ther Nucl Med 1965;95(3):655-661.

133. BRECHER GA, HUBAY CA. Pulmonary blood flow and venous return during spontaneous respiration. Circ Res 1955;3(2):210-214.

134. Ross M, Pawlina W. Histology: A Text and Atlas, with Correlated Cell and Molecular Biology, 5th Edition: Lippincott Williams & Wilkins: 2006. 3 p.

135. Thompson RB, McVeigh ER. Cardiorespiratory-resolved magnetic resonance imaging: measuring respiratory modulation of cardiac function. Magn Reson Med 2006;56(6):1301-1310.

136. Pucheu A, Evans J, Thomas D, Scheuble C, Pucheu M. Doppler ultrasonography of normal neck veins. Journal of clinical ultrasound : JCU 1994;22(6):367-373.

137. Ginghina C, Beladan CC, Iancu M, Calin A, Popescu BA. Respiratory maneuvers in echocardiography: a review of clinical applications. Cardiovasc Ultrasound 2009;7:42.

138. Feng W, Utriainen D, Trifan G, et al. Characteristics of flow through the internal jugular veins at cervical C2/C3 and C5/C6 levels for multiple sclerosis patients using MR phase contrast imaging. Neurol Res 2012;34(8):802-809.

139. Stoquart-Elsankari S, Lehmann P, Villette A, et al. A phase-contrast MRI study of physiologic cerebral venous flow. J Cereb Blood Flow Metab 2009;29(6):1208-1215.

140. Barger AV, Peters DC, Block WF, et al. Phase-contrast with interleaved undersampled projections. Magn Reson Med 2000;43(4):503-509.

141. Peters DC, Korosec FR, Grist TM, et al. Undersampled projection reconstruction applied to MR angiography. Magn Reson Med 2000;43(1):91-101.

142. Barger AV, Block WF, Toropov Y, Grist TM, Mistretta CA. Time-resolved contrast-enhanced imaging with isotropic resolution and broad coverage using an undersampled 3D projection trajectory. Magn Reson Med 2002;48(2):297-305.

143.   Markl M, Hennig J. Phase contrast MRI with improved temporal resolution by view sharing: k-space related velocity mapping properties. Magn Reson Imaging 2001;19(5):669-676.

144.   Sachs TS, Meyer CH, Hu BS, Kohli J, Nishimura DG, Macovski A. Real-time motion detection in spiral MRI using navigators. Magnetic resonance in medicine : official journal of the Society of Magnetic Resonance in Medicine / Society of Magnetic Resonance in Medicine 1994;32(5):639-645.

145.   Pang J, Bhat H, Sharif B, et al. Whole-heart coronary MRA with 100% respiratory gating efficiency: self-navigated three-dimensional retrospective image-based motion correction (TRIM). Magnetic resonance in medicine : official journal of the Society of Magnetic Resonance in Medicine / Society of Magnetic Resonance in Medicine 2014;71(1):67-74.

146.   Hsia TY, Khambadkone S, Redington AN, Migliavacca F, Deanfield JE, de Leval MR. Effects of respiration and gravity on infradiaphragmatic venous flow in normal and Fontan patients. Circulation 2000;102(19 Suppl 3):III148-153.

147.   Xing CY, Cao TS, Yuan LJ, et al. Mechanism study of pulsus paradoxus using mechanical models. PLoS One 2013;8(2):e57512.

148.   Carlsson M, Toger J, Kanski M, et al. Quantification and visualization of cardiovascular 4D velocity mapping accelerated with parallel imaging or k-t BLAST: head to head comparison and validation at 1.5 T and 3 T. Journal of cardiovascular magnetic resonance : official journal of the Society for Cardiovascular Magnetic Resonance 2011;13:55.

149.   Sigfridsson A, Petersson S, Carlhall CJ, Ebbers T. Four-dimensional flow MRI using spiral acquisition. Magnetic resonance in medicine : official journal of the Society of Magnetic Resonance in Medicine / Society of Magnetic Resonance in Medicine 2012;68(4):1065-1073.

150.   van Pelt R, Nguyen H, ter Haar Romeny B, Vilanova A. Automated segmentation of blood-flow regions in large thoracic arteries using 3D-cine PC-MRI measurements. International journal of computer assisted radiology and surgery 2012;7(2):217-224.

151.   Semaan EM, Carr M, Gulsun M, et al. Evaluation of an optimized post-processing tool for 4D flow MRI data analysis in healthy volunteers and patients with aortic stenosis, aortic insufficiency, and aortic aneurysm. 22nd Annual Meeting of International Society for Magnetic Resonance in Medicine. Milan, IT; 2014. p. 3948.

152.   Anderson AG, Johnson KM, Bock J, Markl M, Wieben O. Comparison of Image Reconstructioin Algorithms for the Depiction of Vessel Anatomy in PC VIPR Datasets. 16th Annual Meeting of International Society for Magnetic Resonance in Medicine. Toronto, ON, CA; 2008. p. 934.

153. Palágyi KS E, Balogh E, Kuba A, Halmai C, Erdôhelyi B, Hausegger K. A sequential 3D thinning algorithm and its medical applications. Porc 17th Int Conf Information Processing in Medical Imaging. Davis, CA, USA; 2001.

154. Stalder AF, Gulsun MA, Greiser A, Jolly M-P. Fully automatic visualization of 4D Flow data. Internal Society of Magnetic Resonance in Medicine. Salt Lake City, UT, USA; 2013.

155. Uematsu S, Yang A, Preziosi TJ, Kouba R, Toung TJ. Measurement of carotid blood flow in man and its clinical application. Stroke; a journal of cerebral circulation 1983;14(2):256-266.

156. Wåhlin A, Ambarki K, Birgander R, et al. Measuring pulsatile flow in cerebral arteries using 4D phase-contrast MR imaging. AJNR Am J Neuroradiol 2013;34(9):1740-1745.

157. Bland JM, Altman DG. Agreement between methods of measurement with multiple observations per individual. J Biopharm Stat 2007;17(4):571-582.

158. Bouthillier A, van Loveren HR, Keller JT. Segments of the internal carotid artery: a new classification. Neurosurgery 1996;38(3):425-432; discussion 432-423.

159. Rosner B. Fundamentals of Biostatistics. 7 ed. Boston, MA: Brooks/Cole; 2010. p. 562-567.

160. Studinger P, Lénárd Z, Kováts Z, Kocsis L, Kollai M. Static and dynamic changes in carotid artery diameter in humans during and after strenuous exercise. J Physiol 2003;550(Pt 2):575-583.

161. Klotzsch C, Popescu O, Berlit P. Assessment of the posterior communicating artery by transcranial color-coded duplex sonography. Stroke; a journal of cerebral circulation 1996;27(3):486-489.

162. Ambarki K, Hallberg P, Johannesson G, et al. Blood flow of ophthalmic artery in healthy individuals determined by phase-contrast magnetic resonance imaging. Investigative ophthalmology & visual science 2013;54(4):2738-2745.